

MÁSTER UNIVERSITARIO EN INGENIERÍA INDUSTRIAL

TRABAJO FIN DE MÁSTER

SIMULATIVE INVESTIGATION ON THE CONTACT PATTERN OF POLYMER CROSSED HELICAL GEARS BY FEM

Autor: Ángel Moro García

Director: José Rubén Pérez Domínguez

Madrid

Declaro, bajo mi responsabilidad, que el Proyecto presentado con el título

Simulative investigation on the contact pattern of polymer crossed helical gears by FEM

en la ETS de Ingeniería - ICAI de la Universidad Pontificia Comillas en el

curso académico 2022/23 es de mi autoría, original e inédito y

no ha sido presentado con anterioridad a otros efectos.

El Proyecto no es plagio de otro, ni total ni parcialmente y la información que ha sido

tomada de otros documentos está debidamente referenciada.

Fdo.: Ángel Moro García Fecha: 07/ 07/ 2023



Autorizada la entrega del proyecto

EL DIRECTOR DEL PROYECTO



Firmado digitalmente por Jose Ruben Perez Dominguez
Fecha: 2023.07.08 09:35:19 +02'00'

Fdo.: José Rubén Pérez Domínguez Fecha: 07/ 07/ 2023

SIMULACIÓN SOBRE ENGRANAJES HELICOIDALES DE MATERIAL PLÁSTICO MEDIANTE MÉTODO DE ELEMENTOS FINITOS

Autor: Moro García, Ángel.
Director: Pérez Domínguez, José Rubén.
Entidad Colaboradora: ICAI – Universidad Pontificia Comillas

RESUMEN DEL PROYECTO

El objetivo principal de esta tesis es simular el patrón de contacto y el comportamiento de deformación de un par de engranajes helicoidales cruzados fabricados con un material polimérico. Para ello, se ha construido un modelo de simulación, partiendo de la geometría 2D para realizar un análisis de sensibilidad del engrane. A continuación, se ha ampliado a la geometría 3D y simulado un ciclo de engrane completo del par de engranajes investigado; en el caso concreto de esta geometría, esto significa una rotación del engranaje de 9º. Finalmente, los resultados obtenidos corresponden con las presiones y deformaciones que sufre el diente del engranaje durante el ciclo completo de engrane y se ha representado tanto de forma individual como la trayectoria conjunta de engrane

Palabras clave: Elementos finitos, simulación de deformaciones y tensiones, análisis mecánico, engranajes de plástico, estudio de sensibilidad de malla.

1. Introducción

Hoy en día, la electrificación es un tema de gran importancia en todos los sectores, como la aviación, el transporte por carretera o incluso la industria automovilística comercial. El lento cambio de los vehículos de combustión a los de propulsión eléctrica ha incrementado la demanda de motores eléctricos y ha aumentado la investigación sobre la mejor manera de implantar este nuevo tipo de motor en las cadenas cinemáticas existentes. Se demandan motores eléctricos lo más compactos posible para una amplia gama de aplicaciones, como la tecnología médica o la robótica; estos motores también se utilizan cada vez más en medios de transporte como las bicicletas eléctricas [Bos23] o los patinetes eléctricos [DSM23].

Para que estas aplicaciones sean eficientes desde el punto de vista de los recursos, el consumo de material debe ser lo más bajo posible, por lo que los conceptos de diseño ligero son esenciales. Esto puede lograrse con el uso de cajas de engranajes, lo que hace posible el uso de motores

más pequeños para una amplia gama de aplicaciones, pero estas cajas de engranajes tienen dos inconvenientes principales: el peso extra y los requisitos de espacio.

Con el fin de superar estos dos problemas principales, en el pasado se han investigado diferentes tipos de disposiciones de cajas de engranajes para reducir al mínimo la demanda de espacio y, con la incorporación de las tecnologías de impresión 3D, se ha hecho posible la fabricación de estas cajas de engranajes en materiales plásticos, lo que permite reducir el peso total del sistema.

Los reductores de engranajes cilíndricos, helicoidales y cónicos ofrecen muchas ventajas para este tipo de aplicaciones debido a la elevada relación de transmisión posible en una sola etapa. Además, los reductores de engranajes cilíndricos y cónicos también ofrecen un ángulo de cruce de ejes libremente seleccionable. Estas características permiten desarrollar accionamientos que ahorran espacio y recursos.

2. Descripción del modelo/sistema/herramienta

En el marco de la tesis, se desarrollará y evaluará una simulación de engranajes de prueba con engranaje plástico en lo que respecta a las deformaciones y la distribución global de tensiones de sus componentes. Para ello, se desarrollará un modelo de simulación, de forma que los resultados finales puedan compararse posteriormente con un experimento real y utilizar esta configuración de simulación como referencia para futuros análisis de cajas de cambios, incluyendo el análisis de diferentes geometrías y ensamblajes.

Para ello se parte inicialmente de un modelo CAD desarrollado en SOLIDWORKS, que se observa en la siguiente imagen, y que posteriormente será adaptado y modificado para su uso en ANSYS, programa empleado para su simulación.

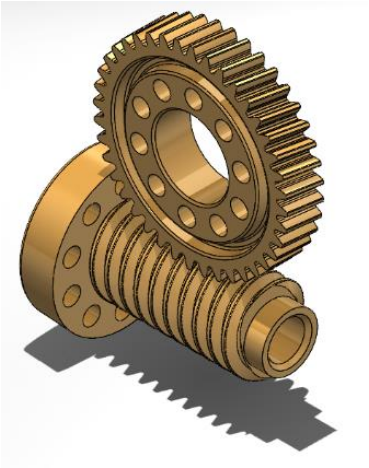


Ilustración 1: modelo CAD de engranajes

Para lograr simular los esfuerzos y deformaciones de dicho conjunto, se deben desarrollar unas fases previas como, por ejemplo: ajuste y limpieza de la geometría, desarrollo de la malla y parámetros de refinado, definición de condiciones de contorno, aplicación de fuerzas y finalmente ajustar los parámetros de la simulación. Después de todos estos pasos, se podrán obtener unos resultados que serán tratados posteriormente para su representación dentro del mismo programa de ANSYS y mediante el uso de programas externos como MATLAB a través de código. En la siguiente imagen se puede observar un esquema del proceso necesario para llevar a cabo la simulación.

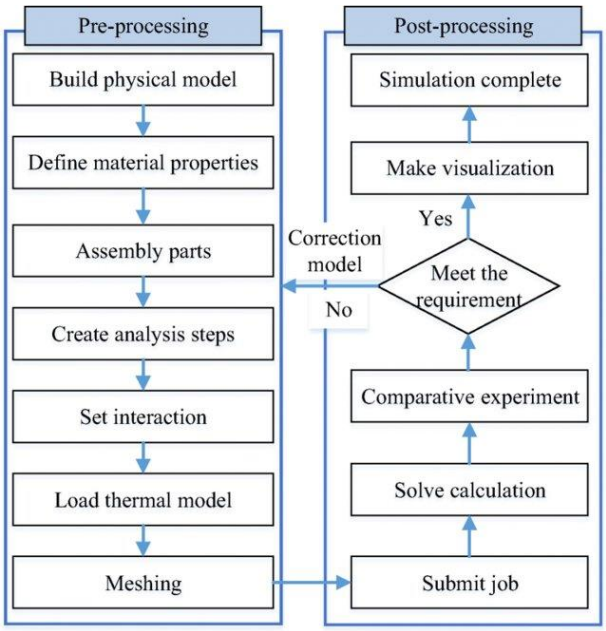


Ilustración 2: pasos para llevar a cabo una simulación exitosa

Con la intención de elegir de forma idónea todos los parámetros requeridos para ajustar el modelo de forma más fiel a la realidad, previa a la simulación final, se ha realizado un estudio de sensibilidad de malla sobre contactos de Hertz, que se trata de estudios de contactos entre geometrías sencillas que poseen solución analítica y sirven de base para calcular errores cometidos en la simulación.

3. Resultados

En cuanto a los resultados, como se ha comentado anteriormente, principalmente se han obtenido datos sobre las presiones y deformaciones de la geometría bajo una serie de condiciones de contorno determinadas. En las siguientes imágenes se mostrarán algunas de las gráficas extraídas pertenecientes a la simulación usando como material PEEK reforzado.

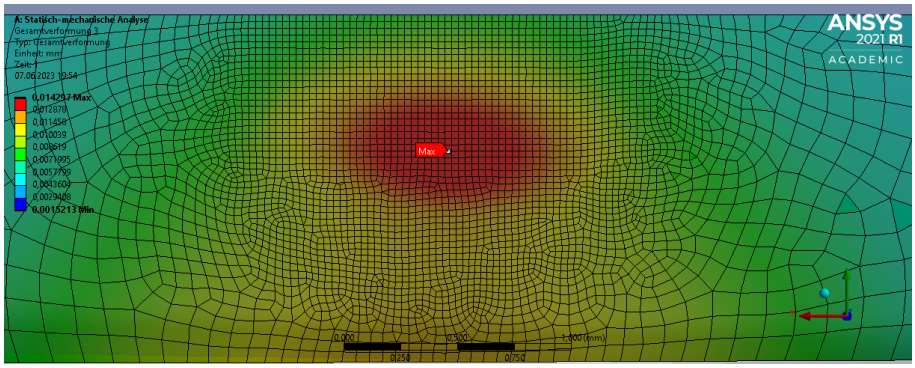


Ilustración 3: elipse de deformación en la cara de contacto del diente

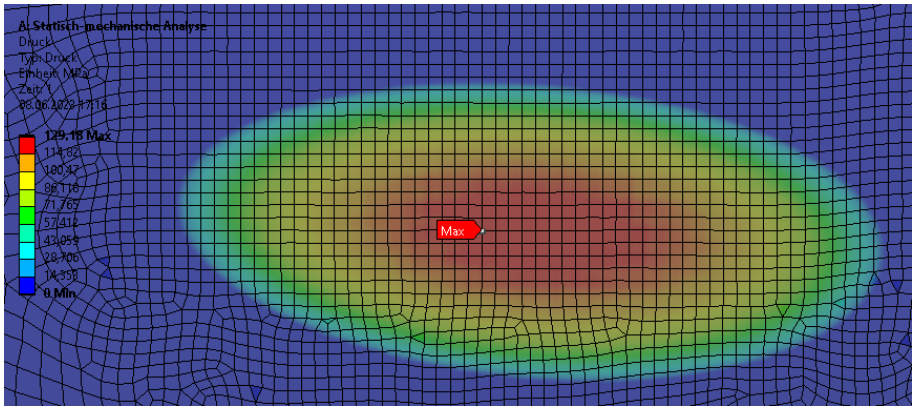


Ilustración 4: elipse de presiones en la cara de contacto del diente

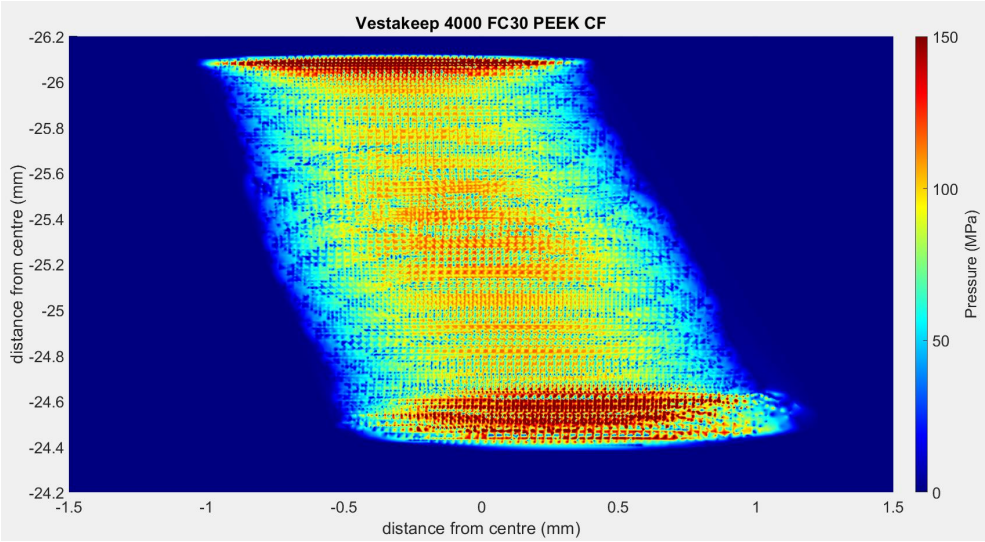


Ilustración 5: trayectoria de presiones global durante todo el contacto

4. Conclusiones

Finalmente, las conclusiones a las que se han llegado es que en cualquier simulación se está cometiendo un mínimo de un 5% de error que debe añadirse como banda de tolerancia a los resultados finales. Adicionalmente, los resultados concuerdan con los datos esperados de presiones, siendo estas mayores justo al inicio y al final del contacto, pero difieren ligeramente de los datos obtenidos mediante otros programas de simulación que emplean técnicas de simulación diferentes, por lo que hay que quedar a la espera de disponer de datos obtenidos de un ensayo en un banco de pruebas para confirmar que tipo de simulación es más correcta para este caso concreto.

SIMULATIVE INVESTIGATION ON THE CONTACT PATTERN OF POLYMER CROSSED HELICAL GEARS BY FEM

Author: Moro García, Ángel.
Supervisor: Pérez Domínguez, José Rubén.
Collaborating Entity: ICAI – Universidad Pontificia Comillas

ABSTRACT

The main objective of this thesis is to simulate the contact pattern and the deformation behavior of a pair of crossed helical gears manufactured with a polymeric material. For this purpose, a simulation model has been built, starting from the 2D geometry to perform a sensitivity analysis of the gear. Then, it has been extended to the 3D geometry and simulated a complete meshing cycle of the investigated gear pair; in the specific case of this geometry, this means a gear rotation of 9º. Finally, the results obtained correspond to the pressures and deformations that the gear tooth undergoes during the complete meshing cycle and have been represented both individually as well as the joint meshing path.

Keywords: Finite elements, stress and strain simulation, mechanical analysis, plastic gears, mesh sensitivity study.

1. Introduction

Today, electrification is a major issue in all sectors, such as aviation, road transport or even the commercial automotive industry. The slow shift from combustion vehicles to electric propulsion has increased the demand for electric motors and increased research into the best way to implement this new type of motor in existing powertrains. Electric motors that are as compact as possible are in demand for a wide range of applications, such as medical technology or robotics; these motors are also increasingly used in means of transportation such as electric bicycles [Bos23] or electric scooters [DSM23].

For these applications to be resource-efficient, the material consumption must be as low as possible, so lightweight design concepts are essential. This can be achieved with the use of gearboxes, which makes it possible to use smaller motors for a wide range of applications, but these gearboxes have two main drawbacks: extra weight and space requirements.

In order to overcome these two main problems, different types of gearbox arrangements have been investigated in the past to minimize space requirements and, with the incorporation of 3D printing technologies, it has become possible to manufacture these gearboxes in plastic materials, thus reducing the overall weight of the system.

Helical, helical and bevel gearboxes offer many advantages for this type of application due to the high transmission ratio possible in a single stage. In addition, helical and bevel helical gear units also offer a freely selectable shaft crossover angle. These features make it possible to develop space- and resource-saving drives.

2. Description of the model/system/tool

Within the framework of the thesis, a simulation of test gears with plastic gearing will be developed and evaluated with regard to the deformations and the overall stress distribution of its components. For this purpose, a simulation model will be developed, so that the final results can later be compared with a real experiment and this simulation setup can be used as a reference for future gearbox analyses, including the analysis of different geometries and assemblies.

For this purpose, the starting point is a CAD model developed in SOLO CAD model developed in SOLIDWORKS, which can be seen in the following image, and which will be image, which will later be adapted and modified for use in ANSYS, program used for its simulation.

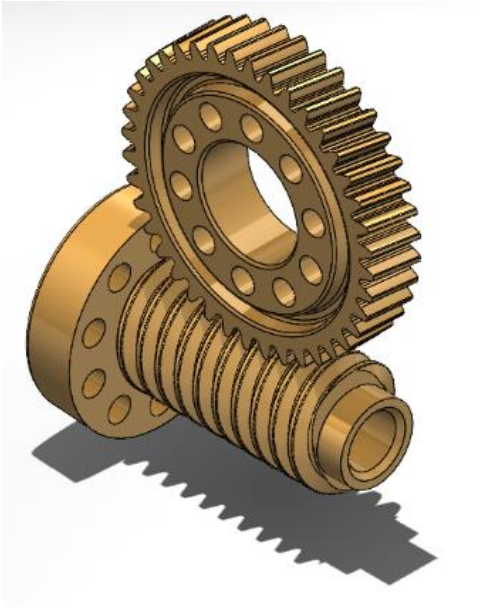


Image 1: CAD model of gears

To be able to simulate the forces and deformations of this set, some previous phases must be developed, such as: adjustment and cleaning of the geometry, development of the mesh and refining parameters, definition of boundary conditions, application of forces and finally adjusting the parameters of the simulation. After all these steps, you can obtain results that will be further processed for representation within the same ANSYS program and through the use of external programs such as MATLAB through code. In the following image you can see a scheme of the process necessary to carry out the simulation.

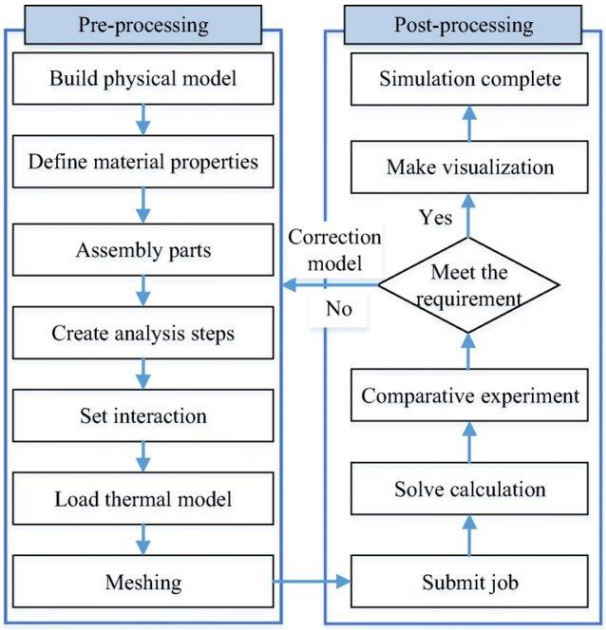


Image 2: steps to perform a successful simulation.

In order to make the best choice of all the parameters required to adjust the model more closely to reality, prior to the final simulation, a mesh sensitivity study was carried out on hertz contacts, which are studies of contacts between simple geometries that have an analytical solution and serve as a basis for calculating errors committed in the simulation.

3. Results

As for the results, as mentioned above, we have mainly obtained data on the pressures and deformations of the geometry under a series of given boundary conditions. The following images show some of the graphs extracted from the simulation using reinforced PEEK as material.

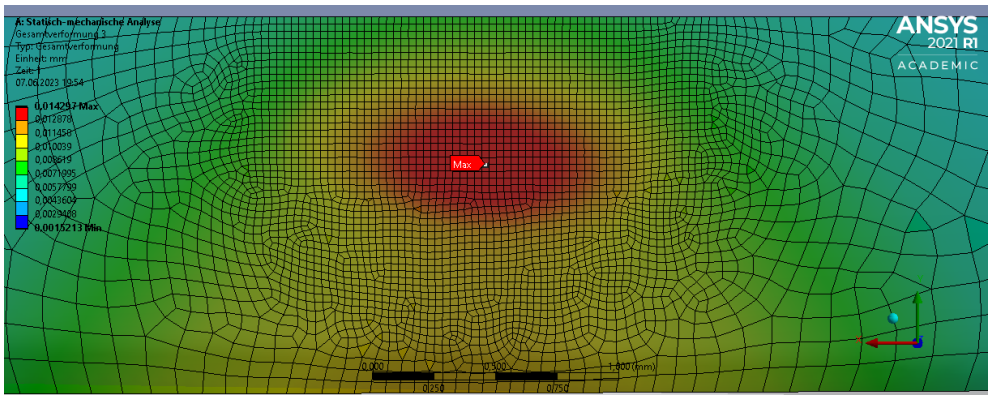


Image 3: deformation ellipse of contact surface at gear's tooth

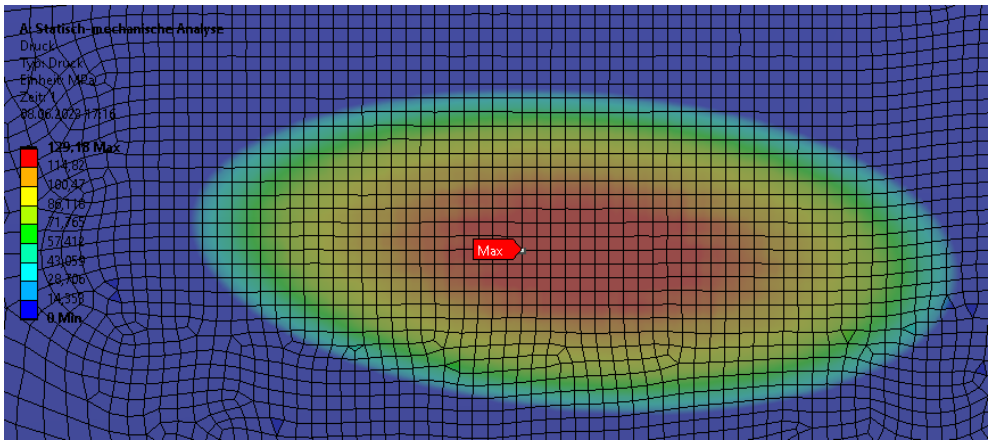


Image 4: stress ellipse at contact surface at gear's tooth

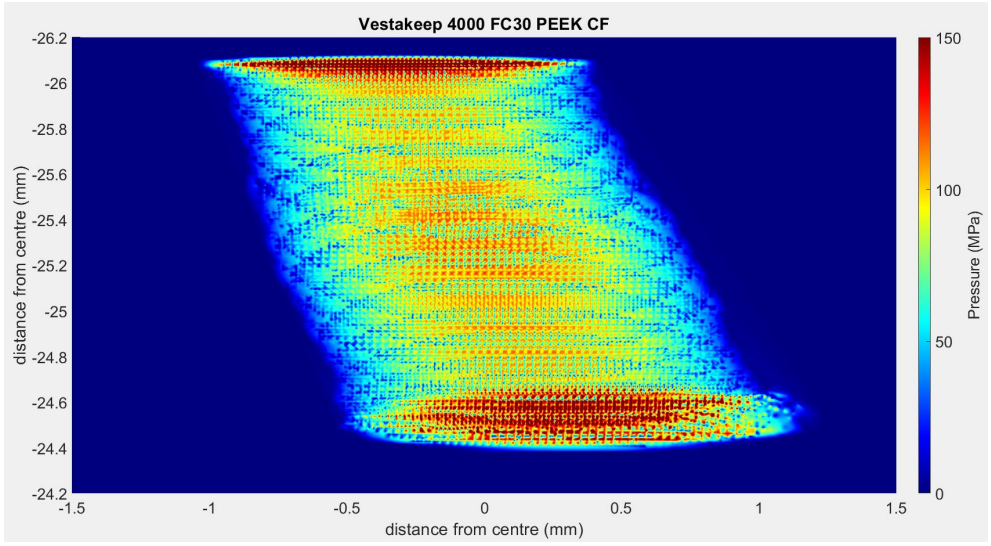


Image 5: contact path trayectory displaying stresses during complete conctact cycle

4. Conclusions

Finally, the conclusions reached are that in any simulation a minimum of 5% error is made and should be added as a tolerance band to the final results. Additionally, the results agree with the expected data of pressures, being these higher just at the beginning and at the end of the contact but differ slightly from the data obtained by other simulation programs that use different simulation techniques, so it is necessary to wait for data obtained from a test in a test bench to confirm what type of simulation is more correct for this particular case.

Table of contents

1 INTRODUCTION 1

1.1 STARTING POINT AND PRESENTATION OF THE PROBLEM 2
1.2 GOALS DEFINITION AND SOLUTION 3

2 STATE OF THE ART 5

2.1 FUNDAMENTALS OF GEARBOXES 5
2.1.1 WORKING PRINCIPLE OF A GEARBOX 7
2.2 DIFFERENT TYPES OF GEARBOXES AND THEIR APPLICATIONS 9
2.2.1 SPUR GEARS 9
2.2.2 PLANETARY GEARS 10
2.2.3 CROSSED HELICAL GEARS 12
2.2.4 BEVEL GEARS 13
2.2.5 WORM GEARS 14
2.3 INTRODUCTION TO PLASTIC GEARS 15
2.4 FUNDAMENTALS OF FINITE ELEMENT METHOD (FEM) 17
2.4.1 SIMULATION STEPS 18
2.4.2 GEOMETRY GENERATION AND ADAPTATION 20
2.4.3 MESH GENERATION 20
2.4.4 SOLVER 22
2.4.5 POST-PROCESSING 23

3 HERTZIAN CONTACTS 24

3.1 CYLINDER-CYLINDER CONTACT 25
3.1.1 GEOMETRY GENERATION 27
3.1.2 FIRST STRATEGY MESH GENERATION 29
3.1.3 MESH QUALITY EVALUATION 31
3.1.3.1 Element quality 31
3.1.3.2 Aspect ratio 33
3.1.3.3 Skewness 35
3.1.3.4 Orthogonal quality 37
3.1.4 CONTACT DEFINITION 38
3.1.5 BOUNDARY CONDITIONS 39

3.1.6 ELEMENT ORDER EVALUATION 40
3.1.7 RESULT EVALUATION OF FIRST REFINEMENT GEOMETRY 43
3.1.8 CONCLUSIONS 46
3.1.9 SECOND MESH GENERATION AND BOUNDARY CONDITIONS 48
3.1.10 THIRD MESH GENERATION AND BOUNDARY CONDITIONS 50
3.1.11 VALIDATION OF THE RESULTS 54
3.2 SPHERE-SPHERE CONTACT 55
3.2.1 GEOMETRY GENERATION 55
3.2.2 MESH GENERATION AND BOUNDARY CONDITIONS 56
3.2.3 REFINEMENT RADIUS DETERMINATION 58
3.2.4 REFINEMENT SIZE DETERMINATION 60
3.2.5 QUALITATIVE VALIDATION OF THE RESULTS 62
3.3 CONCLUSIONS OF MESH SENSITIVITY ANALYSIS 63

4 GEARBOX SYSTEM SIMULATION 65

4.1 GEOMETRY GENERATION AND MODIFICATION 65
4.2 ENGINEERING DATA 67
4.3 GEOMETRY 69
4.4 MODEL (MESH) 75
4.5 SETUP 78
4.5.1 CONTACT DEFINITION 78
4.5.2 BOUNDARY CONDITIONS 81
4.6 RESULTS (FRICTIONLESS) 82
4.7 RESULTS (WITH FRICTION) 89

5 VALIDATION OF THE RESULTS 95

6 SUSTAINABLE DEVELOPMENT GOALS 106

6.1 BUILD RESILIENT INFRASTRUCTURE, PROMOTE INCLUSIVE AND SUSTAINABLE INDUSTRIALIZATION AND FASTER INNOVATION [Uni23] 106
6.2 "ENSURE SUSTAINABLE CONSUMPTION AND PRODUCTION PATTERNS" [UNI23] AND NUMBER 13 "TAKE URGENT ACTION TO COMBAT CLIMATE CHANGE AND ITS IMPACTS" [UNI23]. 107

7 SUMMARY AND OUTLOOK 108

8 BIBLIOGRAPHY 111

9 ANNEX 117

9.1 MATERIAL PROPERTIES AND GEOMETRIC DATA OF THE SIMULATED GEAR 117

9.2 MATLAB SOURCE CODE FOR PLOTTING CONTACT PATH DATA 127

List of figures

FIGURE 1: ANNUAL GLOBAL ELECTRIC VEHICLE SALES BY MARKET [KAT22, U.S11] 1
FIGURE 2: ENGINE POWER AND TORQUE CURVE [HOR20] 6
FIGURE 3: ANGULAR VELOCITY CORRELATION [TEC18] 8
FIGURE 4: SPUR GEAR WITH EXTERNAL TEETH [NIC22] 10
FIGURE 5: PLANETARY GEAR ASSEMBLY [LES23] 11
FIGURE 6: MOVEMENT COMPOSITION OF THE PLANETARY GEAR [LES23] 12
FIGURE 7: CROSSED HELICAL GEARS [LAY14] 13
FIGURE 8: SPIRAL BEVELED GEAR (LEFT) AND STRAIGHT BEVELED GEAR (RIGHT) [LAY14] 14
FIGURE 9: WORM GEAR ASSEMBLY [SAN23] 15
FIGURE 10: SEMI-CRYSTALLINE THERMOPLASTIC PROPERTIES [WUD21] 16
FIGURE 11: STEPS TO PERFORM A THERMAL-MECHANICAL SIMULATION [SON21] 19
FIGURE 12: STRUCTURE MESH (LEFT SIDE) AND UNSTRUCTURED MESH (RIGHT SIDE) [GIG20] 21
FIGURE 13: STRUCTURE MESH LAYOUTS. H GRID, C GRID AND O GRID (FROM LEFT TO RIGHT) [GIG20] 22
FIGURE 14: CYLINDER – CYLINDER GEOMETRY 28
FIGURE 15: MESH REFINEMENT REGION DETAIL 30
FIGURE 16: MESHING EXAMPLE OF ONE OF THE SIMULATIONS 31
FIGURE 17: ELEMENT QUALITY VALUES 33
FIGURE 18: THE DISPLAY OF ELEMENTS WITH LOWER ELEMENT QUALITY THAN 0.8 33
FIGURE 19: ASPECT RATIO CALCULATION [ANS21] 34
FIGURE 20: ASPECT RATIO VALUES 34
FIGURE 21: ELEMENTS WITH A HIGHER ASPECT RATIO THAN 2 35
FIGURE 22: SKEWNESS VALUES 36
FIGURE 23: VECTORS USED TO COMPUTE ORTHOGONAL QUALITY FOR A CELL [ANS21] 37
FIGURE 24: ORTHOGONAL QUALITY VALUES 37
FIGURE 25: DISPLAY OF CONTACT REGIONS 38
FIGURE 26: BOUNDARY CONDITIONS FOR THE SIMULATION 40
FIGURE 27: LINEAR ELEMENT ORDER (LEFT) AND QUADRATIC ELEMENT ORDER (RIGHT) [ANS21] 41
FIGURE 28: QUADRATIC VS LINEAR RESULTS FOR CYLINDER–CYLINDER SIMULATION 42
FIGURE 29: PERCENTAGE ERROR OF EVERY SIMULATION 43
FIGURE 30: TIME REQUIREMENTS FOR QUADRATIC AND LINEAR ORDER SIMULATIONS 43
FIGURE 31: SIMULATION RESULTS OF REFINEMENT GEOMETRY 1 44
FIGURE 32: MESHING RESULTS OF REFINEMENT GEOMETRY 1 45

FIGURE 33: CONTACT PATTERNS WITH DIFFERENT MESH REFINEMENTS (STRESS SHOWN IN MPA) 46
FIGURE 34: FINAL RESULTS OF SENSITIVITY ANALYSIS WITH GEOMETRY 1 (STRESS SHOWN IN MPA) 47
FIGURE 35: REFINEMENT GEOMETRY 2 AND BOUNDARY CONDITIONS 48
FIGURE 36: SIMULATION RESULTS OF GEOMETRY 2 49
FIGURE 37: REFINEMENT MESH 3 50
FIGURE 38: GEOMETRY STUDY FOR OPTIMUM RADIUS 51
FIGURE 39: REFINEMENT RADII ANALYSIS (STRESS SHOWN IN MPA) 51
FIGURE 40: RESULTS OF SIMULATION GEOMETRY 3 52
FIGURE 41: RESULTS SIMULATION GEOMETRY 3 53
FIGURE 42: RESULTS COMPARISON FOR CYLINDER-CYLINDER CONTACT (LEFT SIDE [SUG21]) 54
FIGURE 43: GEOMETRY FOR SPHERE CONTACT SIMULATION 56
FIGURE 44: MESH REFINEMENT SPHERE CONTACT SIMULATION 57
FIGURE 45: BOUNDARY CONDITION SETUP SPHERE–SPHERE CONTACT 58
FIGURE 46: REFINEMENT RADII ANALYSIS SPHERE - SPHERE CONTACT 59
FIGURE 47: PLOTS OF REFINEMENT RADIUS SIMULATION FOR SPHERE CONTACT (STRESS SHOWN IN MPA) 60
FIGURE 48: MAXIMUM STRESS RESULTS OF SPHERE CONTACT 61
FIGURE 49: SIMULATION TIME FOR SPHERE CONTACT SIMULATION 62
FIGURE 50: VALIDATION OF STRESS PATTERN FOR SPHERICAL CONTACT SIMULATION 63
FIGURE 51: GEOMETRY ASSEMBLY IN SOLIDWORKS 65
FIGURE 52: GEOMETRY LOADED IN DESIGN MODELER. 69
FIGURE 53: MINIMUM DIMENSIONS TO SIMULATE AN EQUIVALENT GEAR. [FRÜ12] 71
FIGURE 54: THREAD EDGE REFINEMENT 73
FIGURE 55: FINAL GEOMETRY TO BE SIMULATED. 74
FIGURE 56: STRESS DISTRIBUTION (MPA) OF FULL GEOMETRY (LEFT) VS REDUCED GEOMETRY (RIGHT) 74
FIGURE 57: SURFACE DEFORMATION (MM) OF THE COMPLETE GEOMETRY (LEFT) VS REDUCED GEOMETRY (RIGHT) 75
FIGURE 58: POSITIONING OF THE CENTERS OF THE SPHERES OF INFLUENCE 76
FIGURE 59: ISOMETRIC VIEW OF GEAR MESH 77
FIGURE 60: CUT PLANE DISPLAYING REFINEMENT REGIONS. 77
FIGURE 61: ISOMETRIC VIEW OF WORM MESH 78
FIGURE 62: MAIN CONTACT DEFINITION 79
FIGURE 63: CONTACT STATUS OF THE THREE DEFINED CONTACTS 80
FIGURE 64: INITIAL CONTACT GAP (MM) 81
FIGURE 65: BOUNDARY CONDITIONS DEFINITION 82
FIGURE 66: SNAPSHOT OF INITIAL CONTACT STATUS (0º) 85
FIGURE 67: STRESS PATTERN OF A COMPLETE FRICTIONLESS ROTATION 86

FIGURE 68: STRESS PATTERN NEGLECTING OUTLIERS (FRICTIONLESS) 86
FIGURE 69: CONTACT PRESSURE AT THE EDGE OF THE TOOTH (TOP) VS AT PITCH DIAMETER (BOTTOM) 87
FIGURE 70: AN OVERVIEW OF PITCH DIAMETER CONTACT 88
FIGURE 71: DEFORMATION OF THE CONTACT SURFACE IN A FRICTIONLESS SIMULATION 89
FIGURE 72: SCHEMATIC COMPARISON OF THE CONTACT FORCE IN A FRICTION AND FRICTIONLESS SIMULATION [DRE16]... 91
FIGURE 73: STRESS PATTERN OF A COMPLETE FRICTIONAL ROTATION 92
FIGURE 74: STRESS PATTERN NEGLECTING OUTLIERS (FRICTIONAL) 92
FIGURE 75: SURFACE STRESS DISTRIBUTION FOR FRICTIONLESS (TOP) AND FRICTIONAL SIMULATION (BOTTOM) 93
FIGURE 76: DEFORMATION OF THE CONTACT SURFACE IN A FRICTIONAL SIMULATION 94
FIGURE 77: GEOMETRIC SHAPE OF CONTACT ELLIPSE DEPENDING ON TOTAL SHAFT ANGLE [TAM17]. 97
FIGURE 78: RESULTS OF CONTACT ELLIPSE IN FRICTIONAL SIMULATION 97
FIGURE 79: LOAD CONTACT PATTERN FOR THE MATERIAL COMBINATION STEEL/PEEK (SCHRAD2) [SOK22]..... 101
FIGURE 80: STEEL – PEEK PRESSURE DURING CONTACT PATH..... 101
FIGURE 81: LOAD CONTACT PATTERN FOR THE MATERIAL COMBINATION PEEK/PEEK (SCHRAD2) [SOK22]. 103
FIGURE 82: PEEK – PEEK PRESSURE DURING CONTACT PATH..... 104
FIGURE 83: PEEK CF – PEEK CF PRESSURE DURING CONTACT PATH 105

List of tables

TABLE 1: CHARACTERISTICS OF STRUCTURE AND UNSTRUCTURED MESHES. [GIG20] 22
TABLE 2: MECHANICAL PROPERTIES OF STRUCTURAL STEEL 29
TABLE 3: C CONSTANT VALUE FOR ELEMENT QUALITY 32
TABLE 4: CONTACT TOOL DATA 39
TABLE 5: RESULT SUMMARY TABLE 47
TABLE 6: PEEK CF – PEEK CF MECHANICAL PROPERTIES 68
TABLE 7: PEEK - PEEK MECHANICAL PROPERTIES 68
TABLE 8: PEEK - STEEL MECHANICAL PROPERTIES 68
TABLE 9: RELEVANT GEOMETRIC VALUES OF THE GEAR ASSEMBLY 70
TABLE 10: MAXIMUM STRESS IN MPA FOR FRICTIONLESS CONTACT 84
TABLE 11: MAXIMUM STRESS IN MPA FOR FRICTIONAL CONTACT 90
TABLE 12: MESH GRID FOR INTERPOLATION OF RESULTS 99

1 INTRODUCTION

Electrification has been crucial in all developed countries during the last few years. CO2 emissions and other kinds of pollution, such as NOx or O3, have heavily impacted our way of living, forcing us to change our living habits and adapt them to generate new, eco-friendlier, and more sustainable, living standards.

One of the most important and most well know changes pursuing the reduction of this type of emissions is the electrification of multiple sectors, like aviation, road transport, the automatization industry and most importantly, the commercial automotive sector.

In Europe, many countries are taking action to decarbonize the vehicle industry and achieve a fully electric vehicle network. A proposal for prohibiting the sale of new combustion vehicles by 2035 has been written to achieve the 2030 and 2050 climate objectives set by Europe [EEU].

With the increasing number of laws and restrictions on combustion vehicles, electric vehicles have become the alternative way of transportation bringing with them the main problem of maintaining the actual range that combustion vehicles offered. In Figure 1, extracted from Kathiresh et. al's. book "E-Mobility", an estimation of the number of global electric vehicle sales can be observed.

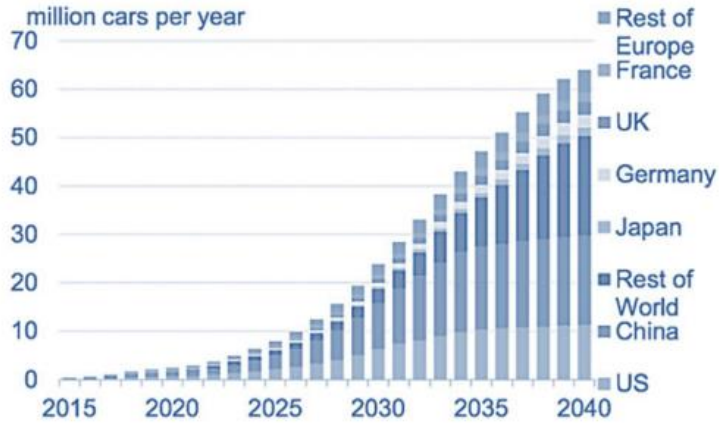


Figure 1: Annual global electric vehicle sales by market [Kat22, U.S11]

Many reasons explain why the range of electric vehicles is reduced, but the most important one is related to the car's weight and dimensions. At the moment, the battery module is really big and there are a lot of automated actions that are powered with electricity such as adjustable mirrors, electric seats, powered doors, assistance driver systems, etc. All these accessories need to be powered and controlled through an electric motor, adding a lot of extra weight, reducing the car's effective range, and making this option not so attractive to new buyers.

With the implementation of gearbox systems, the dimensions of the electric motors can be reduced, allowing them to have a better performance due to the lower weight, but this does not only apply to electric motors of electric cars, as stated by Kinnaird, "typical modern cars on American roads might easily have 40 electric motors or more" [Kin20]. Some other applications in which electric motors are present are robotics, small appliances like kitchen tools, e-bikes, scooters and many more.

1.1 STARTING POINT AND PRESENTATION OF THE PROBLEM

One of the best ways to reduce the weight of an electric drive is to include a gearbox in the system. This will allow the transformation of power into two main forms: high velocity / low torque, or low velocity / high torque applications. With this system, a much smaller motor could be chosen for a wider range of applications, allowing companies to reduce the size of the motors in all types of sectors. For example, this would have a direct application in electric-powered mirrors, electric-powered seats, industrial machines, electric bicycles offered by companies such as Bosch [Bos23], Scooter [DSM23], hand tools and many more.

In order to implement gearboxes in electrified applications, it must be as compact as possible, to avoid including extra weight due to the extra space requirements. This versatility derives from the development of multiple types of gear patterns, such as crossed helical gears (gear systems studied for this thesis).

Having said that gearbox systems help improve the efficiency of the electric motors, this is not true for all kinds of gearboxes and motors. Each application needs its gearbox systems considering space requirements, power losses, operative working range etc. due to this, a deep study for every application needs to be done and, in this thesis, a specific gearbox system will be studied in depth to analyze its usability.

The thesis aims to create a setup for a specific gear type, allowing it to perform a higher number of tests while reducing the testing cost and increasing the number of variations and models that can be tested in a restricted amount of time.

1.2 GOALS DEFINITION AND SOLUTION

As mentioned in the previous paragraph, the goal of this thesis is to generate a simulation setup that allows simulating a specific type of gear assembly in order to check how it behaves under certain loads, how it deforms and if any type of redesign is needed in order to perform in its optimal conditions.

Once this setup is created, the studied gear assembly can be checked for its compatibility with the application that was thought for. The tools needed for the creation of the setup are first a mesh sensitivity analysis that shows the dependency of the results based on mesh variations and estimates the percentual error introduced by the mathematical models. Based on the results, the mesh for the final simulation will be computed and the boundary conditions will be assigned. Finally, the results obtained could be validated as future work based on real-life testing results obtained from a test rig.

Another future study following this thesis is performing a more in-depth study of the design of every component of the gearbox, allowing to reduce the testing cost and time, like the bearings, fixing elements, casing, etc.

2 STATE OF THE ART

In the following section, there will be an explanation of the main topics that the scope of the thesis involves. First, an overview of the working principles of a gearbox will be explained, highlighting why it brings different benefits in this and other applications. Following this chapter, a deeper understanding of different gearbox systems will be explained, including the pros and cons of every system and their possible applications. Last but not least, the concept of FEA (Finite Element Analysis) will be introduced and an explanation of why this is a huge improvement in these types of research studies will be given.

2.1 FUNDAMENTALS OF GEARBOXES

As has been explained in the introduction, a gearbox system is created to transform the power output of the system. The most well-known application of a gearbox system nowadays is on automotive vehicles, but these systems have evolved and have been improved massively during the last years.

The first reported transmission on a passenger car was dated in 1894, with the three-speed manual transmission of Panhard et Levassor according to Collins [Col19]. Over the years, as cars have been able to reach higher speeds, a larger number of gears have been introduced in these gearbox assemblies, reaching today to 9 and 10 speeds in automatic transmissions, as stated in the following article about automatic transmissions [Wik23], and usually, 6 speeds in manual transmissions, as Auto Simple affirms in his article [Aut17].

The main purpose of using a gearbox is to allow the engine to work in its most effective operating RPM (revolutions per minute) range for a longer period. Figure 2 shows a standard engine's power / torque to angular velocity graph.

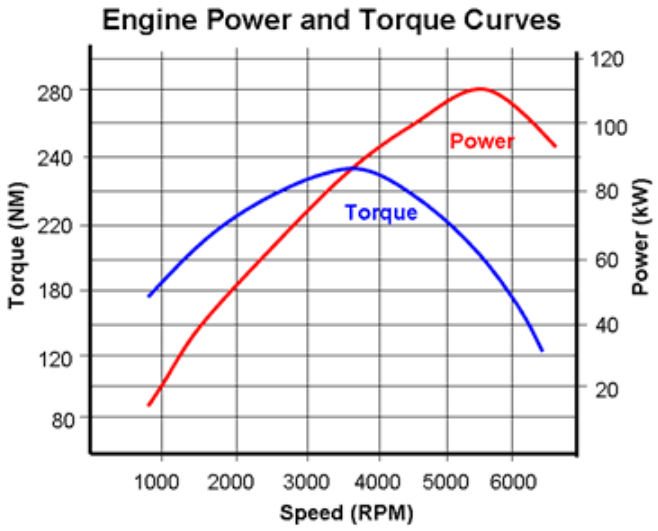


Figure 2: engine power and torque curve [Hor20]

As seen in Figure 2, the torque curve of an engine has an inverted U shape, reaching the peak torque or moment somewhere around the middle of its RPM range. Taking into consideration the equation for the power output, this value can also be derived from this information.

$$P = M \cdot \omega = F \cdot v \tag{1}$$

P	Watt	Power	M	Nm	Moment
ω	Rad/s	Angular velocity	F	N	Force
v	m/s	Velocity			

The first interesting conclusion that can be observed is, that the peak power is reached much later than the peak torque and the second conclusion is, that after a certain RPM, the engine torque decreases considerably deriving in a steep decrease in the power output of the motor. [Hor20]

Due to this last effect, the goal of a gearbox is, that once the engine enters into the steep power decrease range, the actual gear ratio is decoupled, and a new gear ratio is coupled to the system, reducing the engine RPMs back to the start of its operative range and making again all the power available while maintaining the speed.

By doing this, the engine is allowed to work on a much wider range and is also capable of performing on its optimal range on many more applications, as its velocity and momentum can be almost freely adapted to each case. This is the main reason why with electric motors, the addition of a gearbox is so powerful, making possible the usage of smaller motors for more applications saving space and weight.

2.1.1 WORKING PRINCIPLE OF A GEARBOX

As has been shown in *Equation $P = M \cdot \omega = F \cdot v$* (1), power can be expressed in a linear or angular way. In the case of a linear movement, it depends on force and linear velocity and if the movement is rotational, then it depends on the moment and angular velocity.

As the power must be transmitted through the gears in a gearbox assembly (a percentage of the power is lost due to efficiency and friction forces in the form of heat), when the velocity increases the moment decreases and the other way around.

As it is explained by Vullo in his book [VUL21], a moment cannot be enforced, but velocity can, and it is done due to the gear's teeth. With the ratio between the teeth of the big and the smaller wheel, a velocity ratio between the gears is enforced, as the teeth prevent the slippage of the gears and force the same linear or tangential velocity for both gears in their contact point. Then the linear velocity is transformed into rotational velocity and with this value, the moment transmitted in each gear can be calculated. This equation can also be expressed with forces. In this case, the velocity will refer to the force and the angular velocity the moment that is transmitted through the wheels.

$$v_c = \omega_1 \cdot r_1 = \omega_2 \cdot r_2 \quad (2)$$

v_c	m/s	Linear velocity in contact point	r_n	m	Radius of gear n
ω_n	Rad/s	Angular velocity of gear n			

$$F = M_1 \cdot r_1 = M_2 \cdot r_2 \quad (3)$$

F	N	Contact force	r_n	m	Radius of gear n
M_n	N/m	Moment of gear n			

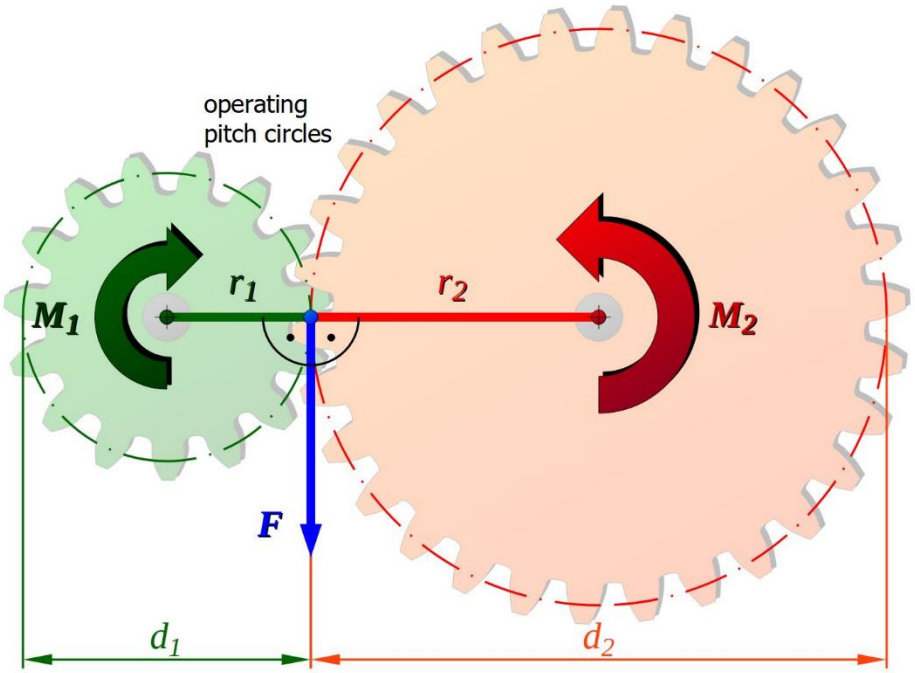


Figure 3: angular velocity correlation [tec18]

2.2 DIFFERENT TYPES OF GEARBOXES AND THEIR APPLICATIONS

Once the basic working principle of a gearbox has been explained, in this next chapter, different gearbox assemblies will be analyzed in terms of their pros and cons with a short introduction to their application.

As motor-powered systems are present in many types of machinery and professional sectors such as medical tools, or day-to-day objects like a watch, its gearbox system needs to be as versatile as possible, to ensure a good fit in every application and due to that, many different types of combinations have been developed and implemented during the last years. In this thesis the 6 main types will be discussed, being these spur gears, planetary gears, crossed helical gears, bevel gears, crown gears and worm gears.

2.2.1 SPUR GEARS

As Errichelo [Err13] states, spur gears are the simplest of all types consisting of a cylindrical body that has multiple teeth, parallel to the gear axis, that can be located internally or externally, depending if the teeth are projected outwards or inwards [Wan13a]. This type of gear is the simplest geometry that can be used. They are mainly used for driving technology due to their easy and controllable dimensioning and cheap fabrication. The main characteristic of this type of gear is that the teeth are oriented in the same direction as the shaft, meaning that no angle change can be possible between both connected shafts [Err13]. This can be a limiting factor for its application in areas where the space requirement needs to be very low, and a compact design is necessary.

Regarding the contact pattern, these assemblies have a line contact pattern with only one tooth in contact at the same time [Err13]. This creates higher vibrations, noise, and a variable load-carrying operation according to Nice and Hall-Geisler [Nic22]. When the gears are in contact, the load is transmitted through the teeth which contact is active, but when this contact disappears, the gears accelerate until the next teeth pair comes into contact, creating an uneven load transport with spikes in forces during its application. This shift between teeth contact pairs is

also the cause of the noise during operation. One benefit of this type of gear is that, due to the teeth having the same direction as the shaft, the load force is always transmitted in the tangential direction, having no load in the axial direction, making the mounting, and fixing of this type of gear much easier and cheaper in comparison with another type of gear geometries [Err13].

In Figure 4, one type of spur gear is shown, in this case, it is a spur gear with external teeth.



Figure 4: spur gear with external teeth [Nic22]

2.2.2 PLANETARY GEARS

These gears are much more complex than standard spur gear systems but are based on the same working principles. A base planetary gear system is formed by a sun gear (dark green), multiple planet gears (grey), the ring gear (light green) and a carrier, that connects all the planet gears (red). In the following picture, a representation of this assembly is shown. [Les23]

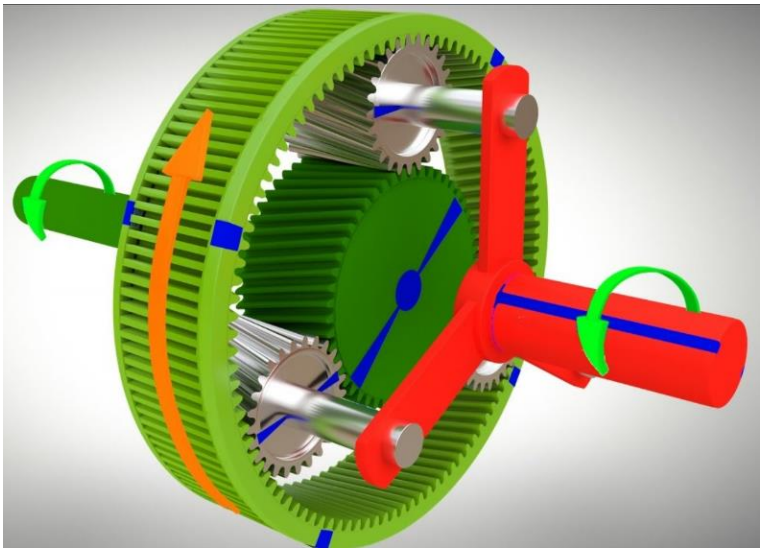


Figure 5: planetary gear assembly [Les23]

According to Pullen, this type of gear system is commonly used in automatic transmissions due to its high number of ratio combinations possible depending on which part stays fixed and where the input of movement is located [Pul23]. To increase the number of combinations, multiple planetary gears can be placed in series connecting the carrier of the planetary gears system to the sun of the next planetary assembly. This type of layout also allows the creation of a backwards gear used in multiple automotive gearboxes. According to Crispel et. al., this type of gearbox is very common also in robotics, where a high-revolution electric motor trades its high velocity for high torque with this type of transmission [Car19, Cri19].

Its working principle depends on which part stays static and which parts are free to rotate. For example, if the ring gear is held static and the input is located at the sun gear, the planet gears are forced to rotate around its axis and also rotate around the sun axis. This is the only way in which both velocity conditions can be fulfilled simultaneously, the linear velocity forced by the sun gear at the contact point between the sun gear and the planet gear and the static condition at the contact point between the planet gears and the ring gear. [Les23]

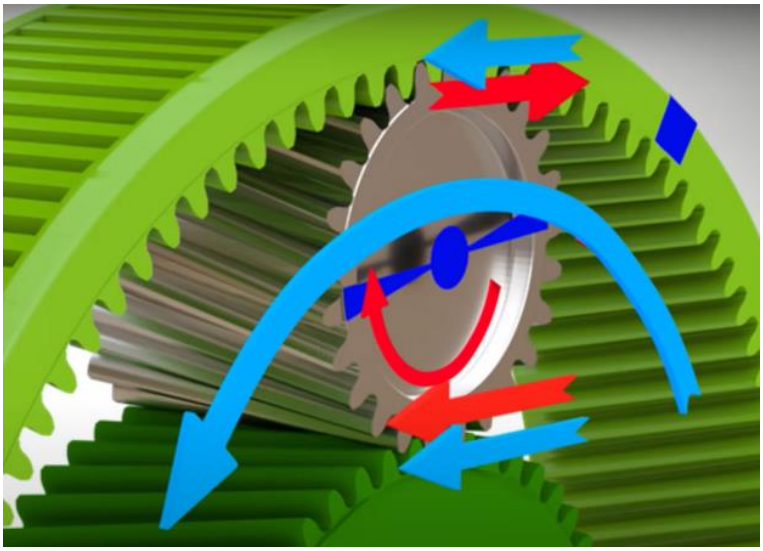


Figure 6: movement composition of the planetary gear [Les23]

By this composed movement, the rotation around its proper axis forces two tangential velocities in both contact points with different directions (showed in red), but the rotation of the planet gear around the sun enforces two different tangential velocities, this time with the same direction (showed in blue). Both velocities on top cancel out generating the 0-velocity requirement in the contact point, while the two velocities on the bottom add up generating the rotation of the wheels [Les23].

Varying the combination of static and input gears a huge amount of ratio combinations can be derived for this system, creating a very compact solution in the axial direction.

2.2.3 CROSSED HELICAL GEARS.

Crossed helical gears are the layout that will be simulated in this thesis. As explained by Niemann et. al. [Nie11], they consist of two gears that have different helix angles on their teeth. This means that the teeth are not parallel anymore to the shaft direction as happened with spur gears. The addition of this angle generates a new degree of freedom in the system, allowing to pair shafts with an angle between 0 and 90 degrees. This gives a huge versatility to the system

making possible extremely compact solutions but has also some disadvantages in comparison with spur gears.

As a helix angle is present on the teeth of the gears, the contact is not a line contact anymore, in this case, a point contact is present, localizing the carried load. This creates a less uniform load distribution causing stress spikes at the contact point and thus they require better material properties to withstand the high stress generated on the contact point [Nie11]. It must be mentioned also the increased degradation of the teeth due to the localized force and the increased temperatures the teeth suffer during operation. On the other hand, a much smoother contact behavior can be observed, as more teeth can be in contact at the same time allowing a good point load transition between the teeth coming out and coming into contact. This also derived in better vibration behavior and lower noise during operation according to Layosa [Lay14].



Figure 7: crossed helical gears [Lay14]

2.2.4 BEVEL GEARS

According to Klingelnberg et. al. [Kli08], This type of gear did not have a relevant use until the development of the automotive industry in the 20th century, when they were used in order to transmit the torque to the rear axle of cars while having a rear differential. Bevel gears are

characterized by having two shafts at a 90-degree angle crossing axis, although other angles could be achieved. This type of gear allows all types of teeth geometries, from straight standard teeth to complex helical teeth. The most important characteristic of this layout relies on the fact that one of the axes is allowed to move rotating around the axis of the other axis [Lay14].

Due to the freedom of choosing different diameters for both axes, this setup is usually used in applications where a high conversion ratio is needed while maintaining a very compact design.

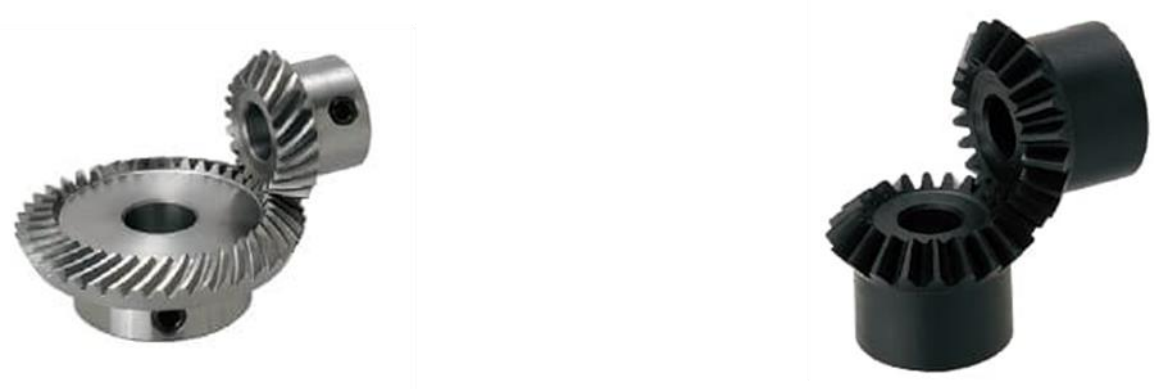


Figure 8: spiral beveled gear (left) and straight beveled gear (right) [Lay14]

2.2.5 WORM GEARS

This type of gear is a specific layout inside helical gears explained in Chapter **¡Error! No se encuentra el origen de la referencia.**. In this case, one of the gears is a worm screw, which typically has a much smaller diameter than a usual gear, making this type of assembly the best option to transmit big amounts of torque and for applications that need extremely high conversion ratios in one single stage as stated by Santram Engineers [San23].

As such huge ratios can be achieved with this setup, it is also ideal for compact solutions that have their shafts at a 90-degree angle. There is one more difference between worm gears and crossed helical gears and it is related to the teeth pattern. In crossed helical gears it has been explained that the teeth have the same geometry as spur gears but with a certain inclination

angle. In this application, the teeth geometry has an irregular thickness distribution, that allows the teeth to achieve a line contact pattern instead of a point contact pattern of the helical gears.

This means that it avoids all the disadvantages of point contact layouts while maintaining its extremely compact design. The biggest disadvantage of this type of gear is its high cost of manufacturing [San23].

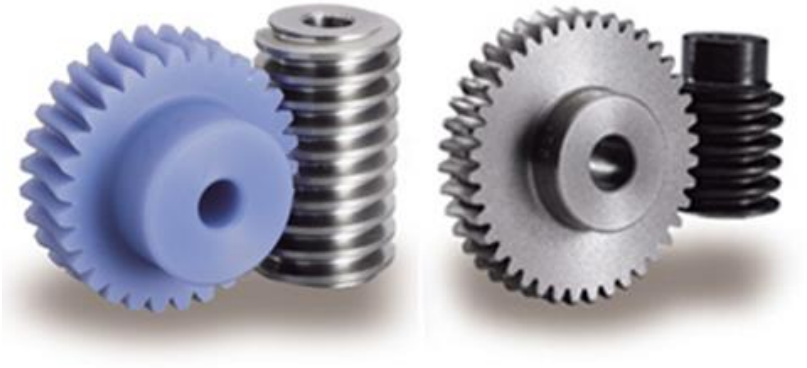


Figure 9: worm gear assembly [San23]

2.3 *INTRODUCTION TO PLASTIC GEARS*

Another possibility to reduce the weight of the system and make the gearing mechanism more affordable is changing the material of the gears. In the past, most of the gears were made out of metal, but with the increasing 3d printing sector and the improvement in the development of new plastic materials, this type of material can also be considered in certain applications. According to Radzevich, "semi-crystalline thermoplastics are mainly used as gear materials." [Rad22], with the following stated as particularly relevant: high-molecular polyethylene of high density (PE-HD), polyoxymethylene (POM), polyamide (PA), polybutylene terephthalate (PBT) and polyetheretherketone (PEEK).

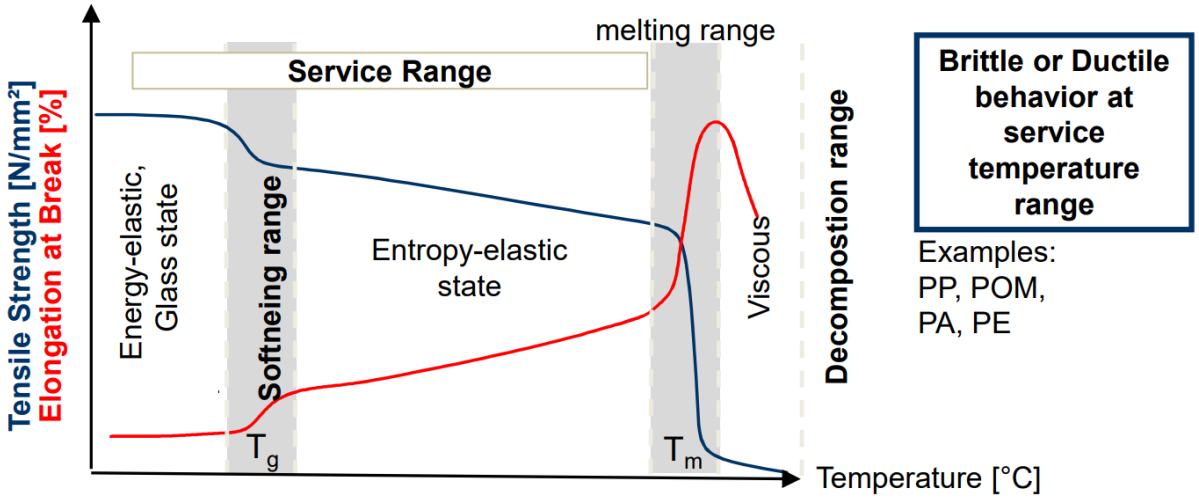


Figure 10: semi-crystalline thermoplastic properties [Wud21]

As translated from Fürstenberg's dissertation [Für13], usually in a gear pair, one of the gears is made of plastic and the other one is made of metal, due to the heat generated while working. If both gears would be made out of plastic, they would eventually melt and because of that a material with high thermal conductivity is needed in the gear pair making possible the exit of the generated heat.

Another further advantage of this type of material is that their properties can be changed with some heating treatments and by the addition of other components as Mandt et al. [Man22] and Kurokawa et al. [Kur03] affirm in their books.

The following main mechanical properties of thermoplastics are gathered in Hasl's dissertation [Has18] and the following bibliography [Ehr11, Erh78, Gre21, Sto12]:

- Properties are strongly time and temperature dependent.
- Time-dependent properties mean that extreme caution needs to be considered for short time stresses vs long time stresses.
- Elastic and plastic creep under sustained stress.
- Modulus of elasticity of thermoplastics increases with decreasing temperature.
- An increase in the elongation rate is qualitatively comparable with decreasing temperature, and the modulus of elasticity increases.

- Due to the temperature-dependent elasticity, these are usually given for different temperature levels.

It must also be remarked that the deformation of this material is divided into three different areas: elastic, viscoelastic and viscous deformation, only the last one non-reversible. The deformation depends on factors such as material, stress level, time and temperature [Has18]. One last important characteristic is that this material has no fatigue strength in comparison with steel [Has18, Nie03].

The use of plastic gears also allows a much easier manufacturing process and a higher versatility in the design process of the gears with the implementation of 3D printing technologies. Considering the type of material needed for this application, the best manufacturing method needs to be evaluated, because not all 3D printing systems allow every plastic type. More information on 3d printing principles and technologies can be found in "Guide to Additive Manufacturing" by Godec et. al. [God22a, God22b].

More information about plastic material for gears and about its manufacturing process could be found in the following documents [Ans01, Für13, Ver16]

2.4 *FUNDAMENTALS OF FINITE ELEMENT METHOD (FEM)*

During the last few years, there has been an incredibly fast improvement and development of engineering in multiple different research areas, and this comes paired with a lot of hours of testing to check if the improvements are applied correctly or if the design needs changes and improvements. This testing process is mainly slow and expensive. Every time some testing is needed, first, the object that is going to be tested needs to be produced and fabricated, after its final design, then it needs to be tested at the adequate testing bench or facility, and then a system for collecting all the data extracted from the test needs to be purchased. Once this process is finished, the data is evaluated and in case of getting results that were not expected, this whole process needs to be repeated completely.

With the introduction of simulation software, all this testing procedure has become much simpler and easier, not only in terms of saving time and money but also because it allows studying behaviors and scenarios that in other ways wouldn't be possible like testing in extremely high or low temperatures, under controlled environments or with extreme forces.

At the moment multiple types of software can perform simulations of any kind, for example, aerodynamics for external flow simulations, internal tube simulations, chemical simulations, thermal simulations, or mechanical simulations, the one that will be performed in this case. For this case, the simulations will be performed using ANSYS, although other software for gear simulations are also valid for this type of testing like, for example ABACUS.

This technology has been present for many years, but due to the high computational demand, its usage has increased massively since 1940 according to Fritscher [Fri93].

As Whiteley defines in his book, the main working principle of the finite element method is very simple first of all, the domain where the differential equation is defined is divided into multiple small regions called elements, and in each of these elements, the corresponding equations are evaluated and solved using a low-order polynomial function [Whi17].

More information about FEM and simulation tools can be found in the following documents [Alt20, Cas20, Het14, Kle00, PID17]

2.4.1 SIMULATION STEPS

Before jumping to the simulations, in this section, the steps to achieve a successful simulation will be defined. These steps are common to all software that performs these types of simulations and must be followed in the following order.

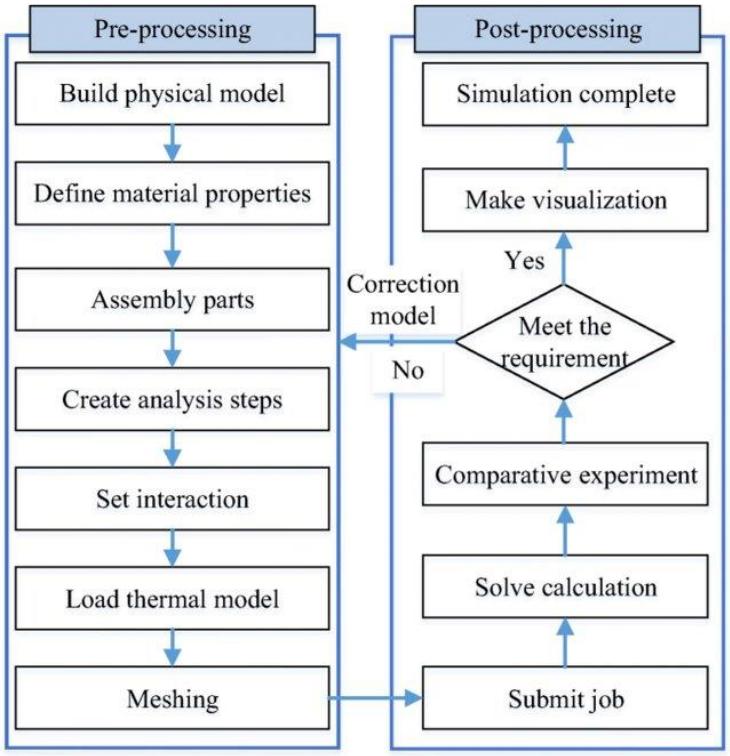


Figure 11: steps to perform a thermal-mechanical simulation [Son21]

An example of all the steps followed in ANSYS to perform a simulation is also available in Aschendorf's book "FEM bei elektrischen Antrieben 1" [Asc14].

First of all, a division into Pre-processing and Post-processing is carried out. The pre-processing stage is where all the preparation for the simulation is done, while in the post-processing step, the calculation of the simulation and the evaluation of the results is performed.

Inside the pre-processing stage, first a physical model needs to be designed, this means simplifying the model that is going to be simulated in order to reduce the computational resources needed to perform the simulation. Some of these modelling steps are filling unnecessary holes, cutting the geometry to only the area of interest or simplifying small details. A definition of modelling according to Giglmaier [Gig20] is: "simplification and/or neglection, complex or unknown mechanisms are replaced by simpler (and hopefully similar) ones".

When the physical model is decided, then a material needs to be assigned to that model with the necessary properties for the simulation such as young modulus, Poisson coefficient, maximum tensile strength, etc. Then all the parts are assembled into one big geometry file with all the contact and correlations such as contact patterns, force, moments, boundary conditions, etc.

As the geometry and definition of relations between the parts are defined, then the geometry needs to be divided into small regions where the equations will be analyzed in the solution step. The creation of divisions in geometry is called meshing. In chapter 2.4.3 Mesh generation, a more in-depth look into the different techniques for generating a mesh will be given.

Once the pre-processing steps are finished, the solving algorithm is applied in order to generate the simulation results and check if these results have a logical and physical meaning or if any kind of error has been committed during the simulation.

As can be seen in Figure 11 there are many steps needed in order to perform a simulation. A more in-depth view of the most important steps will be given in the following chapters.

2.4.2 GEOMETRY GENERATION AND ADAPTATION

In the geometry generation stage, the geometry is adapted so that it can be easier to mesh, an operation that will be explained in the next step. This means removing small details that need a lot of precision to mesh, like for example excessively small rounding, simplifying operations that are not relevant to the simulation, like removing holes or small openings for flat bulk surfaces or even deleting full components of the assembly that do not play a role in the simulation.

2.4.3 MESH GENERATION

The next step is meshing the geometry. This step is crucial because, without a good mesh, it is impossible to have good simulation results. As a general concept, what is achieved in the meshing stage is a discretization of the simulation geometry into a finite number of regions (called elements) each one with its evaluation points (called nodes). This is needed because the

approach in which these problems are solved is via approximation with a numerical solution instead of an analytical solution. This differentiation is needed because the problems that are solved with these techniques are too complex to have an exact solution and the solution is approximated by solving the equations at discrete points [Moa13]. Two main numerical methods can be used in order to perform this approximation of the solution: finite discretization and finite element, this last one is the one used by Ansys on the simulation of this thesis.

As Moaveni explained in his book "Finite element analysis" [Moa13], the finite difference method uses differential equations evaluated in each node of the mesh, while in the finite element method, the formulation uses integrals to create a system of algebraic equations.

Regarding the meshing parameters and characteristics, there are a lot of options that be adjusted in order to have the most optimized mesh for every simulation or application, this means, having the least number of cells without losing precision. The main types of meshes regarding their layout are structured or unstructured meshes.

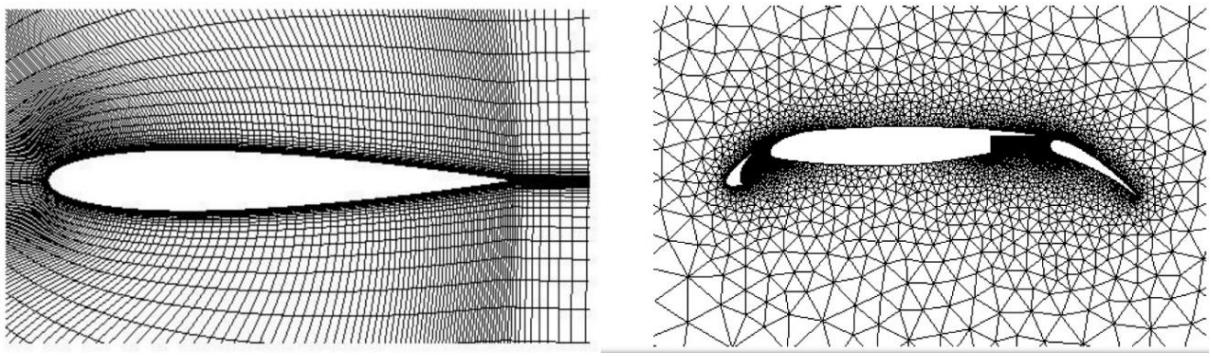


Figure 12: structure mesh (left side) and unstructured mesh (right side) [Gig20]

Each form has its pros and cons, and every simulation must be studied previously with care to select which strategy is more beneficial for that specific case. In the following table, the main differences between both approaches will be exposed.

Structure grids	Unstructured grids

Grid generation by hand (easier geometries)	Automated grid generation (complex geometries)
Simple and quick implementation	Difficult implementation but simple refinements
Mesh refinement complex	No global structure
Shorter computing times	Higher computing times
Similar elements with the same local connections	Any structure possible with different connections

Table 1: Characteristics of structure and unstructured meshes. [Gig20]

It must be also highlighted, that not every mesh is valid. The elements of the mesh must fulfil some specific quality requirements in order to generate trustworthy results. Some of those requirements are having no overlapping grids, always having a positive volume, being able to increase the density in a specific region of the mesh, having smooth size transitions and aiming for orthogonal neighboring cells, as Giglmaier states [Gig20].

In the case of having a structured mesh, these rules could be transformed into using three different types of meshing approaches which can be seen in the following picture.

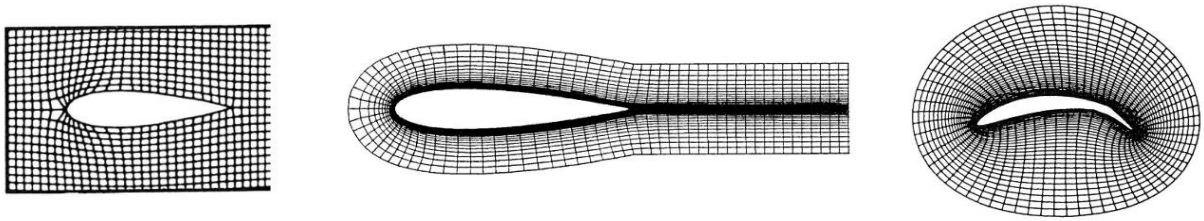


Figure 13: structure mesh layouts. H grid, C grid and O grid (from left to right) [Gig20]

2.4.4 SOLVER

As mentioned before, the next step is creating the mathematical model in the solver step. In this step, depending on the type of simulation (mechanical, thermal, aerodynamics, electromagnetism, etc.) multiple modelling approaches can be found for solving the same problem. The

task of the user in this case is to select the model that best describes the simulation for that case in order to have a more realistic approach to what the real behavior of your simulation will be.

Depending then on the model that is selected to represent reality, with the same geometry and mesh, different solutions can be extracted. This is another reason why this kind of simulation must be done always taking also into account a percentage of error that may be achieved and always comparing the results with a real experiment, to validate the results or the simulation setup used. For this validation stage, the next and last steps will be the most important ones.

2.4.5 POST-PROCESSING

The last step is what is called post-processing and is as important as the rest of the stages. In this step, the simulation is already finished, and the results of the simulation are evaluated to extract as much information as possible from that simulation. There is no point in doing a very good simulation when the post-processing stage has poor results evaluation.

In this stage, multiple plots, graphs, diagrams, and other means of representation are created in order to understand and validate the simulation results so that they can be compared with real-life experiment results or just evaluated to perform design improvements or extract the final results.

In terms of mechanical simulations as is the case with this thesis, the most important type of results and plots showing the total deformation, the stresses that the pieces suffer during the simulation, the temperature of surfaces if thermal equations are considered and also the contact related parameters to validate the contact behavior and check if the contact has been defined correctly.

3 HERTZIAN CONTACTS

In the third chapter of the thesis, before jumping into the simulation of the gears, it is necessary to do some previous preparation and study a similar contact that has a purely analytical solution as a reference for our simulation.

In this case, the Hertzian contact is a similar type of contact in comparison with the simulation that will be performed and thus it will be deeply analyzed and studied.

These contacts are a group of contact between different types of geometries that have been studied and evaluated so that every contact pair has a mathematical solution which result can be compared with the simulation results in order to determine the amount of error that the simulation introduces.

According to Taylor [Tay16], the creation of Hertz's contact dates from 1882, when Hertz investigated the contact between different elastic geometries. The study was carried out when investigating the contact between two elastic spheres. As Hertz stated in his book [Her96], the contact between these geometries should be a point, but that would lead in reality to infinite forces and stresses. Due to that, the geometries deform themselves slightly so that a tiny contact area is formed and solves this mathematical problem. The same happens to the contact between two cylinders, in this case, the theoretical contact region would be a line parallel to their axes, but in reality, it is also a small contact area created by the deformation of both bodies.

The Hertz contacts were studied under the following conditions and assumptions under Xiaoyin's paper: "Tutorial on Hertz Contact Stress" [Zhu12]:

- The type of contact is a non-adhesive elastic contact.
- The strains are small and within the elastic limit.
- Each body can be considered an elastic half-space, i.e., the area of contact is much smaller than the characteristic radius of the body.

- The surfaces are continuous and non-conforming.
- The bodies are in frictionless contact.

If these assumptions are fulfilled, then the following analytical results can be considered for calculating contact areas and contact stresses in the following contact pairs according to Xiaoyin [Zhu12]: sphere-plane contact, sphere-sphere contact, cylinder-cylinder contact, cylinder-plane contact, and rigid conical indenter-plane contact.

From all of these contact types, this thesis will focus on two, the contact between two cylinders (2D simulation) and the contact between two spheres (3D simulation).

3.1 CYLINDER-CYLINDER CONTACT

This first type of contact is going to be studied in a 2D simulation in order to reduce the computational time and make easier its evaluation.

Following "Contact Mechanics" by James Barber [Bar18], the mathematical approach, the maximum stress in this contact can be calculated based on the following equation depending only on the radius of the cylinders (R), the Young Modulus (E), the length of the cylinders (L), the application force of the contact (F) and the Poisson ratio of the material (v).

$$P_{max} = \frac{4 \cdot P_{mean}}{\pi} \tag{4}$$

P_{max}	MPa	Maximum pressure	P_{mean}	MPa	Mean pressure

$$P_{mean} = \frac{F}{2 \cdot L \cdot b} \tag{5}$$

P_{mean}	MPa	Mean pressure	F	N	Force
L	mm	Length	b	mm	Contact radius

$$b = 2\sqrt{\frac{F \cdot R \cdot (1-\nu^2)}{\pi \cdot L \cdot E}} \quad (6)$$

b	mm	Contact radius	F	N	Force
R	mm	Cylinder radius	ν	[-]	Poisson ratio
L	mm	Length	E	MPa	Young Modulus

If all these equations are merged, then the maximum stress of our contact can be calculated, and that is the value of interest for this comparison.

$$P_{max} = \frac{F}{\pi \cdot L\sqrt{\frac{F \cdot R \cdot (1-\nu^2)}{\pi \cdot L \cdot E}}} = \frac{752}{\pi \cdot 5 \cdot \sqrt{\frac{752 \cdot 6.47 \cdot (1-0.3^2)}{\pi \cdot 5 \cdot 200000}}} = 1275.4\ MPa \quad (7)$$

P_{max}	MPa	Maximum pressure	F	N	Contact force
L	mm	Length	R	mm	Radius
E	MPa	Young Modulus	ν	[-]	Poisson ratio

For the case of this study, substituting all of the values, the maximum stress that should appear between the cylinders is equal to 1275.4 MPa, as can be seen in Equation $P_{max} =$

$$\frac{F}{\pi \cdot L \sqrt{\frac{F \cdot R \cdot \left(1-\nu^2\right)}{\pi \cdot L \cdot E}}} = 752 \cdot \pi \cdot 5 \cdot \cdot 752 \cdot 6.47 \cdot \left(1-0.3^2\right) \cdot \pi \cdot$$

$5 \cdot 200000 = 1275.4\ MPa$ (7). Once this value has been calculated, a model for this geometry will be built in ANSYS and simulated with different meshes to analyze the error of the simulation and the mesh size dependence between the results of the simulation and the mathematical result calculated with the analytical solution.

3.1.1 GEOMETRY GENERATION

As has been remarked previously, this simulation will be analyzed as a 2D simulation to reduce the difficulty and the simulation times. This will allow us to have a much more precise mesh and deeply study the correlation between the mesh and the simulation results. This type of simulation is called “mesh sensitivity studies” and they are performed in order to evaluate the percentage errors that the simulation is approximately causing, concerning the mesh and other parameters.

The geometry simulated for this case is the contact between two semi-cylinders of a certain length and radius of 6.47 mm as can be seen in the following picture.

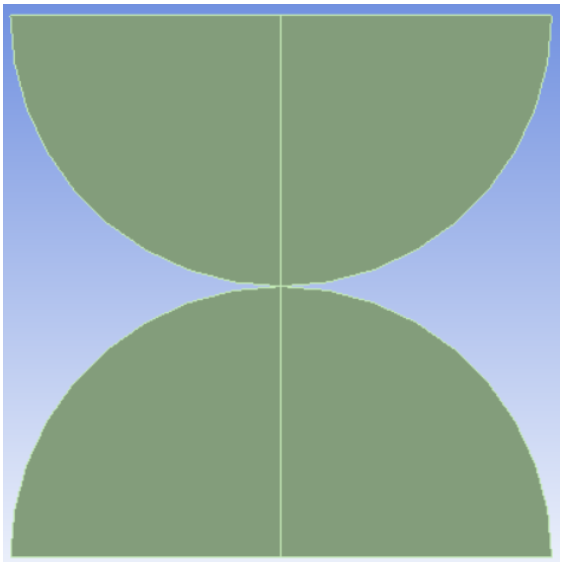


Figure 14: cylinder – cylinder geometry

Concerning the 2D behavior of the simulation, according to the ANSYS user guide, the following behaviors can be selected [ANS21]:

Plane Stress (default): Assumes zero stress and non-zero strain in the z-direction. Option for structures where the z dimension is smaller than the x and y dimensions. Examples of uses are flat plates subjected to in-plane loading, thin disks under pressure or centrifugal loading. A Thickness field is also available if you want to enter the thickness of the model.

Axisymmetric: Assumes that a 3D model and its loading can be generated by revolving a 2D section 360º about the y-axis. The y direction is axial, the x direction is radial, and the z direction is in the circumferential (hoop) direction. The hoop displacement is zero. Hoop strains and stresses are usually very significant. Example of uses is pressure vessels, straight pipes, and shafts.

Plane Strain: Assumes zero strain in the z-direction. Option for structures where the z dimension is much larger than the x and y dimensions. The stress in the z direction is non-zero. Examples of uses are long, constant, cross-sectional structures such as structural line bodies. Plane Strain behavior cannot be used in thermal analysis.

Generalized Plane Strain: Assumes a finite deformation domain length in the z direction, as opposed to the infinite value assumed for the standard Plane Strain option. Generalized Plane Strain provides more practical results for deformation problems where a z-direction dimension exists but is not considerable.

According to the requirements of the simulation, the plane stress behavior with a test length of 5mm will be selected for the simulation.

In terms of material, the selected material was structural steel as the aim of the simulation is to check the precision of the simulation and the standard materials inside the ANSYS materials

library are the ones with trusted and the most amount of information. In the following table, the most important material properties for the simulation can be seen.

Characteristic	Value	Units
Density	7850	$\frac{kg}{m^3}$
Young Modulus	$2 \cdot 10^{11}$	Pa
Poisson's ratio	0.3	Pa
Tensile Yield strength	$2.5 \cdot 10^{8}$	Pa
Compressive Yield strength	$2.5 \cdot 10^{8}$	Pa
Tensile Ultimate strength	$4.6 \cdot 10^{8}$	Pa

Table 2: Mechanical properties of structural steel

3.1.2 FIRST STRATEGY MESH GENERATION

For the creation of the mesh, a study of different strategies had been carried out to select the optimum distribution that allowed the computation of the results in a more efficient and faster way.

The first approach to the simulation was creating two refinement regions, where the element size is controlled to determine the optimum size for the simulation. Two zones were introduced so that the outer bigger region would act as a transition zone between the zone of interest, where the contact is taking place, and the rest of the geometry, where no stresses are present. By doing this, the volumetric growth of the mesh elements would stay around 1,5 so that the mesh quality stays acceptable.

Regarding both refinement areas, a structured mesh was established. This type of mesh needs more work to generate because ANSYS requires specific edge refinements that match the number of elements so that a structured mesh can be generated, but having this type of mesh allows the user to have more control over the mesh generation and the refinement regions.

To generate a structured mesh in the refinement region, the following refinement geometry was generated, so that the top and bottom edges match their number of elements as well as the right and left edges.

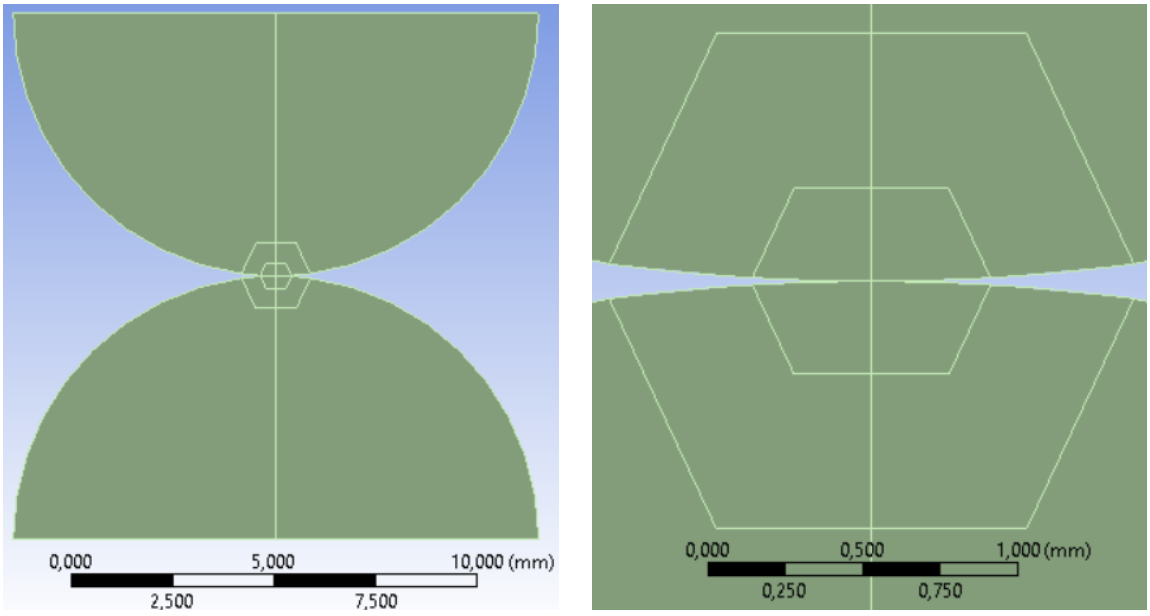


Figure 15: Mesh refinement region detail

Once this geometry has been set up and the refinement controls on the edges have been included, a meshing method has been established, so that the generation of a structured mesh is enforced.

Inside ANSYS, 3 different methods can be selected for 2D simulations or in other words, form meshing surfaces. These methods are Quadrilateral dominant, Triangles or Multizone Quad/Tri. The quadrilateral method is used for the structured meshes. With this method, the type of elements that are created is quads in 2D simulations and Hexahedrons in 3D simulations. If the triangles method is selected, an unstructured mesh is generated with triangle elements in 2D

simulations and tetrahedron elements in 3D simulations. If the geometry is very complex and different methods are required for the generation of the mesh, the multizone method is selected. As the desired mesh is a structured mesh, the quadrilateral method has been selected in this case.

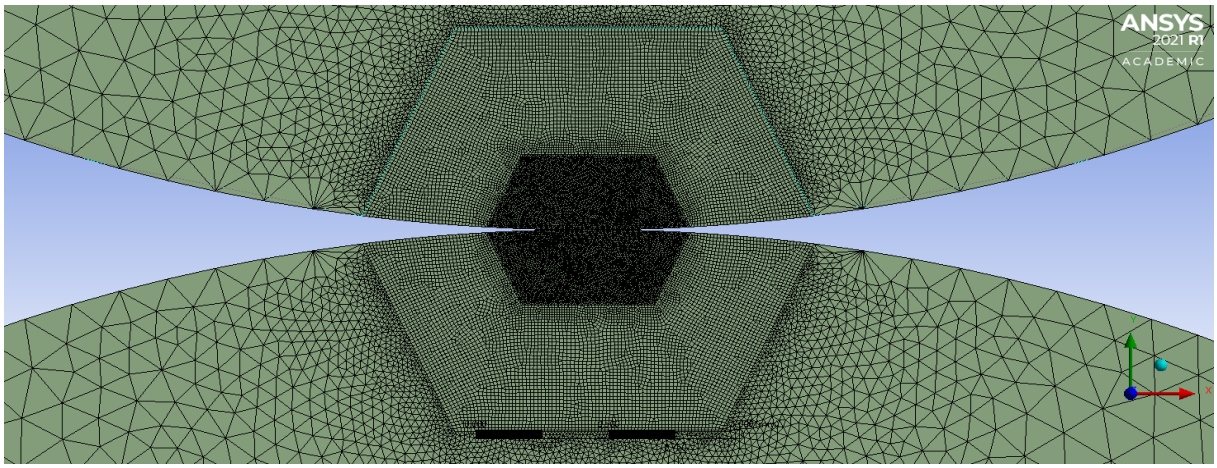


Figure 16: meshing example of one of the simulations

As can be seen in Figure 16, the inner refinement region has a structured mesh, while the outer region that is not relevant to this simulation is an unstructured mesh.

3.1.3 MESH QUALITY EVALUATION

Regarding mesh evaluation, multiple parameters can be used to evaluate the quality of the mesh. Some of those methods are element quality, aspect ratio, Jacobian ratio, warping factor, parallel deviation, maximum corner angle, skewness, orthogonal quality, and characteristic length. From all of these parameters, a selection of 4 has been made to evaluate the quality of the mesh.

3.1.3.1 Element quality

According to the ANSYS User's Manual, *"The Element Quality option provides a composite quality metric that ranges between 0 and 1. This metric is based on the ratio of the volume to*

the sum of the square of the edge lengths for 2D quad/tri elements, or the square root of the cube of the sum of the square of the edge lengths for 3D elements. A value of 1 indicates a perfect cube or square while a value of 0 indicates that the element has a zero or negative volume." [ANS21]

$$Element\ quality = C \cdot \left(\frac{area}{\sum(edge\ length)^2}\right) \quad (8)$$

In the following table, the values of the constant C depending on the element geometry can be checked.

Element	Value of C
Triangle	6.92820323
Quadrangle	4.0
Tetrahedron	124.70765802
Hexagon	41.56921938
Wedge	62.35382905
Pyramid	96

Table 3: C constant value for element quality

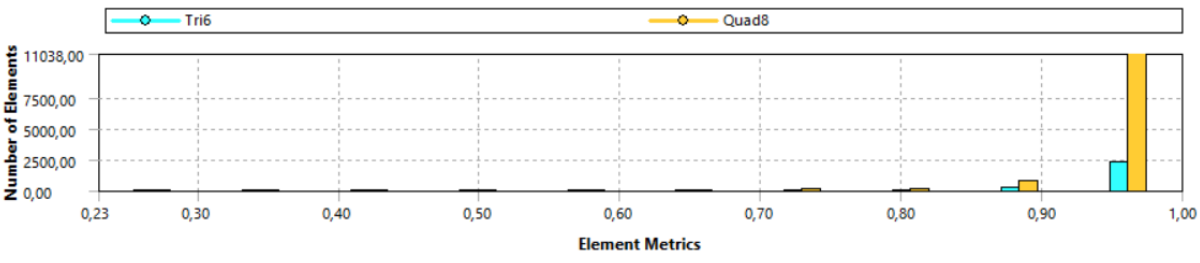


Figure 17: element quality values

As can be seen, most of the elements are close to 1, meaning that they have very good element quality. The minimum quality is around 0.23 but if the elements with a quality below 0.8 are plotted, as it can be seen in the following image, they are very few elements and all of them are outside of the area of interest, so they will not have an impact on the results on the area of interest.

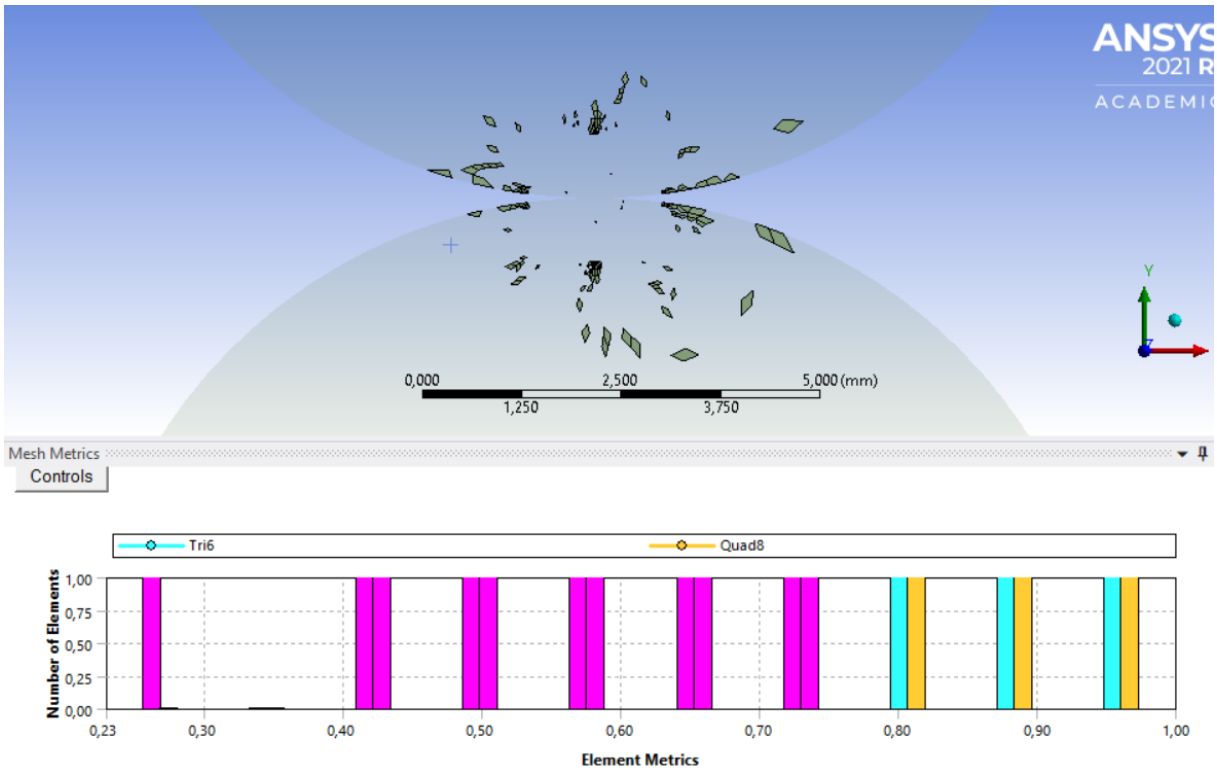


Figure 18: the display of elements with lower element quality than 0.8

3.1.3.2 Aspect ratio

For the calculation of the aspect ratio, the following steps need to be followed according to the ANSYS User Manual [ANS21]

If the element is not flat, the nodes are projected onto a plane passing through the average of the corner locations and perpendicular to the average of the corner normal. The remaining steps are performed on these projected locations.

Two lines are constructed that bisect the opposing pairs of element edges and which meet at the element center. In general, these lines are not perpendicular to each other or any of the element edges.

Rectangles are constructed centered about each of the 2 lines, with edges passing through the element edge midpoints. The aspect ratio of the quadrilateral is the ratio of a longer side to a shorter side of whichever rectangle is most stretched.

The best possible quadrilateral aspect ratio, for a square, is one.

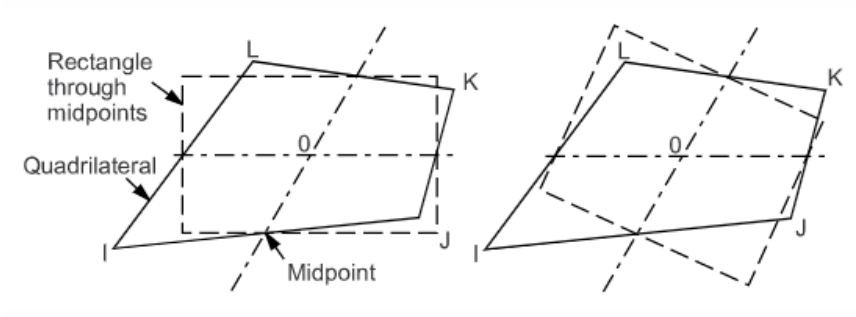


Figure 19: aspect ratio calculation [ANS21]

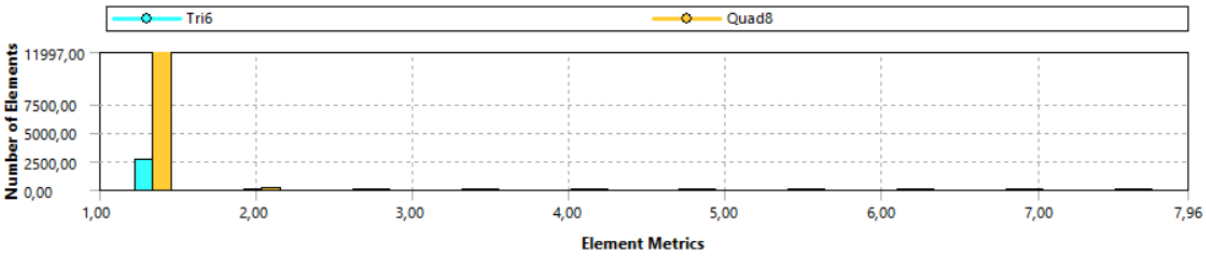


Figure 20: aspect ratio values

As can be seen, the aspect ratio values are close to 1 with a maximum value of 7.96, being the elements with a higher aspect ratio than 2 outside of the area of interest.

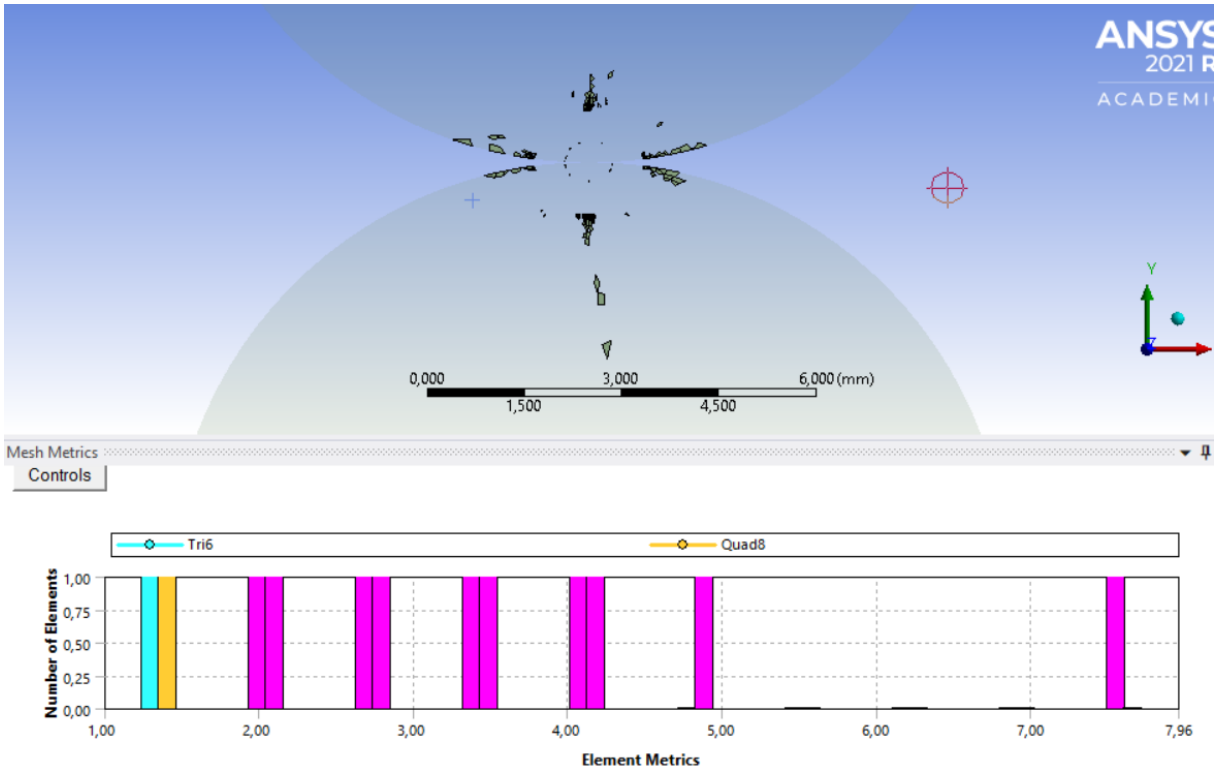


Figure 21: elements with a higher aspect ratio than 2

3.1.3.3 Skewness

Skewness is one of the most common methods to evaluate a cell's quality and determines how close an element is to its perfect equilateral or equiangular shape. There are two main equations to calculate this factor: triangle shape elements and quadrilateral elements. This last one is the one of interest for this mesh as it has a structured architecture and is mainly formed of quadrilaterals.

$$\max\left[\frac{\theta_{max}-\theta_e}{180-\theta_e}, \frac{\theta_e-\theta_{min}}{\theta_e}\right] \quad (9)$$

θ_{max}	º	Largest angle in the face or cell	θ_{min}	º	smallest angle in the face or cell
θ_e	º	angle for an equiangular face/cell (90 for a square)			

The output of this equation is a value between 0 and 1, where 0 indicates a perfect equilateral/equiangular shape and 1 is a degenerated shape. Based on experience, a mesh can be considered good if the skewness level is under 0.8 or 0.9-0.95 in really complex geometries.

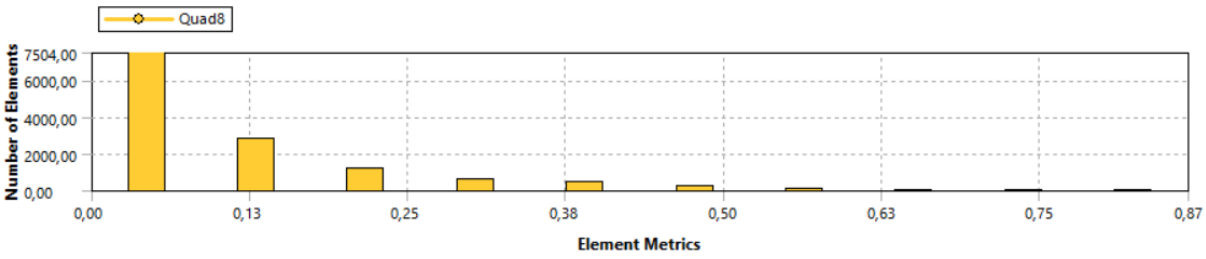


Figure 22: skewness values

As it can be analyzed, the maximum skewness level is under 0.87 and most of the elements have a really low skewness value, meaning that the mesh has good-quality elements.

3.1.3.4 Orthogonal quality

This value is always between 0 and 1 and evaluates not only the quality of the shape of the cell, but also its relation to the neighboring cells. As it is stated on the user manual "The orthogonal quality for cells is computed using the face normal vector, $\overrightarrow{A_i}$ for each face; the vector from the cell centroid to the centroid of each of the adjacent cells, $\overrightarrow{c_i}$; and the vector from the cell centroid to each of the faces, $\overrightarrow{f_i}$. For each face, the cosines of the angle between $\overrightarrow{A_i}$ and $\overrightarrow{c_i}$, and between $\overrightarrow{A_i}$ and $\overrightarrow{f_i}$, are calculated. The smallest calculated cosine value is the orthogonality of the cell." [ANS21]

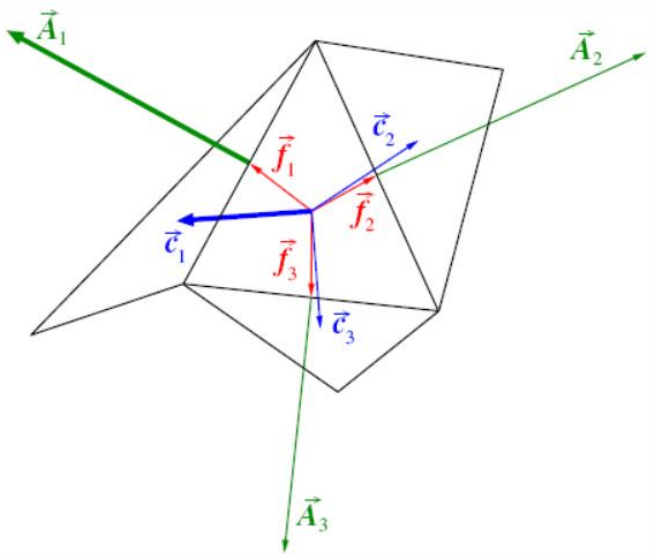


Figure 23: Vectors Used to Compute Orthogonal Quality for a Cell [ANS21]

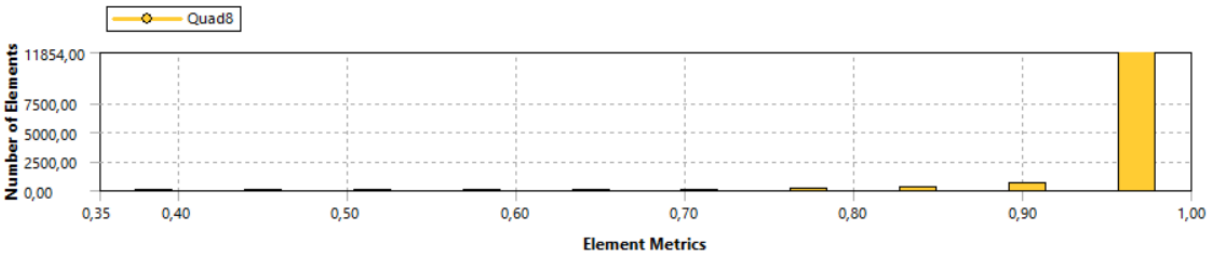


Figure 24: Orthogonal Quality values

Most of the elements have an orthogonal quality over 0.9, which is considered a really good quality with a minimum of 0.35, that can be handled by the solver without generating big problems.

3.1.4 CONTACT DEFINITION

Once the mesh has been generated the next step is to set up the solver of ANSYS to simulate the case of the study. In this occasion, the setup of the solver includes the contact definition and the boundary conditions with the force applications.

Regarding contact definition, in this simulation, there is only one active contact, and it is between the faces of both semicircles. To make the contact computation faster, only the regions where the refinement is done are where the contact is active as can be seen in the next image.

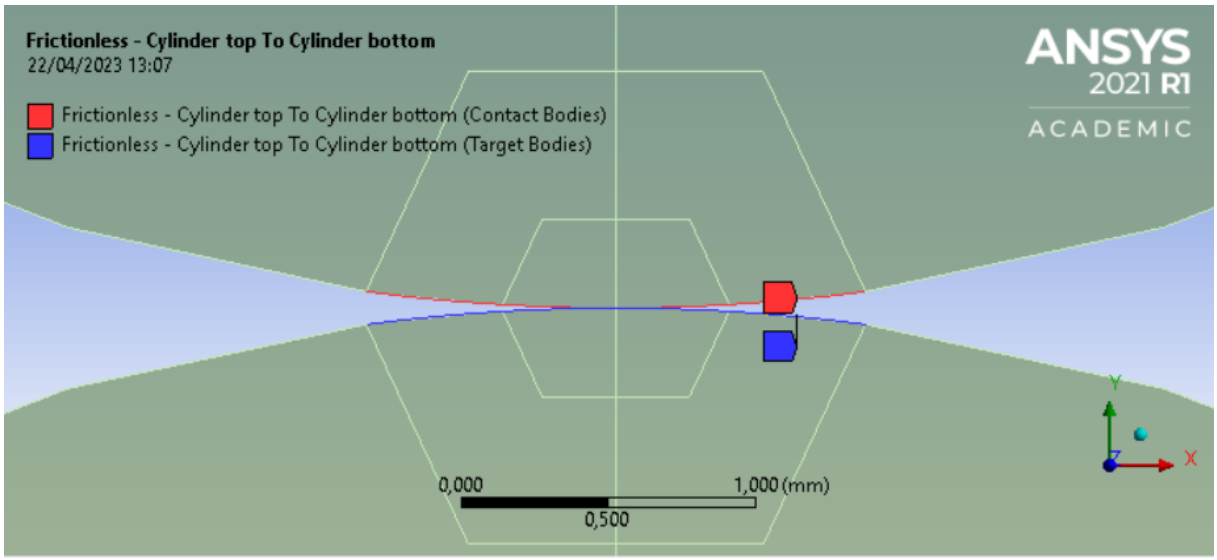


Figure 25: Display of contact regions

The type of contact is frictionless, as that is one of the conditions of the Hertzian contacts lastly, ANSYS allows to include of a geometry modification to ensure that both geometries are in contact at the beginning of the simulation, and that is achieved with the interface

treatment "Adjust to Touch" that was selected for this contact definition. What this option does is slightly modify the nodes of the contact region so that they are in touch at time = 0s of the simulation. This is only a computational change, so the contact starts smoother without pressure peaks but does not change the simulation geometry, so a physical gap could be seen in the post-processing if both geometries are not perfectly adjusted in the CAD phase.

Contact Side	Type	Status	Penetration (mm)	Gap (mm)	Resulting Pinball (mm)
Contact	Frictionless	Closed	0	6.9839^{-23}	4.575^{-2}
Target	Frictionless	Inactive	N/A	N/A	N/A

Table 4: Contact tool data

If the contact tool is run for a pre-analysis of the contact, it can be checked that the contact has a closed status, this means that both geometries are close enough to consider a contact, and the geometric penetration is 0. This last check of the geometric penetration is done to make sure that the adjust-to-touch function has worked correctly and does not overlap both geometries causing a false calculation of the contact.

3.1.5 BOUNDARY CONDITIONS

For the desired simulation, the following boundary conditions have been established. As fixed support, the bottom face of the bottom semicylinder has been fixed. In addition, the symmetry plane on the top semicylinder has been forced a displacement only in the Y direction to avoid possible tipping of the top cylinder. Lastly, the load has been applied on the top surface of the top semicylinder.

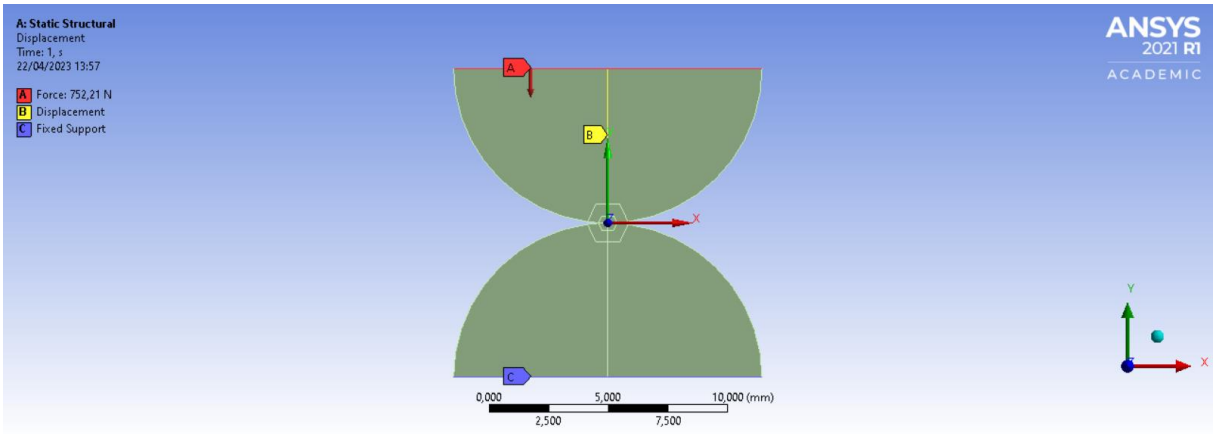


Figure 26: boundary conditions for the simulation

3.1.6 ELEMENT ORDER EVALUATION

The first sensitivity analysis that was carried out with this mesh study was the effect of the mesh element order. In ANSYS there are two types of elements, a linear simpler element order, or a more complex quadratic order and the difference is located in the number of nodes per element or edge.

In the linear element order, a node is located on every vertex of an element, this means that the variation of a value through an edge can only have a linear form, as it has only two reference values, one on each vertex. On the other side, the quadratic element order generates an extra node in the middle of the edge, so that a third value is calculated allowing to have quadratic value changes through an edge. This additional node does not need to be exactly at the middle of the edge, it can be moved slightly to the sides so that it improves the mesh quality in areas where complex geometry is located.

The quadratic order has higher precision due to the additional computational point located at the middle of the two vertexes, but this also increases the calculation time of the mesh and the computational time for getting a solution, so if it is more important time than precision, a linear element method could be the best choice.

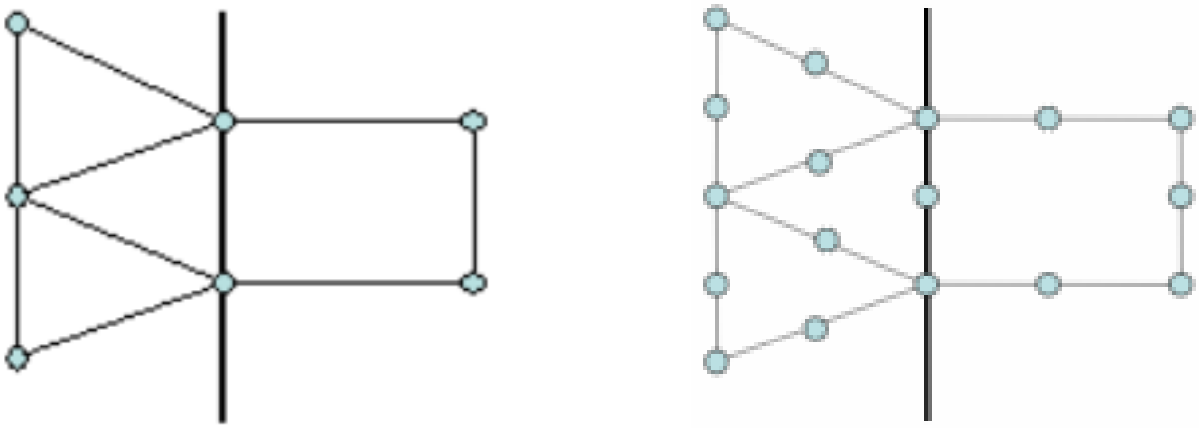


Figure 27: linear element order (left) and quadratic element order (right) [ANS21]

Based on these differences, a study has been carried out in which the same meshes have been tested with both linear and quadratic orders, where the results and time requirements have been monitored. Regarding the results, the reference value that was monitored was the maximum stress, and according to the analytical solution seen in Equation 7.

Based on this result, the percentage of error was calculated for multiple meshes that go from a refinement of 0.1 mm element size to 0.01 mm to evaluate the difference in precision and in-time requirements.

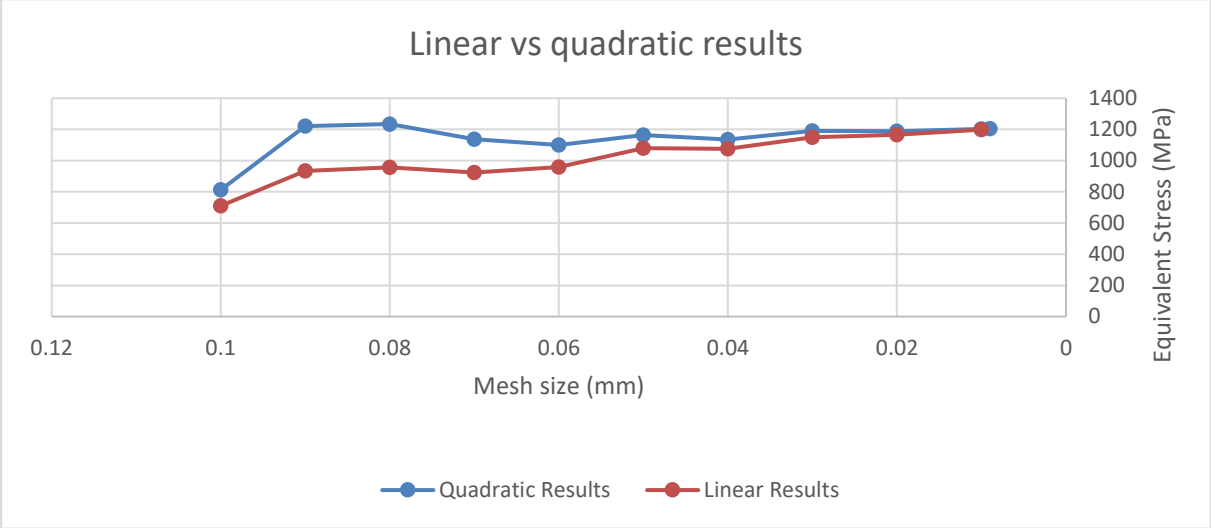


Figure 28: quadratic vs linear results for cylinder–cylinder simulation

Based on this preliminary study, it can be seen that there is an important impact on the element order, being the quadratic order is much more accurate than the linear order. Although the linear order is less accurate in all the simulations that have been tested, from this graph it can also be derived, that if the mesh is small enough to capture all the details of the contract, the loss of precision of the linear order could be almost neglected. In the following graph, the percentage of error generated in every simulation can be seen.

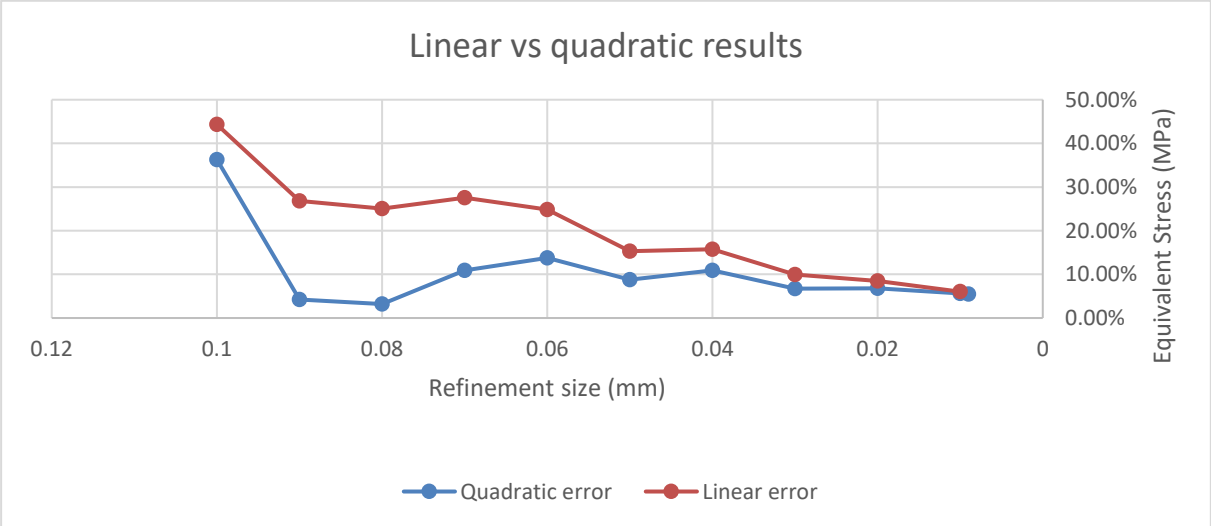


Figure 29: percentage error of every simulation

Considering the dimensions of the final gear geometry, a mesh with small elements around 0.01 mm will not be able to be generated and due to this limitation, the quadratic order will be selected from this point forward.

One last evaluation was carried out comparing the linear and the quadratic order and this is related to the time requirements to complete the simulation.

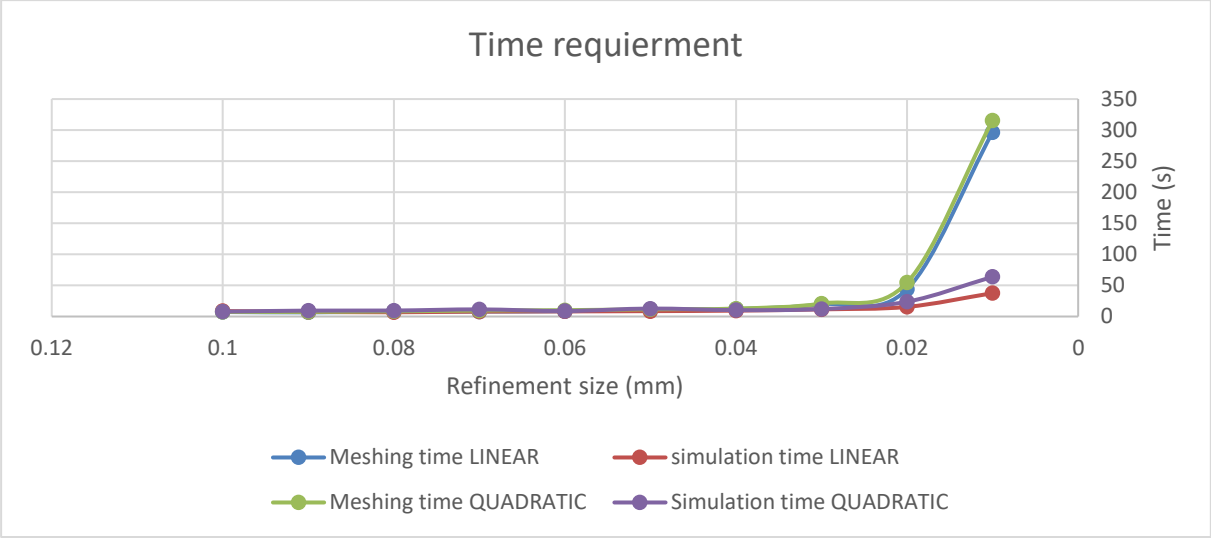


Figure 30: time requirements for quadratic and linear order simulations

As can be seen, the difference in computational time and meshing time of both methods are very similar. Both methods increase the time considerably for a refinement size below 0.02 mm, so the quadratic method can be confirmed as the best element order for this specific simulation.

3.1.7 RESULT EVALUATION OF FIRST REFINEMENT GEOMETRY

Once the mesh quality has been checked and the quadratic element order has been selected as the default order for this simulation, the first mesh sensitivity analysis was carried out. In this case, the mesh refinement region was the one shown in Figure 16. In the

sensitivity analysis, the mesh refinement size has varied from 1 mm to 0.002 mm, having the outer refinement region double the size of the inner region.

With this analysis, once again the maximum stress was monitored as a reference value, as well as the simulation time, the percentage error, and the number of elements of the mesh. In the following graph, on the left side the maximums stress in MPa is located on the right side the percentage error and on the X axis the refinement size is in mm.

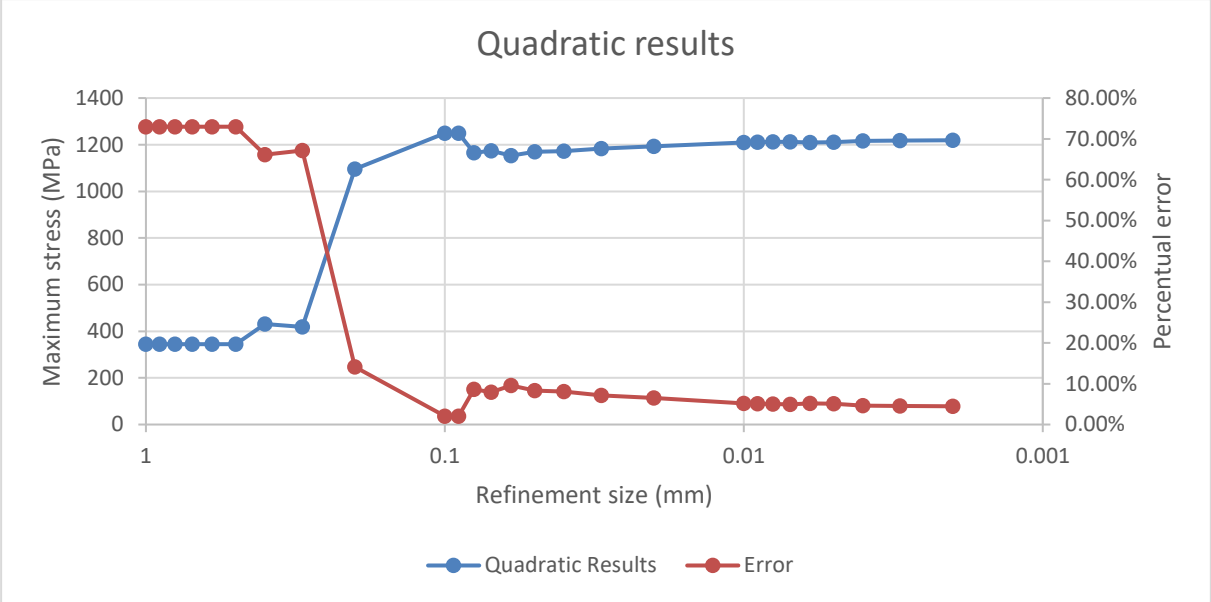


Figure 31: Simulation results of refinement geometry 1

As can be seen, all the results below 0.1 mm have an error of less than 8%, achieving a minimum error of 4.5%. This makes a clear threshold at 0.1 mm where the results can start being considered acceptable.

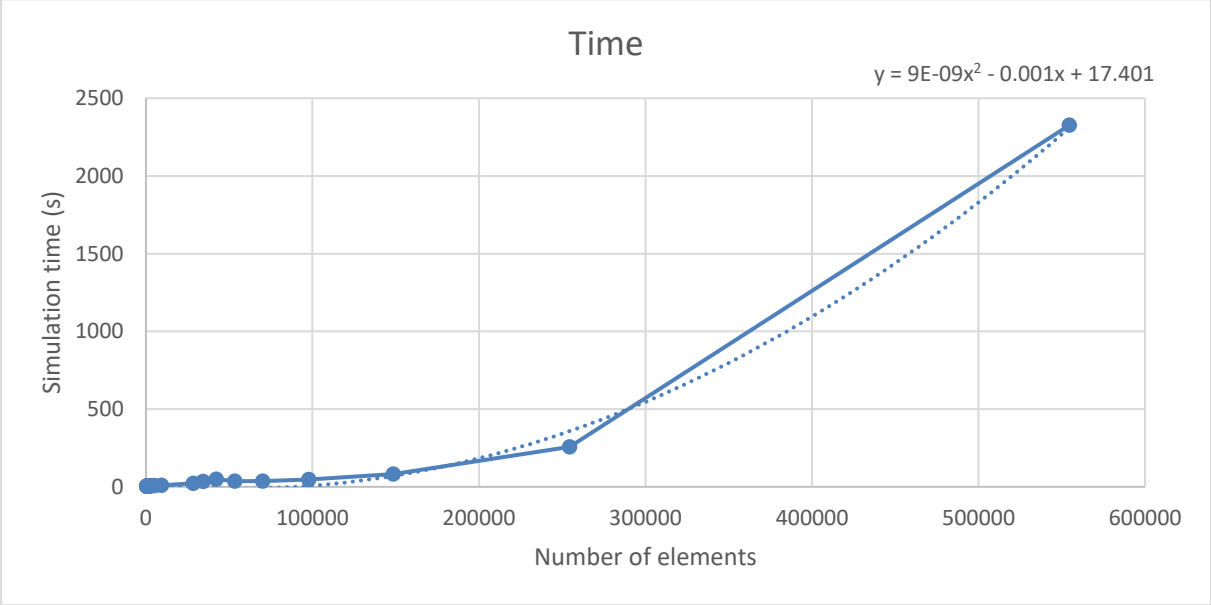


Figure 32: meshing results of refinement geometry 1

In this second graph, seen in Figure 32, the meshing parameters have been evaluated. This time on the X axis, the number of elements of the mesh is present, while on the Y axis, the simulation time can be seen. The simulation time has a clear steep increase in simulations with element numbers above 200.000, having more or less a quadratic correlation as can be seen in the top right corner of the graph. This means that refinements under 0.003 mm are not worth it, due to the increase in simulation time without a decrease in the percentage error, it stays around 5%. For a more visual approach, in the following picture, the different stress patterns can be seen for 4 different simulations with different refinement sizes.

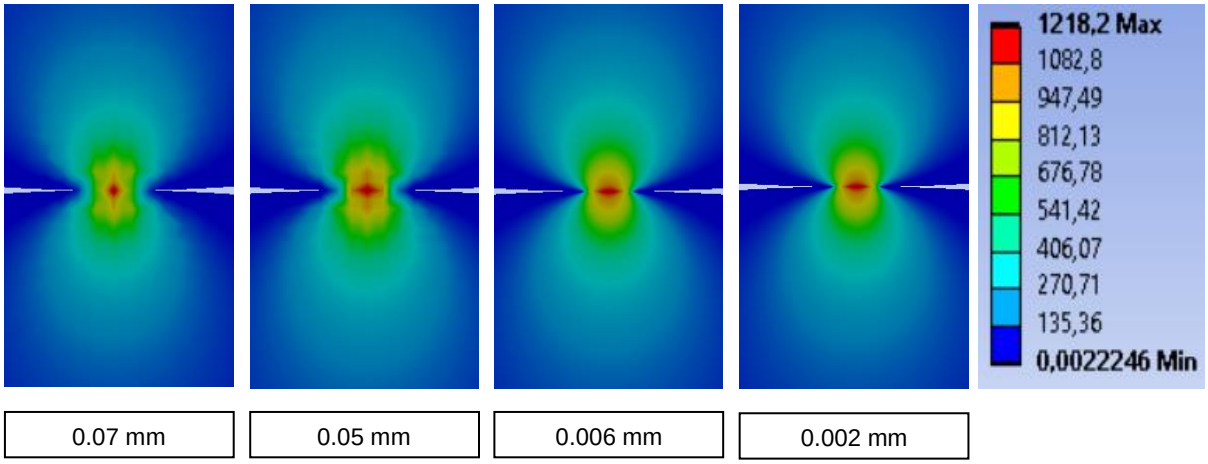


Figure 33: contact patterns with different mesh refinements (stress shown in MPa)

As it is shown in the pictures in Figure 33, the two simulations on the left side show a distorted stress pattern, although the maximum stress compared with the analytical result deviates only by approximately 8%. On the contrary, on the two simulations on the right side, the contact pattern is almost identical, while having a completely different simulation time, needing the simulation with a 0.006 mm refinement only 36 seconds to simulate and the simulation with a 0.002 mm refinement, 2327 seconds. As it has been proved previously in Figure 30, this type of simulation is relatively easy, the most impact is located on the meshing time and not so much on the simulation time. That is why such a big difference in simulation time means a bigger difference in meshing time.

3.1.8 CONCLUSIONS

Evaluating the results of this mesh sensitivity analysis, two main conclusions can be extracted. First, it can be seen that every simulation has an error in comparison with the analytical result that must be considered when using future results as design inputs or requirements. In this occasion, a minimum error of 4.45% was achieved, although considering computational requirements and time, the optimum refinement is located at 0.01 mm, where the error is just above 5% and the total simulation time. Another conclusion that can be drawn is that it is always required to have more than one validation or analysis

variable. If in this analysis all the decisions were based only on the maximum stress, a false conclusion of using a refinement of 0.07 mm would be taken, but as seen in Figure 33, with this refinement, the stress pattern is not the correct one although the maximum pressure is similar to the analytical result. In Figure 34 and Table 5, a summary of the optimum simulation is presented with its results.

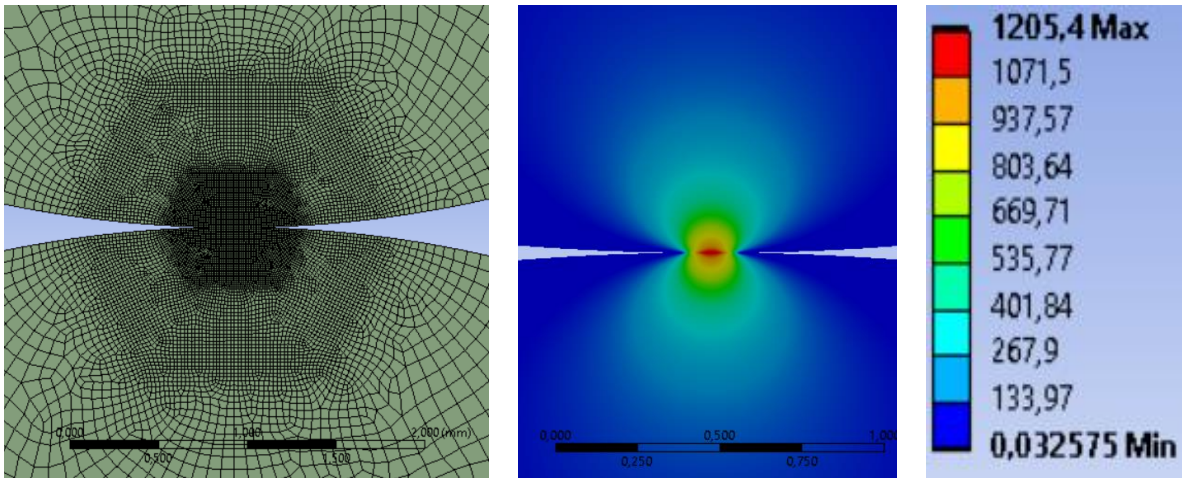


Figure 34: final results of sensitivity analysis with geometry 1 (Stress shown in MPa)

Variable	Value	Unit
Refinement	0.01	mm
Meshing time	11.7	Sec
Simulation time	46.5	Sec
Maximum stress	1205.4	MPa
Percentage error	5.48 %	-

Table 5: result summary table

3.1.9 SECOND MESH GENERATION AND BOUNDARY CONDITIONS

The second refinement geometry that was tested has a first refinement region on the contact area like geometry 1, but instead of having a second bigger refinement region, it has a rectangular geometry above the contact area to capture the radial stresses and have an easier structure mesh generation. With this new geometry, the mesh element number is lower, for the same refinement, making possible faster simulations with the same precision, as the second refinement region of geometry 1 was located too far from the contact region, making almost no impact on the results. Regarding the boundary conditions, the displacement condition only in the Y direction that was applied to the symmetry axis on the first geometry in this occasion was enforced to the whole face except the refinement region, as seen in the following image.

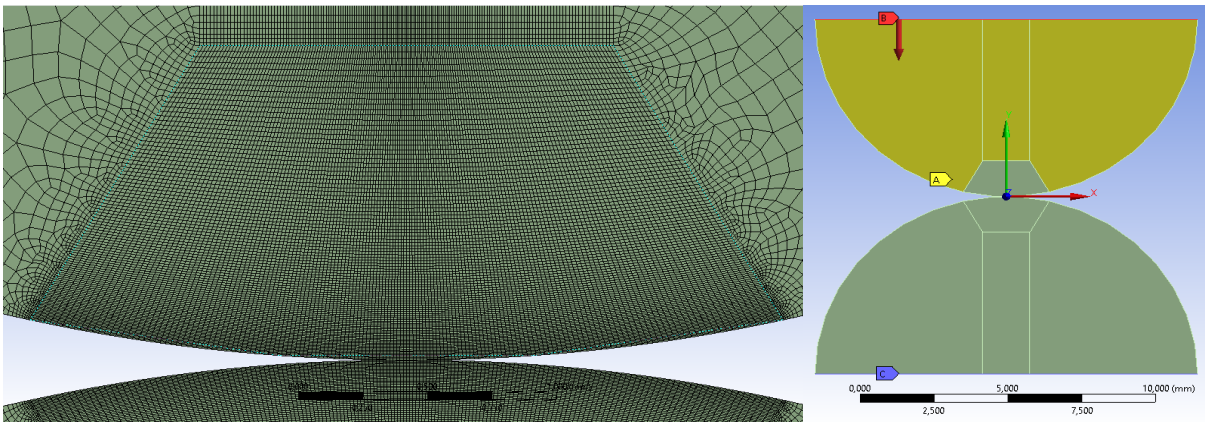


Figure 35: refinement geometry 2 and boundary conditions

After evaluating the results of this simulation, it was found out that this refinement geometry was not the ideal one, because it is true that the number of elements in the contact region is smaller when not having the second refinement area, but due to the large rectangle geometry, when the refinement reaches small sizes, the growth of the number of elements of the mesh is much bigger than in the mesh 1, making impossible very small refinement sizes like the 0.002 mm achieved in the mesh 1.

The boundary conditions also seem to be not the correct ones, because although the simulation is faster, the downward movement of the cylinders generates deformations in all directions, not only in the Y direction, so these boundary conditions do not represent the reality of the contact. This can be seen in the percentage error if it is compared to the first simulation.

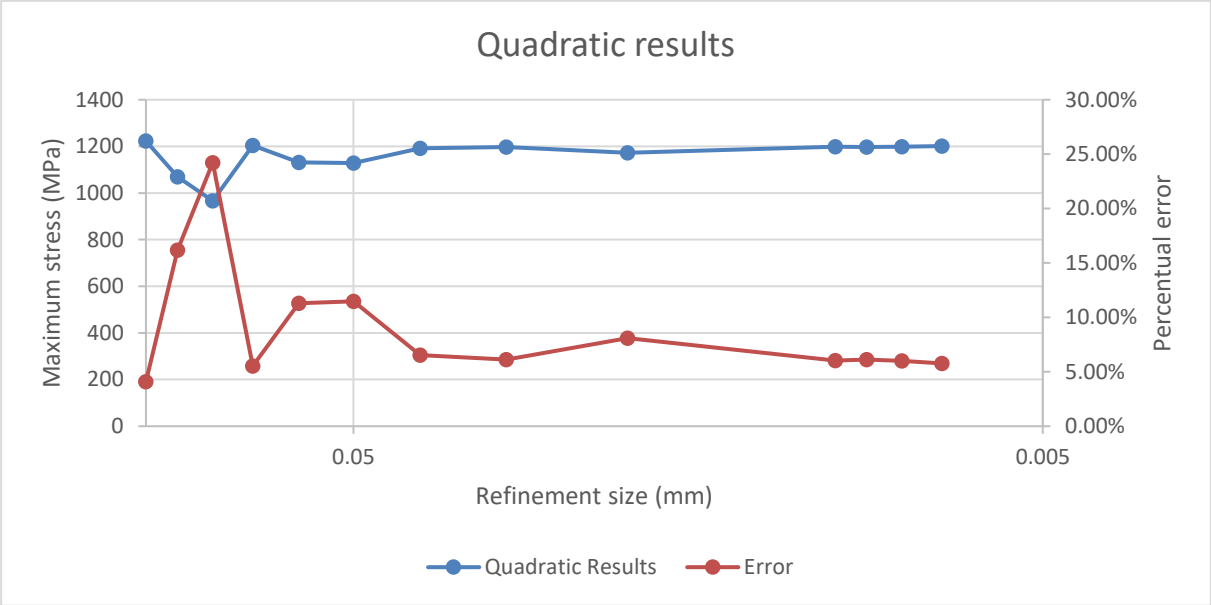


Figure 36: Simulation results of Geometry 2

In this case, if we take as reference for example the simulation with a refinement of 0.01 mm, the error with set up 2 is 6% when in geometry 1 it was approximately 5%. Also, regarding the simulation times, in comparison with the first refinement geometry, this new refinement is much slower. One last interesting thing that can be remarked, is that once more, taking into consideration simulation results and simulation time, the optimum refinement size is 0.01 mm, the same results as the first geometry, confirming once again a possible reference refinement size for this simulation.

3.1.10 THIRD MESH GENERATION AND BOUNDARY CONDITIONS

Having seen both previous simulations, a last refinement strategy was followed whose aim was to make the refinement as uniform as possible, so instead of making a trapezoidal refinement, in this case, the simulation was done with a spherical refinement region as shown in the following figure. This will allow capturing better the stress pattern, as the results shown in the first simulation showed a spherical stress pattern.

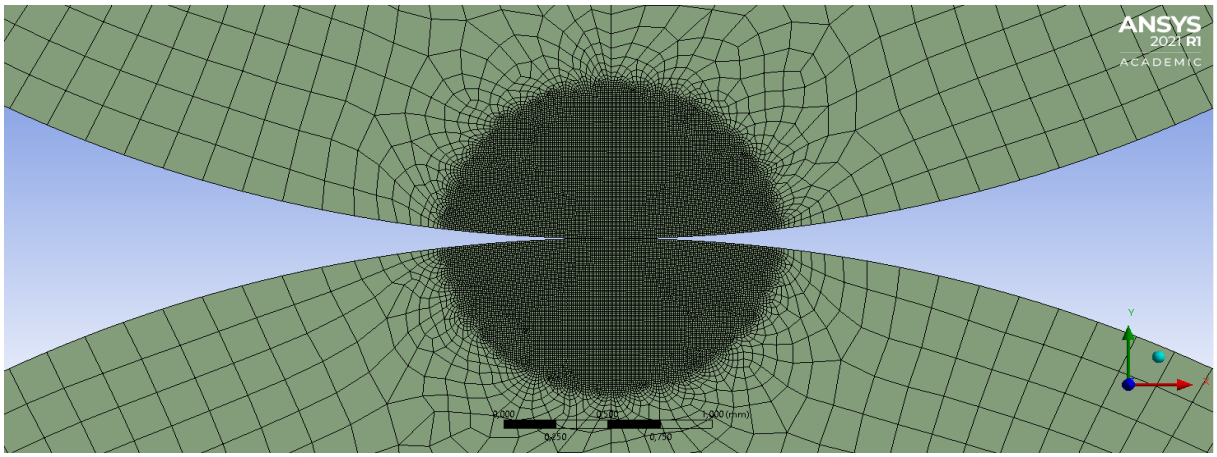


Figure 37: refinement mesh 3

In order to determine the optimum radius for the refinement, a small study has been carried out. In this study, multiple tests have been made to see what the optimum radius is, to capture the whole stress pattern of the contact.

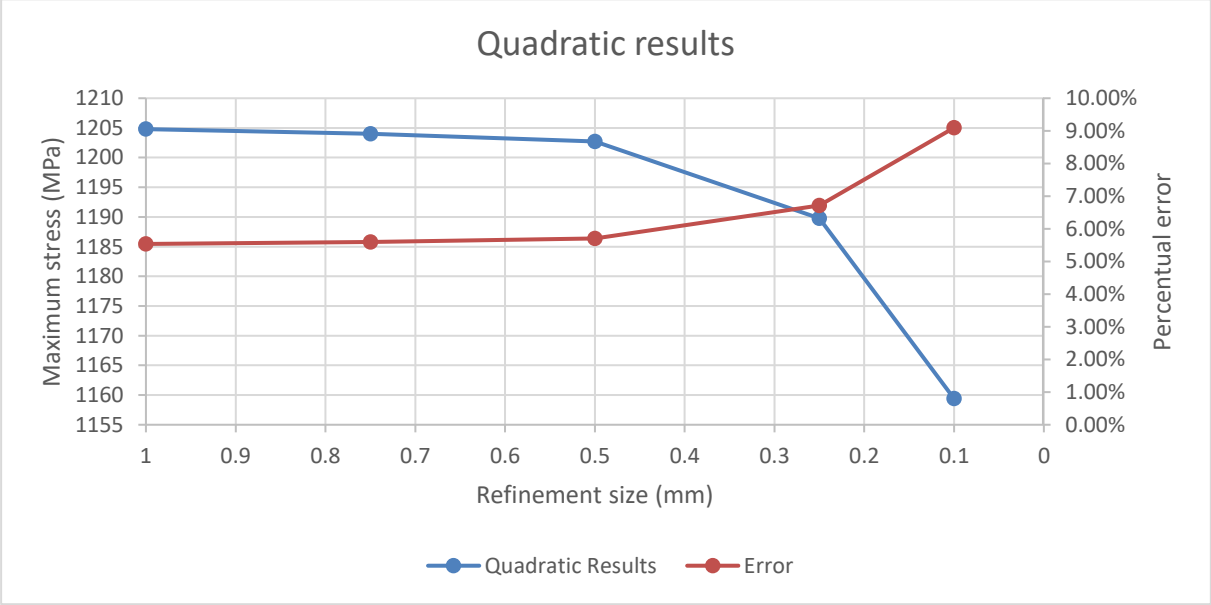


Figure 38: geometry study for optimum radius

As it is shown, the radius of the refinement area is located on the X axis, and which optimum is around 0.5 mm, as a smaller radius does not capture some details of the contract, and a bigger radius gives the same solution and adds no extra information or precision. In the following images, a comparison of the results with three different radii can be seen.

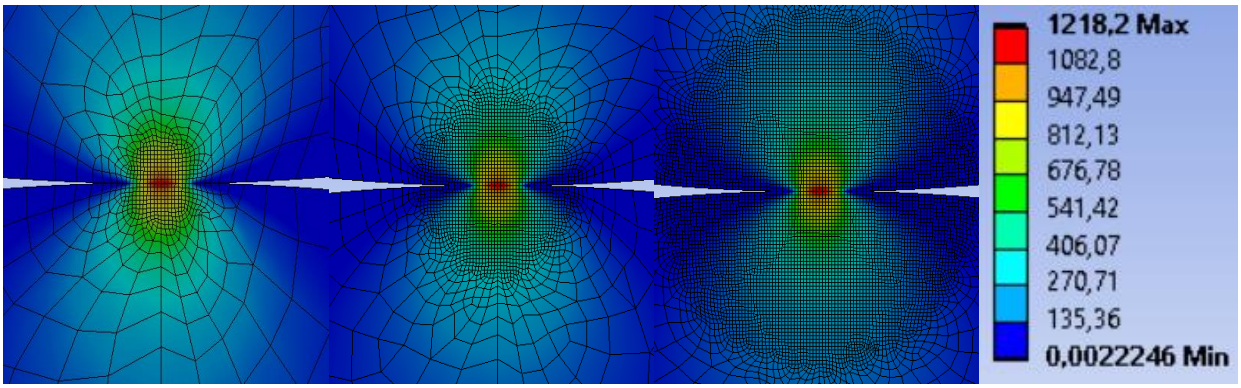


Figure 39: refinement radii analysis (Stress shown in MPa)

Once this radius has been defined, the following mesh sensitivity analysis has been carried out to verify one last time the influence of the mesh and estimate the error that the simulation will give in future simulations.

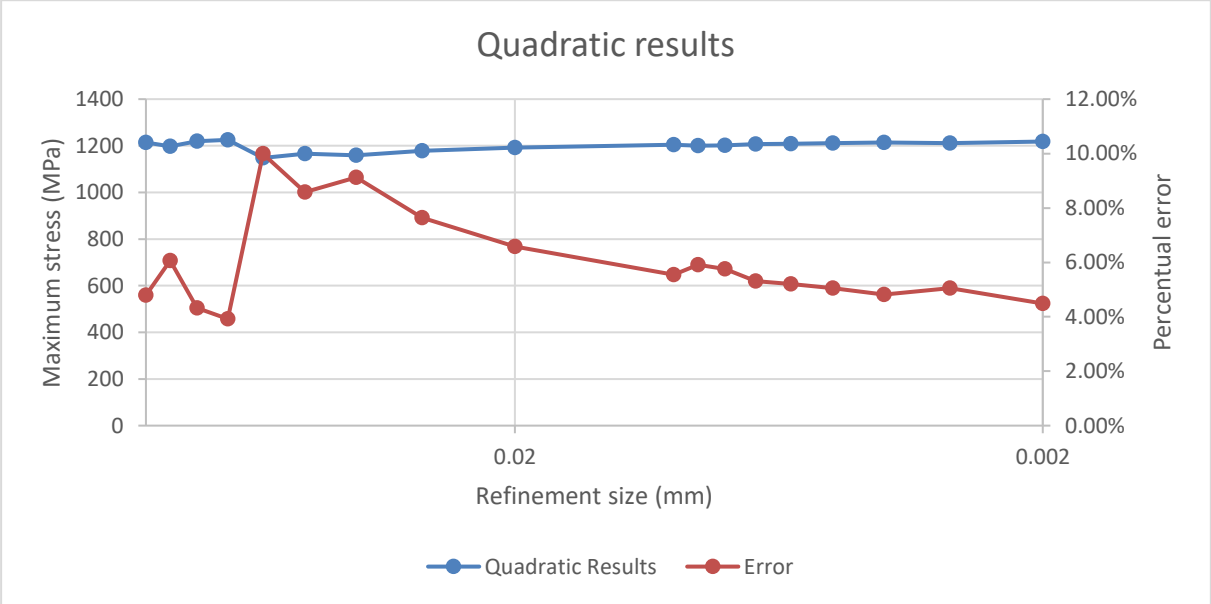


Figure 40: results of simulation geometry 3

As can be seen, the results keep getting closer to the analytical result from a 0.06 mm refinement onwards, achieving a minimum error at 5% like the previous tests done with the other geometries. The reference refinement taken from the previous tests, 0.01 mm, shows also here a good compromise, as is the first simulation with an error below 6%. Regarding the first 4 simulations, which have results with errors even below 4%, they cannot be taken into consideration, as it has been proved, that this is just checking with the maximum stress, but in reality, the simulation does not represent the real stress pattern that the test cylinder would suffer in the reality under that load.

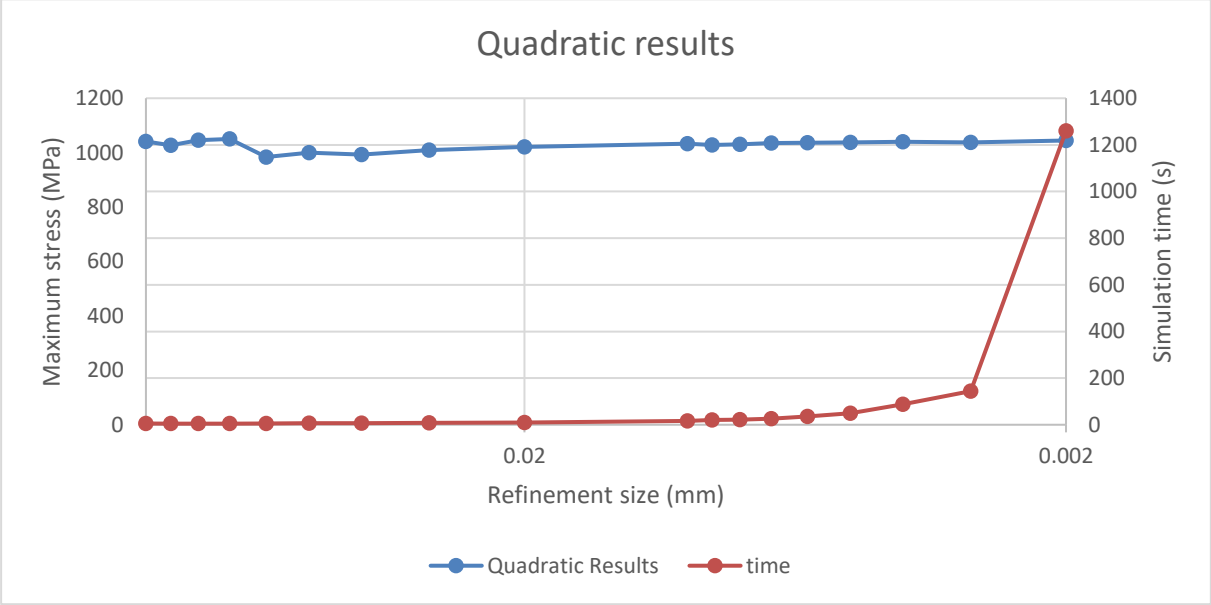


Figure 41: results simulation geometry 3

From this last graph, again it can be seen how the simulation time (not considering meshing time) increases drastically with the last simulations with refinements of 0.002 mm, making once again a reasonable refinement size of 0.01 mm.

As not all the geometries and simulations have the same dimensions and orders of magnitude, for future simulations, instead of taking the absolute value of the refinement, a relative value will be considered, making this sensitivity analysis valuable for a wider range of simulations.

In this case, as a reference length, the radius of the semicylinder was taken, which is 6.47 mm. This means that the optimum refinement, in this case, is achieved when the refinement size is approximately 0.16% of the reference length that was considered. This is always taken as a reference value and can be modified slightly to fulfil other demands or requirements in case the mesh or the simulation will not allow these refinements.

3.1.11 VALIDATION OF THE RESULTS

With this study, the maximum stress of the contact has been contrasted with the analytical result from the Hertz theory, but as it has been proven, this is not enough to affirm that the simulation has valid results. One last check must be done, and it is to compare the complete stress pattern with other simulations of the same type. As can be seen in Figure 39, on the contact region, the maximum is located right at the contact zone on the surface, while when moving inwards, the stress decreases in a spherical distribution with the center at the contact point. If these results are compared with the ones obtained by Sugunesh in his article, it can be seen how both layouts look very similar, confirming that the simulation is performed correctly, and the results have a valid use.

The reason why the maximum stress is located right at the contact region is due to the contact layout of the cylinder contacts. In this case, the contact region is a line, generating a concentration of force along the contact line generating high stresses due to the small contact area. Due to this phenomenon, the maximum stress is always located in the contact point in a 2D simulation and along the contact line in a 3D simulation.

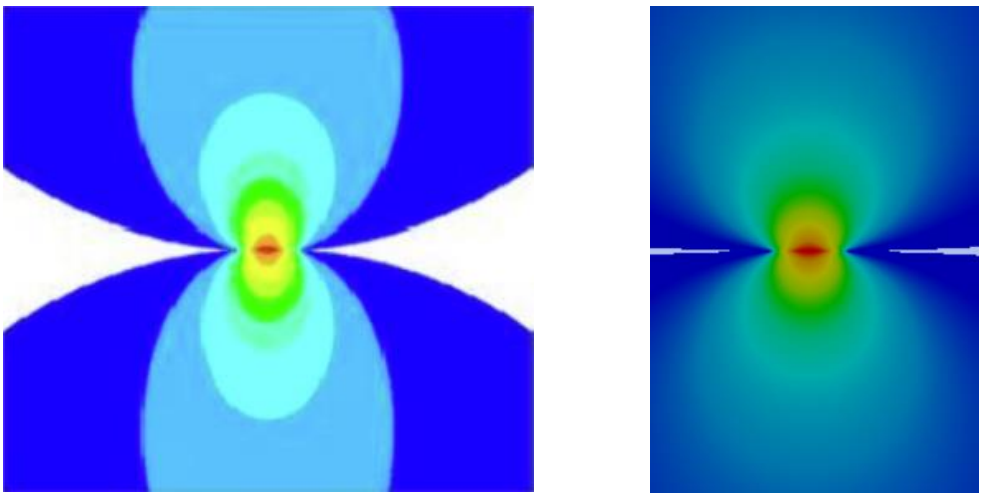


Figure 42: results comparison for cylinder-cylinder contact (left side [Sug21])

3.2 SPHERE-SPHERE CONTACT

For the second mesh sensitivity analysis, a 3D study will be carried out, this time simulating the contact between two spheres. Like on the first contact analysis. In this case, there is also an analytical solution with an exact result for the maximum stress. This can be found in Wang's paper [Wan13b] and following the next equation.

$$P_{max} = \frac{1}{\pi} \cdot \sqrt[3]{\frac{6*F*E^2}{R^2 \cdot (1-\nu^2)^2}} = \frac{1}{\pi} \cdot \sqrt[3]{\frac{6*752.21307*210^2}{6.47^2 \cdot (1-0.3^2)^2}} = 3475.75\text{MPa} \quad (10)$$

P_{max}	MPa	Maximum pressure	F	N	Force
R	mm	Sphere radius	ν	[-]	Poisson ratio
E	MPa	Young Modulus			

3.2.1 GEOMETRY GENERATION

Regarding the geometry generation, two identical spheres were created with a radius of 6.47 mm and both with a point contact instead of a line contact seen in the previous example. As in the previous simulation, both spheres are also made of structural steel with the same mechanical properties as the ones shown in Table 2: Mechanical properties of structural steel.

In order to reduce the number of elements of the mesh, a geometry behavior was introduced in the simulation. In this case, instead of selecting a plane stress behavior, in this specific simulation, the best approach is selecting the axisymmetric behavior. As it was explained in chapter 3.1.1 Geometry generation, what this behavior does is revolving the geometry around the Y axis in order to create a 3D geometry that will be then simulated. Taking advantage of this, the geometry and mesh generation needs to be only of one half of a slice of a sphere as it is shown in the next image.

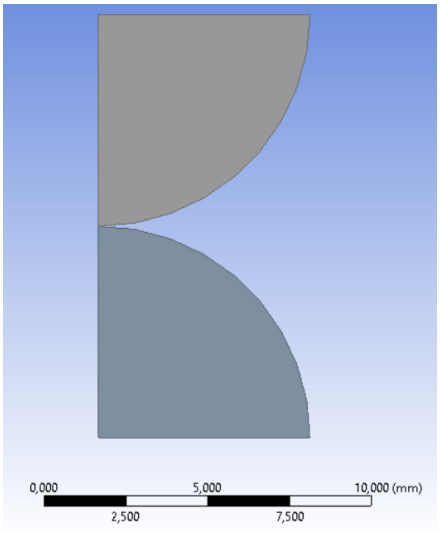


Figure 43: Geometry for sphere contact simulation

3.2.2 MESH GENERATION AND BOUNDARY CONDITIONS

In terms of the mesh generation, in this case, the approach chosen was directly the spherical refinement region with the center at the contact point. This approach was the one that showed the best and most optimal usage of the refinement elements without wasting small elements on non-important areas. Regarding the meshing method, a quadratic order with a structured mesh was still maintained for this simulation.

Taking this into consideration, two different steps needed to be taken. In the first step, the refinement radius was selected, and once this parameter was fixed, the refinement size was studied in order to compare the results with the cylinder contact simulation. In the following picture, an example of the refinement mesh can be seen.

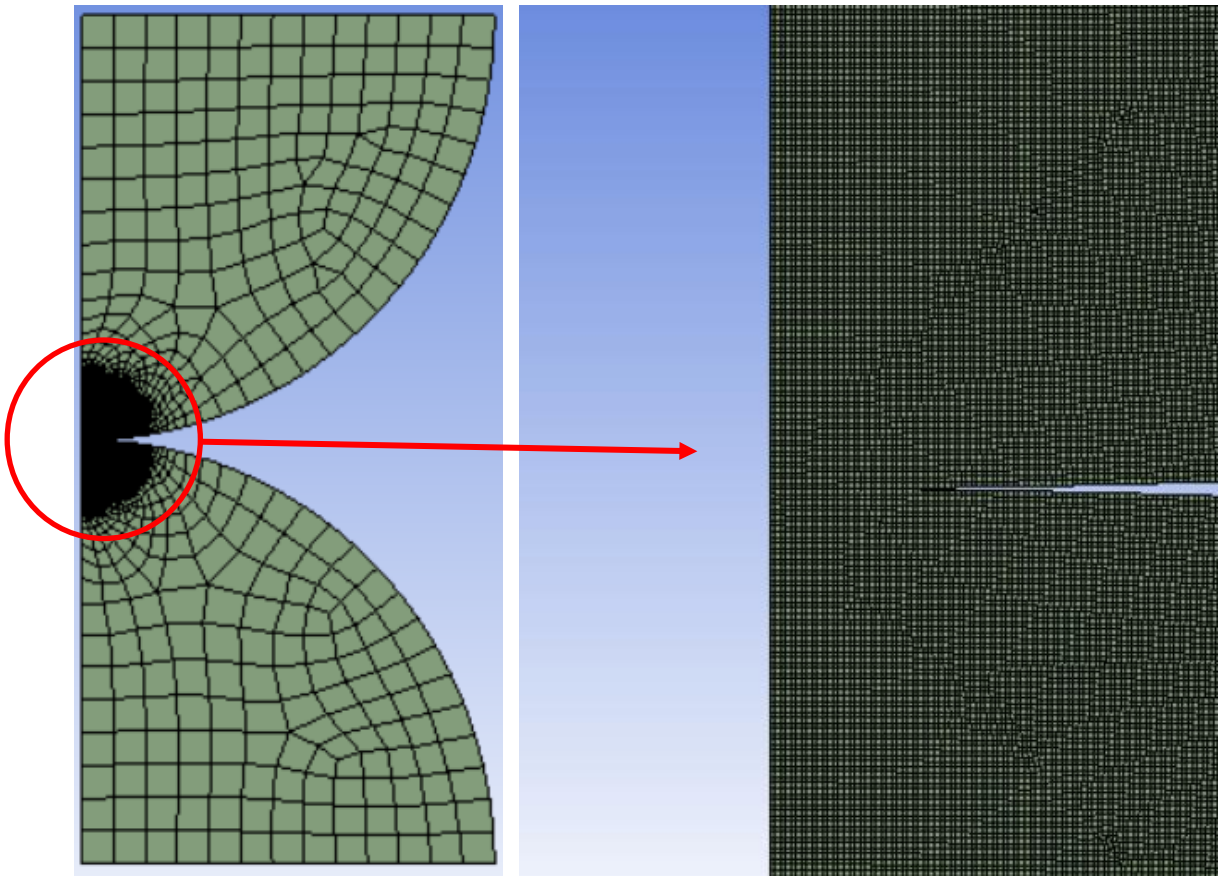


Figure 44: mesh refinement sphere contact simulation

In terms of boundary conditions, these are very similar to the ones shown in the previous simulation. The bottom sphere needs to stay fixed, while on the top sphere, a distributed force is applied to compress both spheres and generate the stresses on the contact point. In order to make easier the application of the forces and supports, both spheres have been cut in the middle, creating a visible flat surface where the boundary conditions can be placed. In the following image, the depicted setup can be observed.

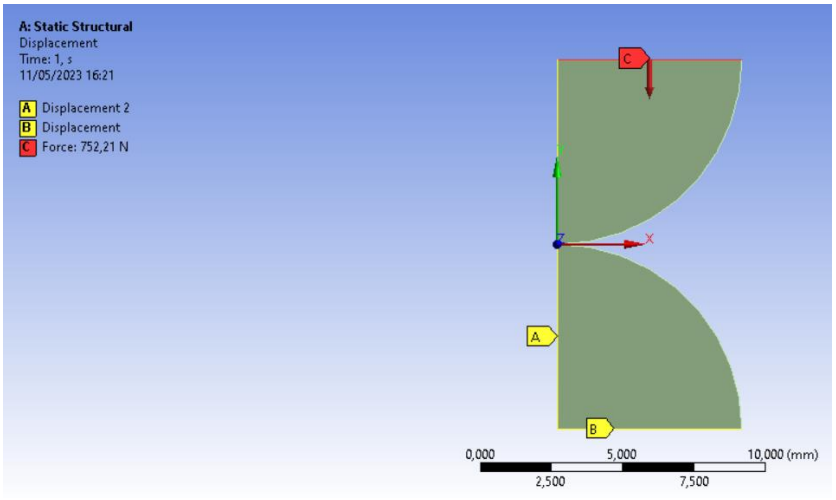


Figure 45: boundary condition setup sphere–sphere contact

3.2.3 REFINEMENT RADIUS DETERMINATION

As explained earlier, the first parameter to determine is the refinement region radius to capture best the stress behavior without wasting elements and creating a too-big region. As a reference, in the previous cylinder simulation, the optimum radius for the refinement was approximately 0.5 mm as shown in Figure 39.

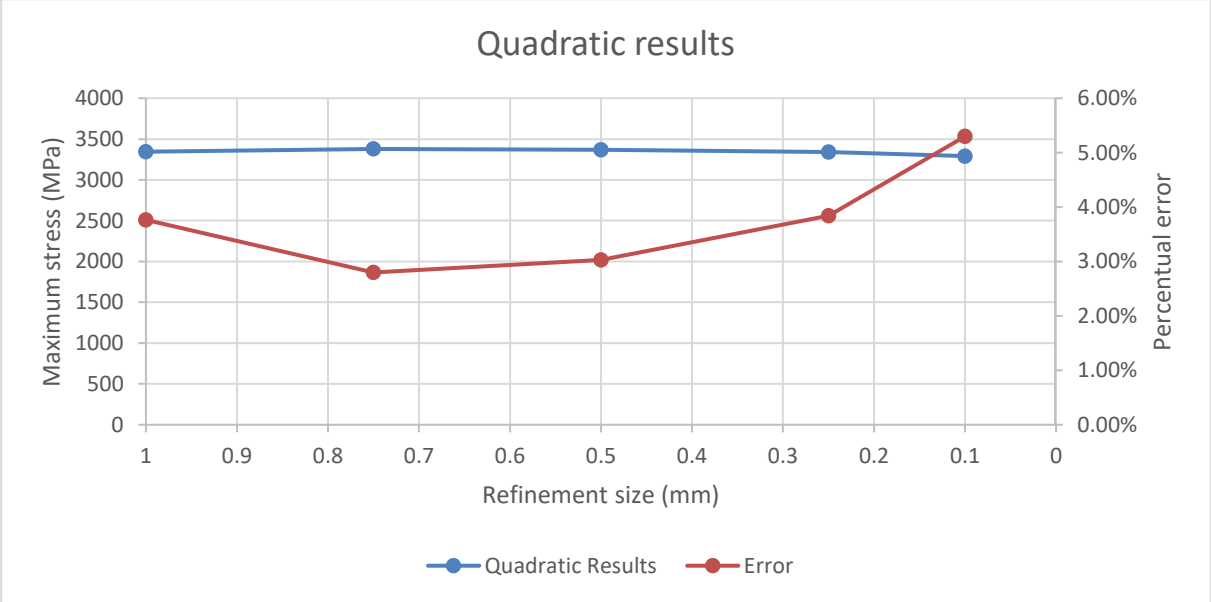


Figure 46: refinement radii analysis sphere - sphere contact

In the previous graph, on the X axis, the radius of the refinement region is plotted, while on the right Y axis, the percentage error is observed and on the left side the maximum pressure in MPa.

From this graph, it can be derived that the simulation with less error is the one with a radius of 0.75 mm, while the one with a 0.5 mm radius performs a similar solution reducing the number of elements used in the simulation. This allows us to conclude that the optimum refinement region, as well as with the cylinder contact, is a radius of 0.5 mm. In the following image, the different simulation results with the different refinement regions can be observed.

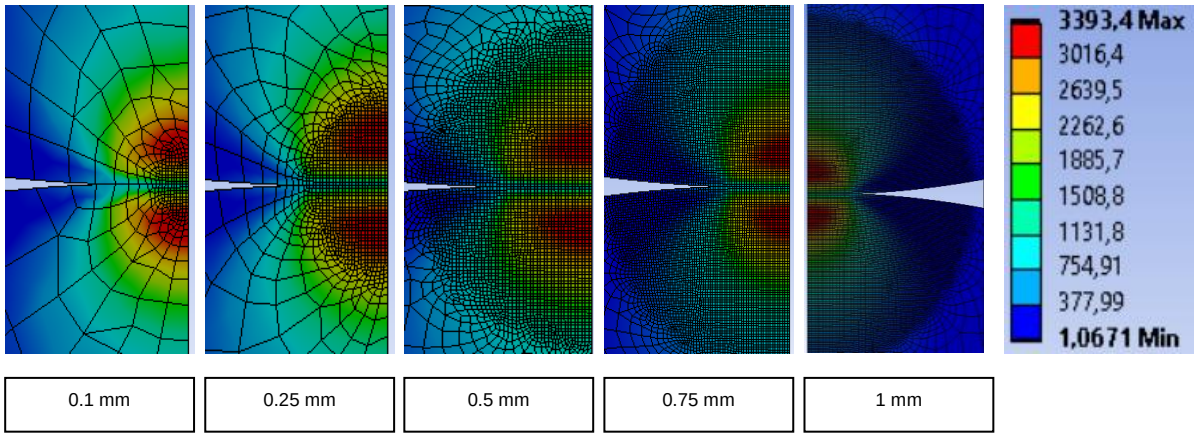


Figure 47: plots of refinement radius simulation for sphere contact (Stress shown in MPa)

As can be confirmed with the plots, the refinement region with a radius of 0.75 mm covers the entire area affected by stresses, while the region with a radius of 0.5 mm refines the area with higher pressures leaving outside the refinement a small region with very low stresses.

3.2.4 REFINEMENT SIZE DETERMINATION

Once the radius of 0.5-0.75 mm is decided, a mesh sensitivity analysis was carried out. This time the refinement size varied between 0.3 mm and 0.003 mm. A lower value than this could not be achieved due to the high ram demand and simulation times. In the following graph, in blue, the maximum pressure is plotted in quadratic order and in red the percentage error of the simulation in comparison with the reference analytical value.

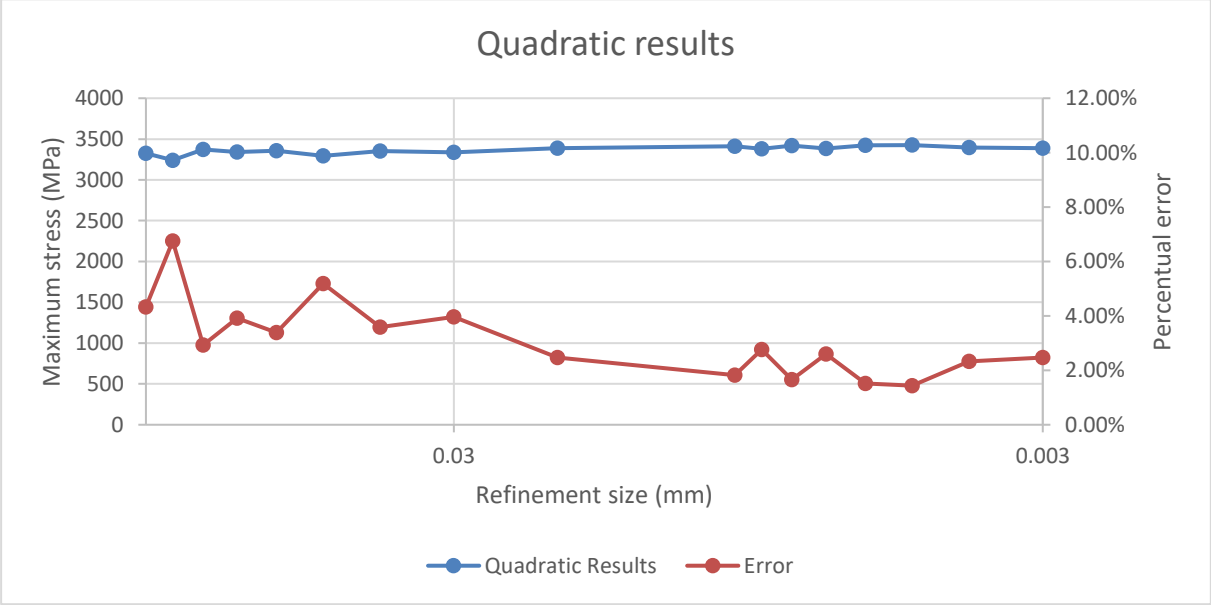


Figure 48: maximum stress results of sphere contact

As can be observed, the results have a very similar shape to the one extracted from the cylinder simulation in Figure 40, but in this case, the percentual error is much smaller in comparison with the other simulation. If the simulation with a refinement size of 0.01 mm is taken as a reference, in this case, the error is somewhere around 2%, while on the cylinder contact simulation is 5.5%.

Seeing these results, having a refinement size below 0.01 mm has no sense, since the results are almost identical with increasing simulation times, while increasing the refinement size does not distort a lot the result if the elements are not above 0.08 mm approximately.

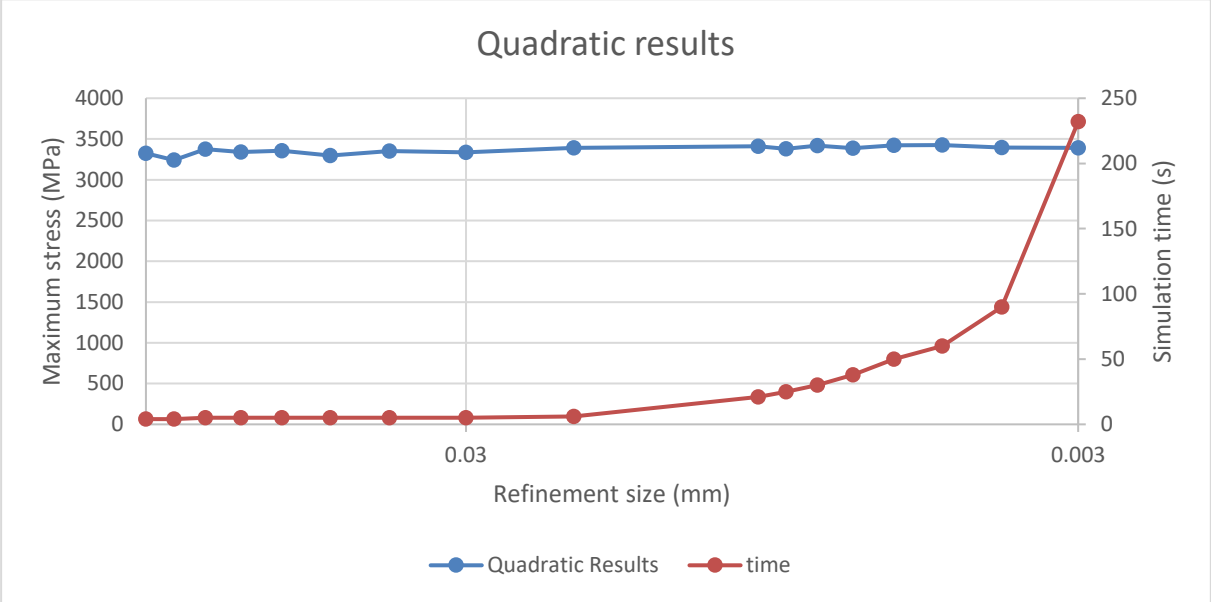


Figure 49: simulation time for sphere contact simulation

As seen in the previous graph, the simulation time also increases exponentially having a steep increase after the 0.01 mm refinement, confirming once more that the best refinement size when possible is between 0.05 and 0.01 mm.

3.2.5 QUALITATIVE VALIDATION OF THE RESULTS

As well as it was done in the first simulation, in this chapter, qualitative validation of the stress pattern will be performed. In this case, in comparison with the cylinder–cylinder contact, the maximum stress is not located in the contact point, but on a region slightly above the contact point. The stress pattern follows an elliptical distribution created due to the deformation of the spheres during contact.

In theory, the contact between two spheres should be a point contact, but due to the deformation during the application of the force, this deformation is not symmetrical causing an elliptical contact region between the two spheres. This uneven deformation also generates an uneven stress distribution in the spheres, causing the displacement of the maximum stress point, in this case, moving it slightly above the contact area. In the following

image, a comparison between the results of a similar simulation done by Zhanjiang Wang and the one performed in this thesis can be observed [Els12, Wan12].

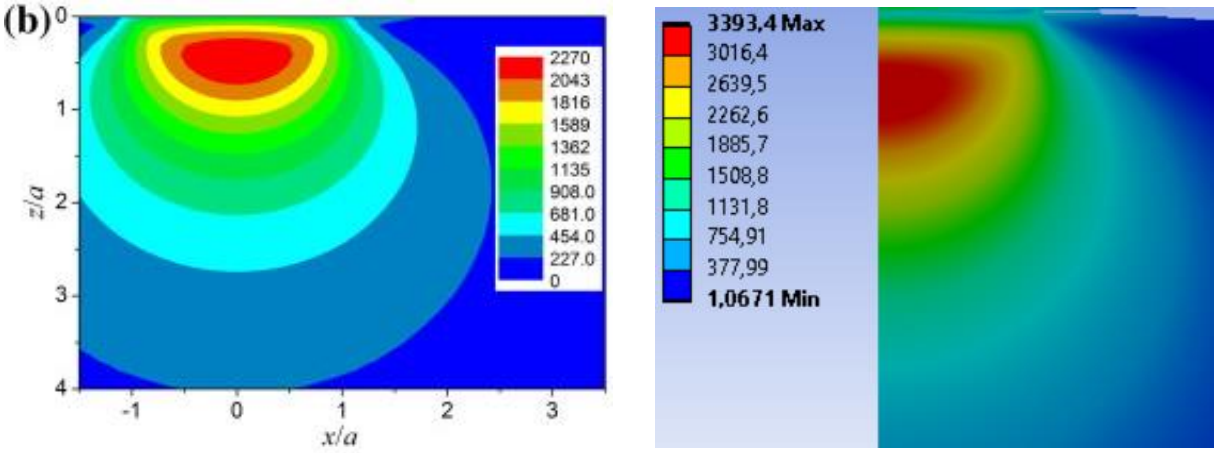


Figure 50: validation of stress pattern for spherical contact simulation

3.3 CONCLUSIONS OF MESH SENSITIVITY ANALYSIS

In this chapter, two mesh sensitivity analyses were performed, in order to analyze the impact of the mesh size and refinements on the results for two hertz contacts. First of all, a cylinder–cylinder contact was performed and secondly a sphere–sphere contact. In both contracts, the withdrawn conclusions are very similar.

In terms of refinement geometry, the optimum geometry is a spherical refinement, as the stress pattern also follows a spherical shape, and this is the optimum approach for optimizing the number of elements of the mesh. In terms of refinement radius, in both studies, the best-performing mesh was the one with a radius between 0.5 and 0.75 mm, the first one the result of the cylinder contact and the latter the result obtained on the sphere contacts. Finally, regarding the refinement size, multiple factors affect this result, but as a preliminary study, a good approach would require a mesh with a refinement between

0.05 and 0.01 mm, or as a percentage, a refinement between 1% and 0.2% of the characteristic length, in this case, the radius of the spheres and cylinders.

This leaves a very good starting point for generating the mesh of the final simulation that will be performed in this thesis and also is useful to take into consideration the percentage error that the following simulations will be given.

4 GEARBOX SYSTEM SIMULATION

In the following chapter, the simulation of the geometry of interest will be carried out. During this chapter, the different steps, and processes to perform the simulation will be explained, from the geometry generation to the analysis and evaluation of the results.

After this chapter, a fully functional simulation setup will be exposed capable of simulating multiple different geometries and materials to optimize and find out what is the perfect combination of parameters for every application.

4.1 GEOMETRY GENERATION AND MODIFICATION

As has been shown previously, the first step to creating a simulation is the generation of geometry. In this case, the original geometry was already given as a SolidWorks assembly containing the gear and the screw as shown in Figure 51.

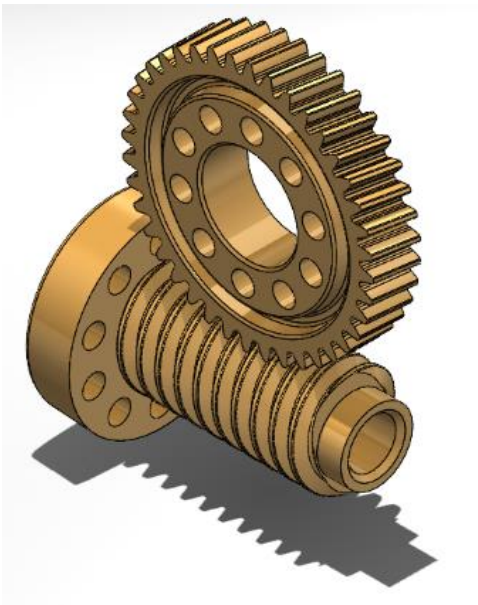


Figure 51: geometry assembly in SolidWorks

If the system were smaller and with fewer details, the geometry could be taken directly to the meshing software in order to keep going with the simulation procedure, but as the geometry has a lot of unnecessary details for this application, it will be worked on in the geometry editor of ANSYS.

When opening ANSYS, the first step is to select a simulation environment, in this case, as it is a mechanical static simulation, the most appropriate environment is the static structural module. Under the static structural environment, different sub-environments are located.

The first module is "Engineering Data". In this module, all the materials required for the simulation are created. Here, any kind of mechanical property can be modified or added to existing material to characterize the material as close as possible to reality.

The next module is "Geometry", where the geometry of interest is modified, and other support volumes are created to improve the quality of the mesh. This module can be operated by different software, such as Design Modeler, the one selected for this application, or Space Claim. For this simulation, the design modeler was selected due to its much simpler usage and because an already existing file of the geometry is available in another CAD program. If no geometry file is available and the complete geometry needs to be created in ANSYS, Space Claim is a much more complete software with more tools and more control of the operations.

In this specific environment, all submodules from "Model" to "Results" are all gathered in one software called "Static Structural – Mechanical". "Model" is where the mesh is defined, inside the mesh it is also included the contact definition, mesh refinement regions, and other operations. Inside "Setup" the simulation setup is created as its name indicates. This includes the fixing points, the load application, the joints, and degrees of freedom definition, etc. Under "Solution" there are not too many options, as this is just the solving algorithm to perform the calculations for the simulation. And last but not least, under "Results" the solution of the simulation can be examined with the creation of multiple plots, graphs, and charts to display any type of information needed to evaluate and validate the results

of the simulation. In the following picture, the environment of the static structural software can be seen, where “Model” “Setup” “Solution” and “Results” are included.

After seeing this overview of the simulation software, a more in-depth look at every module will be shown in the following chapters.

4.2 *ENGINEERING DATA*

As has been explained before, under engineering data, all mechanical properties for different materials are defined. In this case, these previous simulations have been done with both elements made of structural steel, a material preconfigured in ANSYS with all the required properties to perform a simulation as shown in Table 2. In the following figure, the workspace of the engineering data environment can be seen.

Although these first simulations have been made with structural steel, the final simulation results will be made with Vestakeep 4000 FC30 PEEK CF, by Evonik, as this is the material the gears are made of. In the following table (Table 2), the most important characteristics of this material are exposed. This information is extracted with the help of the software created by the company KISSsoft AG [KIS23]. Two additional materials will be used for validation purposes, and these are PEEK and Steel, which properties used are also shown in Table 7 and Table 8 respectively.

Value	Unit	Worm	Gear

Breaking strength	MPa	120.15	120.15
Yield strength	MPa	76.83	76.83
Young modulus	MPa	10075	10075
Poisson number	[-]	0.44	0.44

Table 6: PEEK CF – PEEK CF mechanical properties

Value	Unit	Worm	Gear
Breaking strength	MPa	-	-
Yield strength	MPa	-	-
Young modulus	MPa	4170	4170
Poisson number	[-]	0.4	0.4

Table 7: PEEK - PEEK mechanical properties

Value	Unit	Worm	Gear
Breaking strength	MPa	-	-
Yield strength	MPa	-	-
Young modulus	MPa	4170	210000
Poisson number	[-]	0.4	0.3

Table 8: PEEK - Steel mechanical properties

4.3 GEOMETRY

Under geometry, the modifications to the SolidWorks assembly will be performed, in order to simplify the geometry and make easier the generation of the mesh. For ANSYS to be able to read the CAD data, it needs to be imported as a .STEP file. This type of CAD file allows one to read all the geometry data without loading the different operations to achieve the final geometry. This means that the access data is only the outside shape of the geometry, and this cannot be modified later by accessing the individual operations that were created to generate the geometry shape.

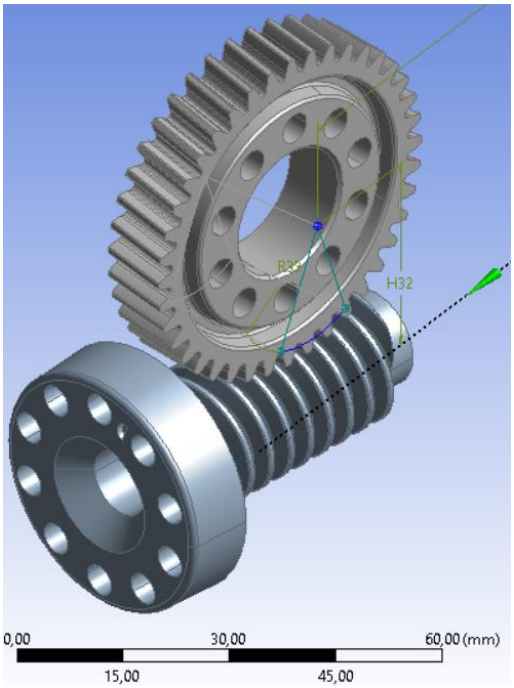


Figure 52: geometry loaded in design modeler.

Some of the most relevant data on the gear assembly is gathered in the following table and it will be used to determine the final dimensions of the reduced geometry for the simulation.

Variable	Symbol	Unit	Worm	Gear
Axis distance	a	mm	34.78	
Axis crossing angle	∑	º	90	
Gear ratio	I	[-]	20	
Module	m_n	mm	1.25	
Teeth number	Z	[-]	2	40
Pitch diameter	D_p	mm	19.135	50.432
Teeth thickness	b	mm	3.32	3.32
Helix angle	$\beta_{1,2}$	º	82.4930	7.5070
Normal pressure angle	α_n	º	20	

Table 9: relevant geometric values of the gear assembly

The first step before loading the geometry to ANSYS is making sure that the contact point is correctly positioned, in this case, it must be at the pitch diameter of the top gear. In order to check this, some measurements must be checked:

- Checking the distance between axes (34.78 mm)
- Checking the axis crossing angle (90º)
- Checking the contact between both surfaces

This last step is done first on SolidWorks [Das15], with the help of its contact detection tool, to get an approximation of the relative position of the gears and then it is completed in the design modeler module of ANSYS, with the contact tool provided by the meshing software of ANSYS. This is done, because sometimes when the required precision is very

small and the file needs to carry some small details, the STEP file generates some error regarding the dimensions or the positioning of the bodies. This final check in the design modeler allows for eliminating the possible error introduced by the STEP file into the system that would cause overlapping geometries and a miscalculation of the contact.

Once the geometry file is loaded, the first modification is to reduce the geometry to the effective part that will be suffering stresses during the simulation.

First of all, focusing only on the top gear, its volume can be reduced notably. The most direct reduction is related to the number of teeth, in this case, according to Frühe [Frü12], the simulation is only relevant to those teeth that are in contact and may suffer stress. Another consideration is the internal radius of the gear and the angle space left after and before the gear teeth to ensure a suitable model is completely compatible with the complete gear. In the following image, extracted from Frühe's dissertation [Frü12], a summary of the dimensions to follow can be seen.

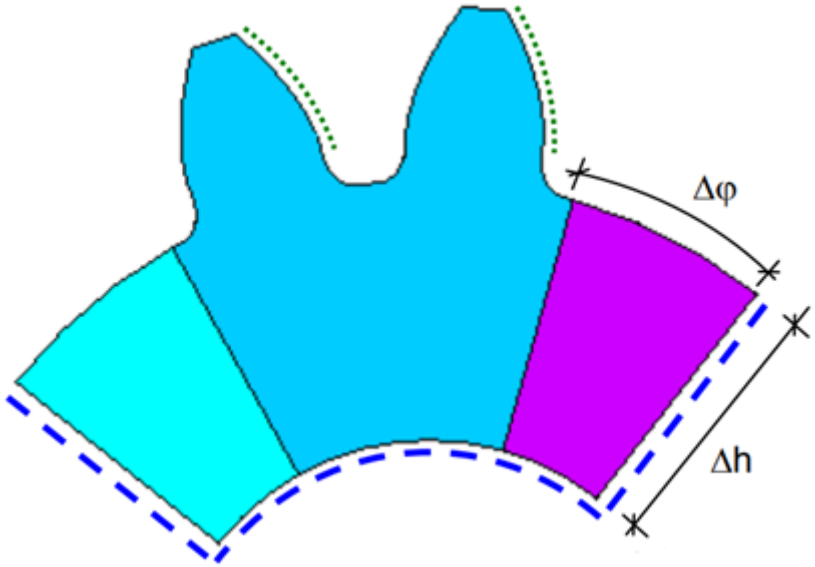


Figure 53: minimum dimensions to simulate an equivalent gear. [Frü12]

Where in the following equations $\Delta h = 3 \cdot m_n \approx 3.75\ mm$ (11) and $\Delta\varphi = \frac{360}{z} = 9°$ (12), these dimensions are explained.

$$\Delta h = 3 \cdot m_n \approx 3.75\ mm \qquad (11)$$

Δh	mm	Thickness of the gear	m_n	mm	Module

$$\Delta\varphi = \frac{360}{z} = 9° \qquad (12)$$

$\Delta\varphi$	º	Margin border	z	[-]	Number of teeth

To analyze all contact options possible, the gear will be reduced to only 3 teeth. With this reduction, a main contact on the middle teeth can be examined, with possible entering and exiting contacts on the right and left teeth, each in a different location. Regarding the wholes and details of the gear, these will also not affect the stress behavior of the final simulation, making possible also the elimination of these elements to make the geometry simpler.

Another modification that is needed is the adaptation of the end of the thread in the screw. As the thread is not parallel to the screw, when cutting the screw into the section of interest, there will always be a sharp edge at the end of the thread. This sharp edge will cause bad-quality elements and will probably affect the precision of the results in the whole mesh, not only on the sharp edge. Due to that, a refinement on the cut of the screw's thread needs to be performed, allowing a much cleaner cut, that will allow the creation of a mesh with better element quality. In Figure 54, both thread ends can be seen, on the left side the thread ends with a straight cut and on the right side the modified cut.

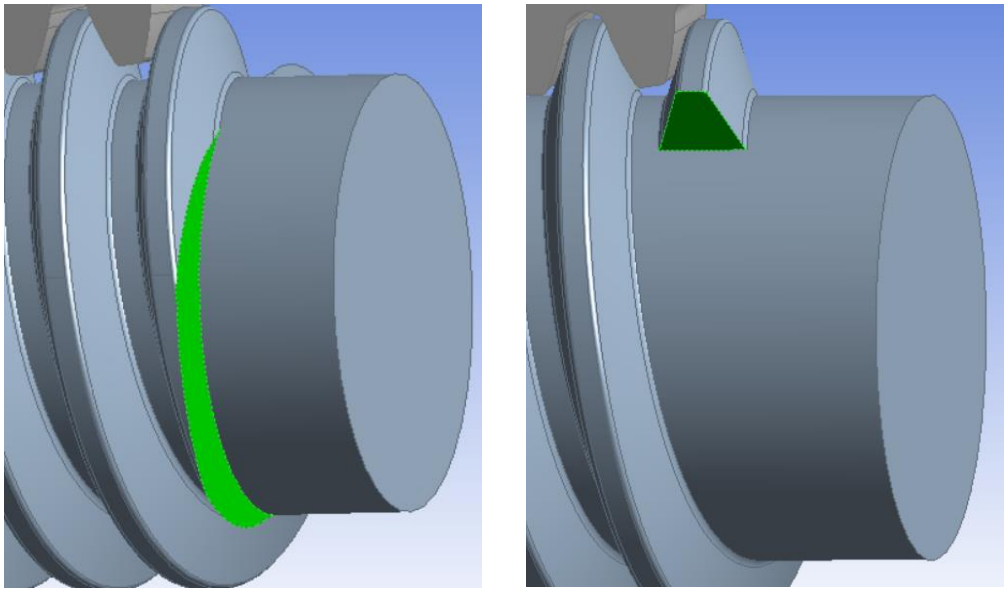


Figure 54: thread edge refinement

After those changes, other modification to reduce the computational time and make a more resource-efficient simulation is, for example, hollowing the screw to reduce the number of elements in the mesh. With all these modifications applied, in the following figure, the final geometry can be seen.

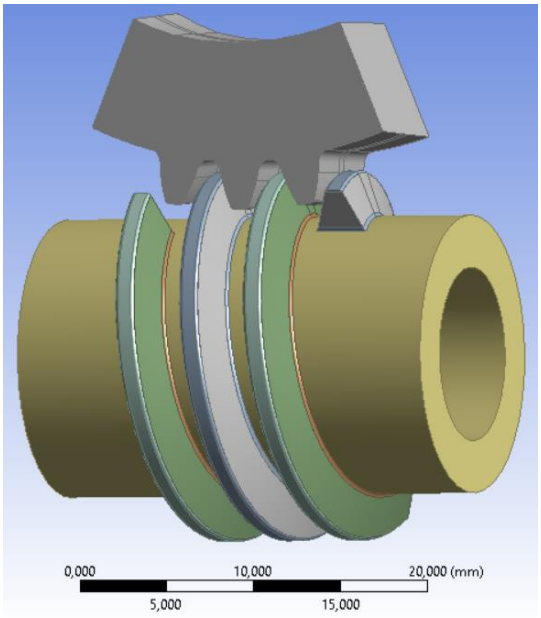


Figure 55: final geometry to be simulated.

To reduce even further the geometry, a study has been carried out in which two different geometries have been tested under the same boundary conditions and with the same mesh parameters. In this case, the two tested geometries have been the one observed in Figure 55 and a reduced variation of this geometry eliminates the $\Delta\varphi$ extension of the gear shown in Figure 53.

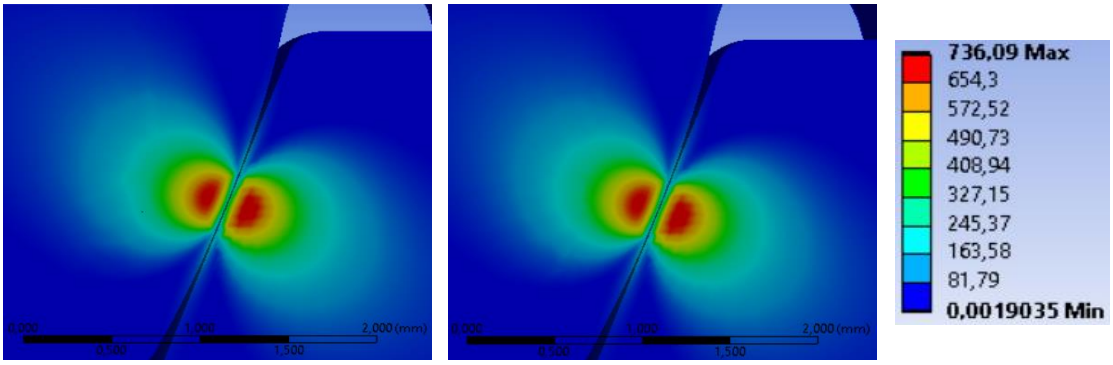


Figure 56: Stress distribution (MPa) of full geometry (left) vs reduced geometry (right)

As can be seen in Figure 56, both geometries show identical behavior regarding stresses. The maximum stress found in both geometries is approximately 736 MPa, with a difference between both simulations being less than 0.05 MPa or 0.007%. The shape of the stress distribution around the point of maximum stress also shows lots of similarities.

Now, if the deformation plot on the contact surface is observed in Figure 57, it can also be said that both geometries show very similar deformation patterns. It must be remarked that the maximum deformation differs slightly between simulations, with a difference of 0.2545 µm or 7.7% of the total maximum deformation. This can be considered negligible if it is taken into consideration the small displacements that are being calculated, concluding, that both geometries can be considered equivalent for this type of simulation and from now on the geometry used for future simulations will be the one without the $\Delta\varphi$ extension in both sides of the gear.

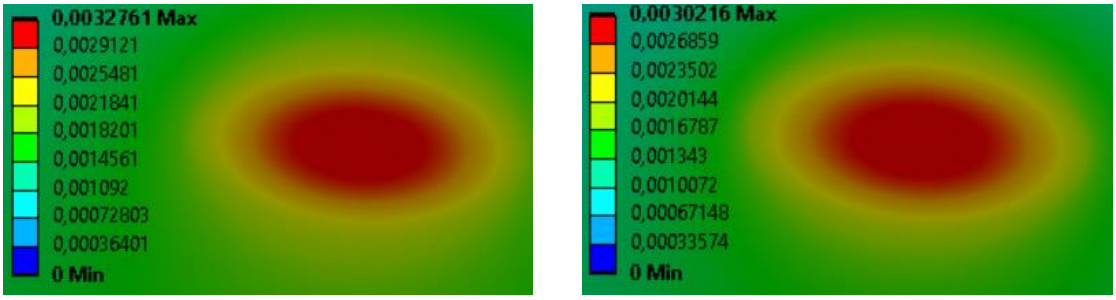


Figure 57: surface deformation (mm) of the complete geometry (left) vs reduced geometry (right)

4.4 MODEL (MESH)

This step is the most important as it was mentioned in the previous chapters. For this simulation, the same strategy was applied as the one concluded in the mesh sensitivity analysis. A structured mesh with a quadratic element order will be generated.

To structure the mesh more efficiently, the geometry was divided into different regions, each one with different refinement demands. Those regions are:

- Main gear
- Worm gear body
- Main thread bodies
- Top thread bodies
- Bottom thread bodies

For the meshing of the main gear, it must be considered special characteristics. The main area of interest is located in the contact point around the teeth of the gear, the main body located at the top is a secondary region that will not have any stresses during the simulation. Considering this, the refinements will only need to be applied to the teeth of the gear.

For creating the refinements, two main refinement strategies will be applied. For the zones where no stresses will take place, the meshing will be the one created with the standard parameters of a target size of 1 mm and a maximum size of 2 mm, but for smaller regions, these parameters are too big to capture all the details. For curved regions, edge refinements have been applied specifying a number of divisions for every edge to ensure capturing the curvature correctly, and for the contact point, a more in-depth refinement was applied. As seen in the previous mesh sensitivity analysis, the stress pattern of this type of contact has a spherical distribution, being this the optimal refinement geometry. ANSYS has a specific refinement command called "Sphere of influence" where after selecting the center of the sphere, the radius, and the refinement size, it creates a refinement sphere in that location.

For choosing the center of the spheres, a first approximation was done to calculate where the contact point for each contact will be placed. Once this approximation was carried out, the following centers were chosen.

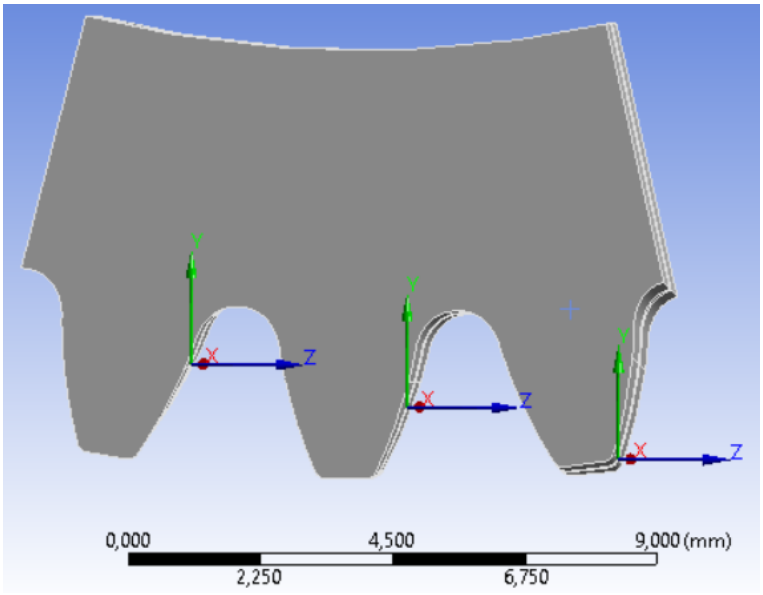


Figure 58: positioning of the centers of the spheres of influence

Regarding the sphere radius, as evaluated in the mesh sensitivity analysis, 0.75 mm was selected as the optimum radius to capture all the stresses around the contact point and

for a refinement size, 0.03 mm was the selected size as this is approximately 1% of the pitch diameter as concluded in Chapter 3.3: Conclusions of mesh sensitivity analysis. Once these refinements were applied, the following figure shows the final result mesh.

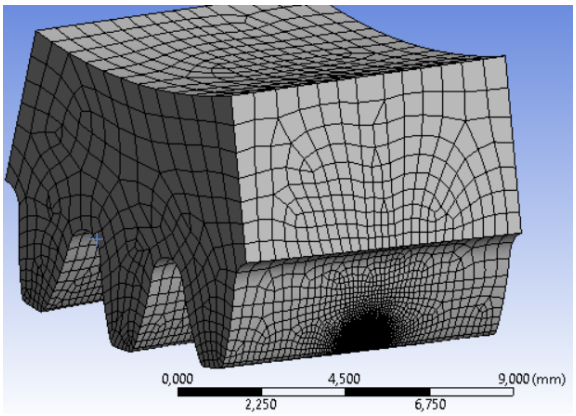


Figure 59: isometric view of gear mesh

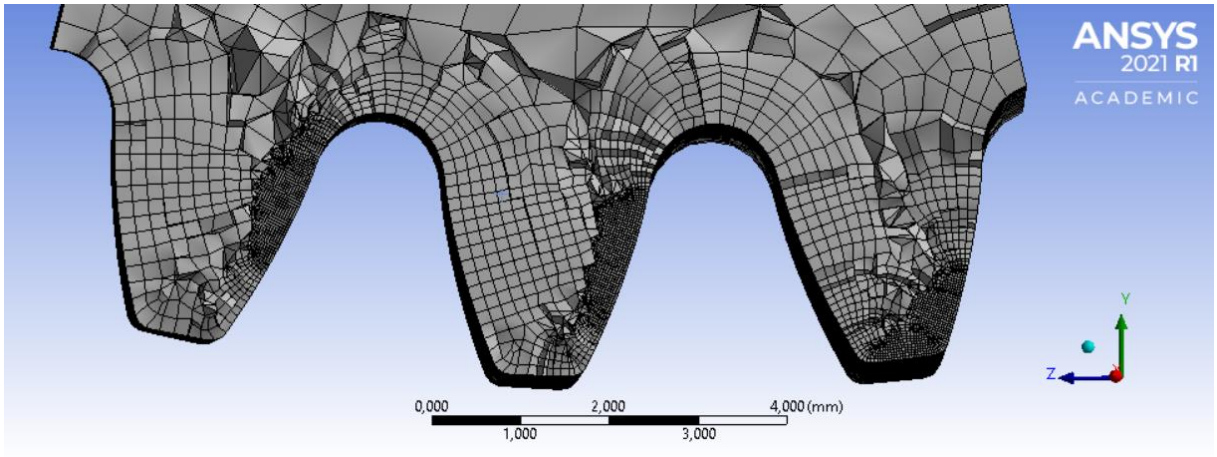


Figure 60: cut plane displaying refinement regions.

For the worm gear, a different approach was taken. In this case, refinement is needed in the worm teeth, reducing the elements spent in the main cylinder body of the worm gear. To maintain a structured mesh around the complete geometry, edge refinement was applied here too. Several divisions were applied on all the edges of the worm teeth to ensure a uniform mesh distribution except where the contact point is located. In that region, a division of geometry was created to increase the control of the refinement in that specific

area. This division was created by rotating the longitudinal plane by 10º on each side, creating a 20º refinement region where the element density is considerably bigger than the rest of the worm gear achieving the following mesh.

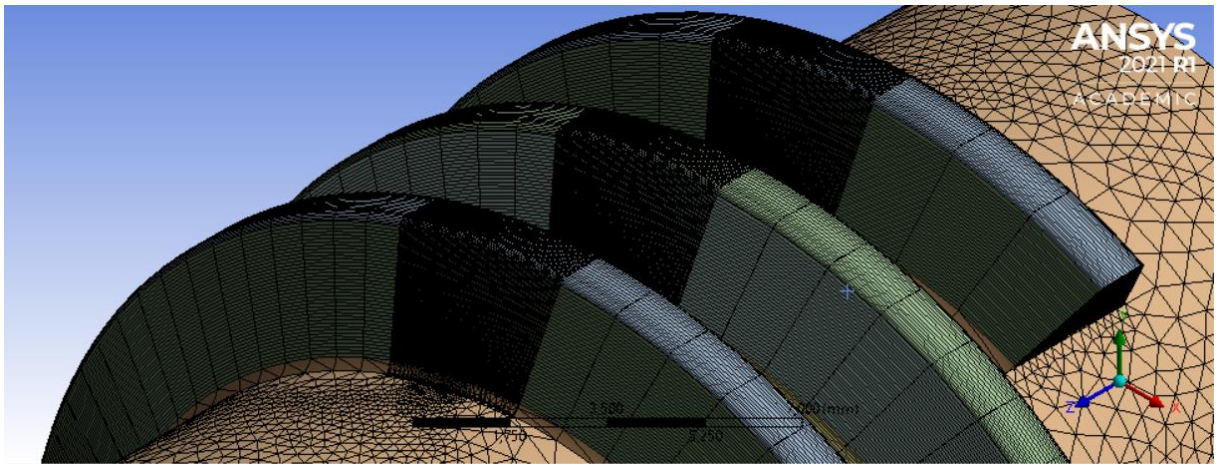


Figure 61: isometric view of worm mesh

4.5 SETUP

4.5.1 CONTACT DEFINITION

For the contact definition, the first thing to remark is that 3 main contacts must be defined. The most important one is the one located in the middle tooth, as this contact will be present in all simulations and its contact point is located at the pitch diameter at the beginning of the simulation, so it will be the contact taken as a reference for all the study of the results. This contact, as it is always active, has some different characteristics in comparison with the other two secondary contacts.

The first thing to do when defining a contact is to decide which is the contact and the target face. For the main contact, the following surfaces were selected as contact and target faces.

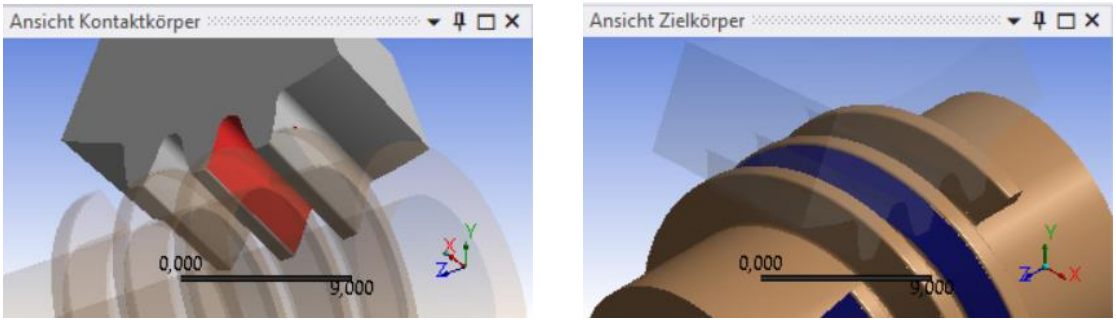


Figure 62: main contact definition

After selecting the contact surfaces, to reduce the computational resources used and not have to calculate the contact for all the nodes for every time step, the contact calculation was reduced to only a circle region with a radius of 1 mm with the center of the contact point. This ensures a good contact placement with the selection of the complete surfaces to find the exact location of the contact point and once this is located, for the solution of the contact, only the elements located in this 1 mm radius circle with the center in the contact point are computed. Once this is correctly defined, the type of contact needs to be selected, choosing between frictionless or with friction, depending on the simulation that needs to be calculated and lastly, the contact behavior needs to be defined.

ANSYS has multiple contact behaviors to allow an easier contact definition when the automatic detection of the contacts based on the geometry does not work correctly and in this thesis two of the behaviors have been used. In the first place, when the user knows 100% that the contact is taking place, is active from the beginning of the simulations and both surfaces are exactly in contact at that point, the adjust-to-touch behavior is selected. What this behavior does is that it selects the nodes of the mesh that are detected in the contact and joins them together so that at the start of the simulation, those nodes are already in contact. This allows for minimizing possible geometry errors that lead to really small gaps in the geometry and causes dynamic reactions in the contact area at the beginning of the simulation. This is only a computational adjustment and the geometry itself is not modified.

The second behavior is the “add offset – no ramping”. This is the standard option and allows the user to manually introduce a geometric offset to close the gap between the surfaces. This is the method used for these simulation contacts. This method is the selected one, because although the contact in the middle is always present, both left and right contact might activate or deactivate during the simulation, so they must be defined with this behavior, as they are not always in permanent contact. In addition, if the geometry was correctly placed in the previous step, both behaviors for the contact in the middle should be equivalent, allowing to use of only one type of contact for all of them.

After defining all the contact options, the ANSYS contact tool was used to check if the contacts were correctly defined and check the status, the initial gap, and the initial penetration between the contact surfaces. In this case, the following pictures show the results of the defined contacts.

As it is shown, the contact of the tooth in the middle is active at the beginning of the simulation without any gap, while the top and bottom contacts of the teeth after and before the middle teeth show a gap with a contact status “Near”, that means that the contact is not active, but is close enough to be computed in case it will become active in a future timestep of the simulation.

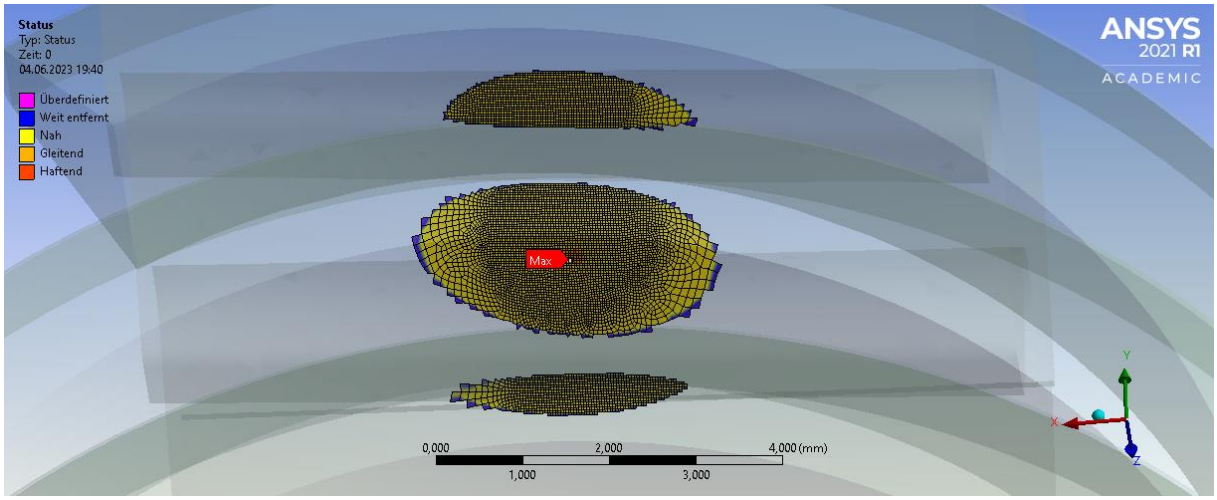


Figure 63: contact status of the three defined contacts

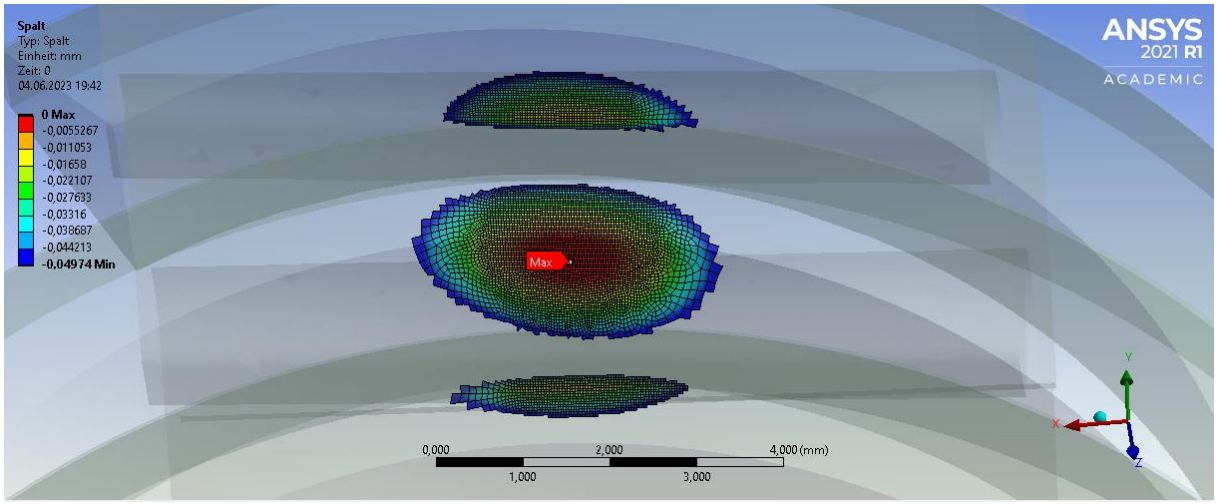


Figure 64: initial contact gap (mm)

4.5.2 BOUNDARY CONDITIONS

Regarding the boundary conditions, two different parameters need to be defined. First of all, the fixing of the two bodies needs to be set up so that the system does not have complete freedom of movement. To achieve this, the helical gear is considered a fixed body, having its inner radius faces completely fixed to experiment with how it deforms with the movement of the worm screw. As this is only allowed to rotate around its axis. To achieve this, a cylindrical fixing condition is forced to the inner faces of the worm gear, allowing only the tangential rotation, and fixing the rest of the degrees of movement.

Once the bodies have been fixed, the next step is to introduce the force into the system, in this case, the worm screw moves due to a rotational moment applied on one of its ends making the screw rotate around its axis and pressing the screw faces into the teeth of the helical gear. In terms of magnitudes, the experiment that needs to be simulated applied a moment of 250 Nmm at the screw side, or 5000 Nmm in the helical gear side.

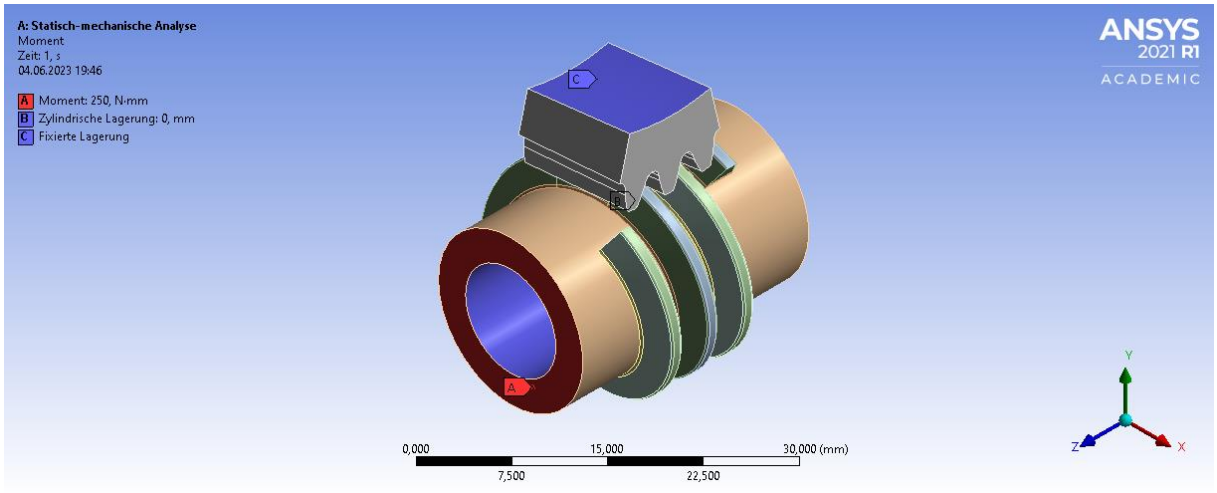


Figure 65: boundary conditions definition

4.6 RESULTS (FRICTIONLESS)

The first simulation that was achieved consisted of a static simulation, in which the geometry is moved in small steps to analyse the complete rotation of the worm screw. This method allows for an increase in the number of elements, and thus the precision, due to the less resource requirement that the static simulations demand in comparison with a transient simulation.

In terms of materials, the results shown in this chapter are of the plastic gears with the properties shown in Table 6, and without any friction activated. As the desired rotation is the one according to one tooth moving to the next position, this means a 9º rotation in the gear or a 180º rotation in the screw, due to the 1:20 ratio of the teeth. The steps done correspond to a 0.9º rotation on each step allowing a complete analysis with 10 simulations.

In the following table, the maximum stress recorded in each tooth is monitored. This will allow following how the load distribution is transmitted, in case of two or three teeth

contact, depending on the position of the gears and how the contact point varies for every tooth.

The last simulation corresponding to the 90º rotation is the same position as the initial simulation, but in this case, the teeth have advanced one position, meaning that the pressure of teeth 1 at 90º rotation corresponds to the pressure of teeth 2 at 0º rotation and so on for the rest of the teeth. This is done to confirm that a full position advance is completed, as the values correspond with the expected values obtained at the initial position.

Another valuable piece of information that can be extracted from the table, is that a three-teeth contact happens only on a +- 1º rotation of the top gear taking as a reference point the moment in which the middle teeth make contact at the pitch diameter.

-	Teeth 1	Teeth 2	Teeth 3	Teeth 4

Location	Screw	Gear	Screw	Gear	Screw	Gear	Screw	Gear
0	0	0	223.97	189.15	79.87	77.38	145.69	173.98
0.9	0	0	239.91	222.54	81.00	79.14	73.02	113.22
1.8	0	0	416.85	213.50	79.55	78.03	0	0
2.7	0	0	630.74	168.46	77.84	77.94	0	0
3.6	0	0	130.90	113.78	74.19	76.47	0	0
4.5	0	0	88.45	78.05	72.27	75.73	0	0
5.4	0	0	82.48	75.98	71.79	77.25	0	0
6.3	0	0	78.01	72.53	93.72	111.48	0	0
7.2	0	0	78.53	74.22	136.95	152.1	0	0
8.1	0	0	79.71	76.29	155.34	178.56	0	0
9.0	214.45	195.39	79.65	77.10	146.78	178.24	0	0

Table 10: Maximum stress in MPa for frictionless contact

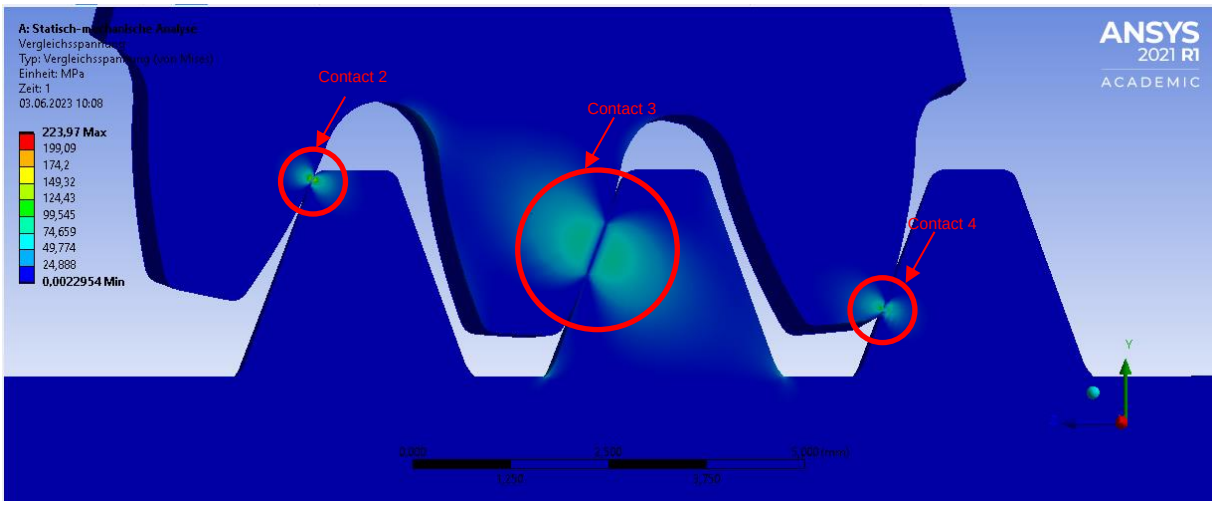


Figure 66: Snapshot of initial contact status (0º)

As can be seen in Figure 66, the initial contact status takes place with 3 active contacts. Contact 1 is not shown in the figure, because it is the one between the tooth located at the left side of contact 2 and the worm gear. Due to the big gap until this tooth enters into contact, the tooth has been eliminated, to save resources until its contact is in a nearer position.

The rotation done corresponds to a counterclockwise rotation of the top gear, meaning that contact 4 is becoming inactive and the rest of the contacts will move their contact point further down in the -Y direction.

In the snapshot shown, contact 3 is located exactly at the pitch diameter, and this will be moving downwards to the location of contact 4 while rotating the gears. This means that at the end of the cycle, contact 4 will be inactive, contact 3 will be located where contact 4 started, contact 2 where contact 3 and contact 1 that started inactive will become active and be located where contact 2 started.

Knowing this nomenclature, if Table 10 is studied again, both contacts 2 and 3 are always active during the complete rotation, contact 2 going from the top end of the tooth to the pitch diameter, and contact 3 from the pitch diameter to the bottom end of the tooth. Considering this, then a full contact motion will go from the start of contact 2 to the end of contact 3. If this is plotted in a graph representing the stress and the angle of rotation, the following curved can be observed.

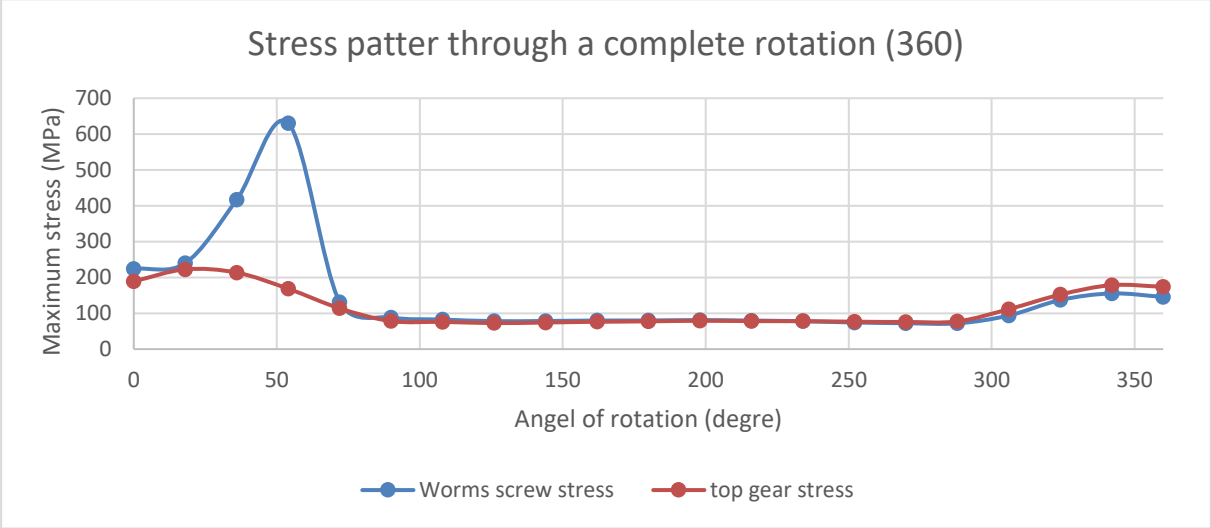


Figure 67: Stress pattern of a complete frictionless rotation

As can be seen in Figure 67, an outlier is present at the beginning of the rotation on the worm side. The stress is much bigger than the one present at the gear side and this can be caused due to mesh quality, mathematical errors during the calculation of the model or other factors, such as dynamic effects when changing from 3 teeth contact to 2 teeth contact. If those values are neglected and a similar stress as the one at the gear side is supposed, the graph will be as shown in Figure 68.

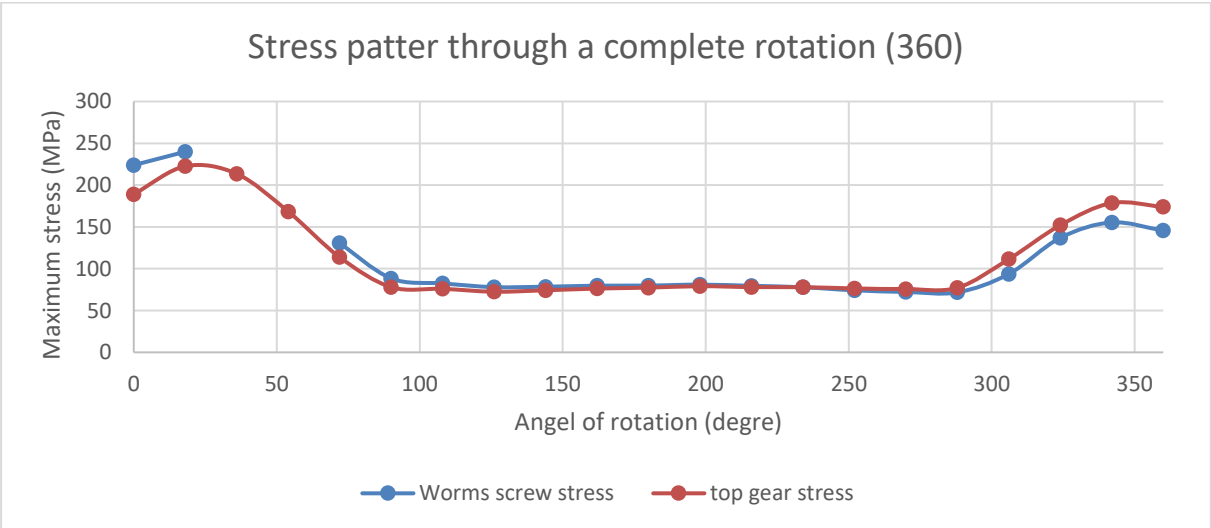


Figure 68: stress pattern neglecting outliers (frictionless)

The results show how stress, when the contact is located at the top or the bottom of the tooth, increases notably. This is due to the reduced contact area of both surfaces, transmitting the same force in a much smaller area and thus increasing the contact pressure and stress inside the bodies. It can be validated with the contact tool of ANSYS displaying the contact pressure when the contact has just become active and the one when the contact takes place at the pitch diameter. The region highlighted as "in contact" in the first case is just a very thin line with a maximum pressure of 312 MPa, while in the other case, the contact area has an ellipse shape with a much larger surface, reducing the maximum contact pressure to 134 MPa.

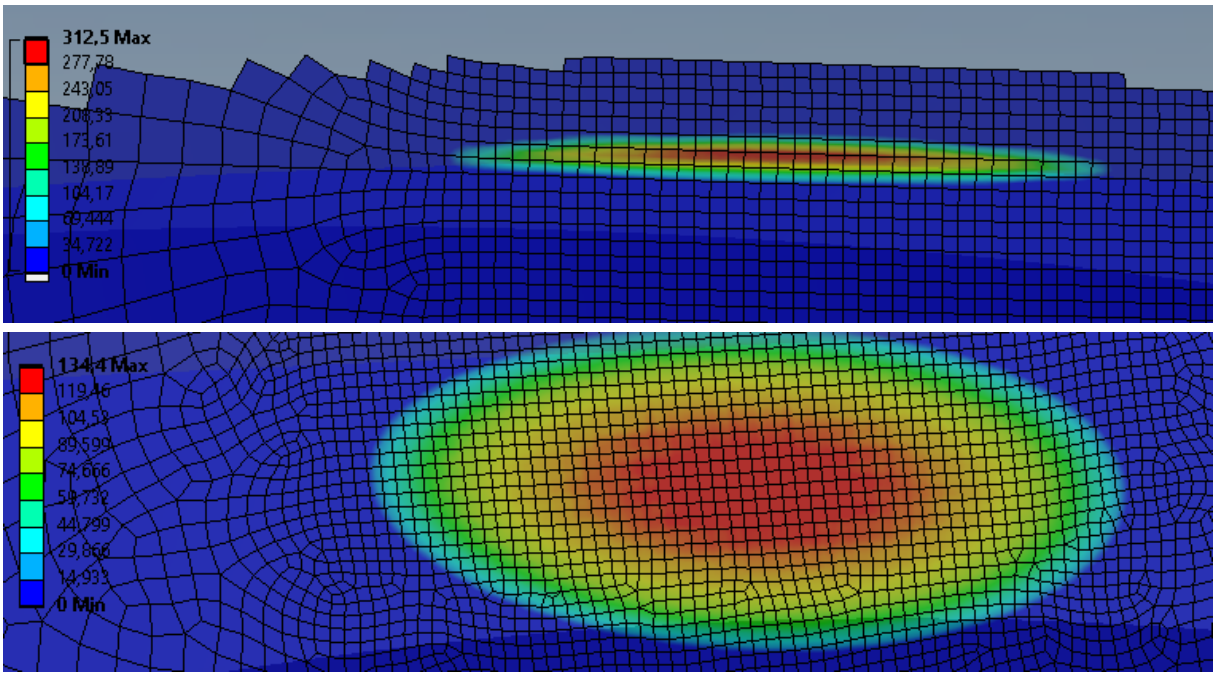


Figure 69: contact pressure at the edge of the tooth (top) vs at pitch diameter (bottom)

This must be considered when designing and testing the gear assembly because those regions, at the initial and last stages of the contact, is where the stress will be maximum and thus where the teeth could fail due to an overload and not during the "main contact" as maybe it could be supposed at the beginning of the study. This result was also validated by Dr.-Ing. Pech, as he showed in his dissertation [Pec11].

In the next part of the chapter, a more in-depth look at the contact at the pitch diameter will be exposed, analyzing the maximum pressure, the deformation of the surfaces and how the stress is distributed around its maximum point. For that, the simulation that will be evaluated is contact 3 at the 0º rotation angle.

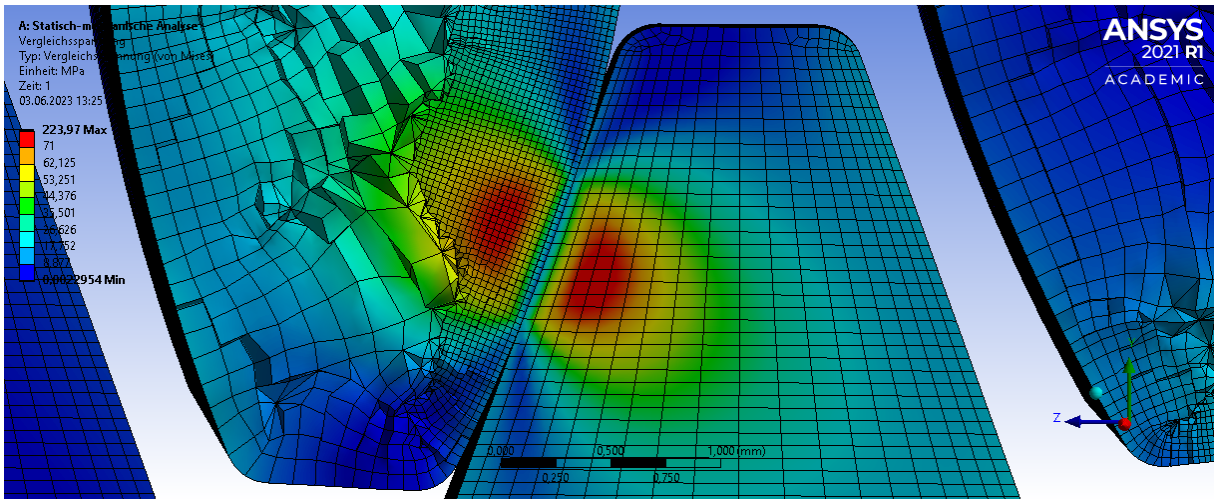


Figure 70: an overview of pitch diameter contact

As it is shown, the contact is very symmetric, having its maximum stress slightly above the surface and creating a sort of ellipse distribution around the maximum stress point that reduces progressively when getting away from the maximum stress point. This shows a very similar result as the one extracted from Wassermann's dissertation [Was05], that in case of a structural failure of the geometry, the damages will start in the internal region of the tooth instead of as superficial damage visible from the outside. Both refinements can be seen as being active and effective to calculate the maximum stress at the contact.

With regards to the shape, it can be seen that it is not a perfect ellipse, it is deformed in the loading direction perpendicular to the face where the contact is active, confirming that the load is being carried in the desired direction.

The next thing that will be examined is the deformation pattern of the contact surface, in Figure 71. As well as the stress pattern, it has an ellipse shape, having its maximum deformation at the center with a value of 15.77 µm.

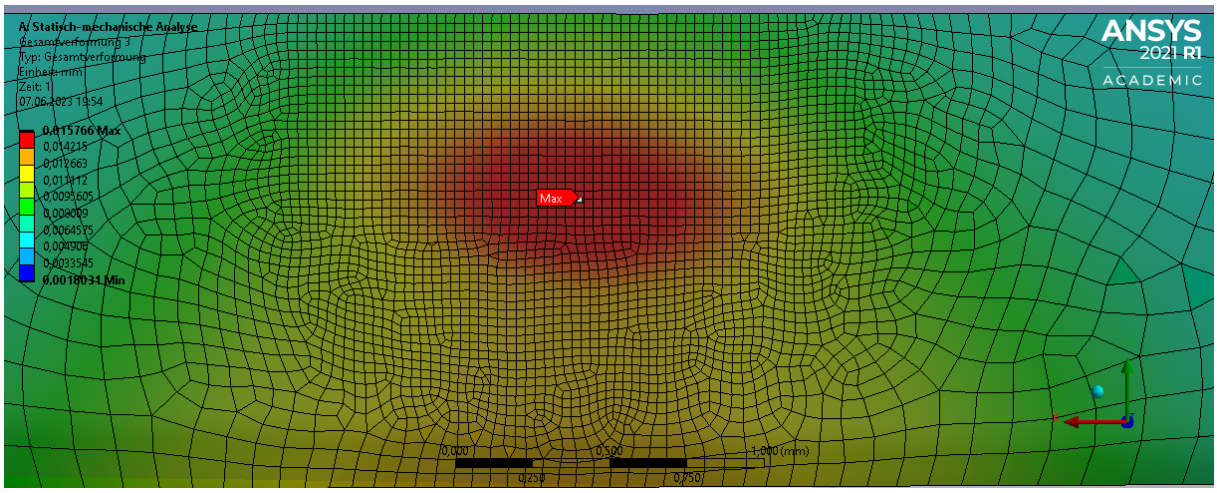


Figure 71: deformation of the contact surface in a frictionless simulation

4.7 *RESULTS (WITH FRICTION)*

In the case of a simulation with friction included in the contact, the results change slightly. First of all, the friction coefficient must be selected, in this case, as the gears are lubricated with oil, the friction coefficient is approximately 0.05, very low if it is compared with other standard friction coefficients. As can be seen in multiple articles, such as the ones from Baumann [Bau22] or Liu et al. [Liu16], in the case of lubricated or oiled gears, the friction coefficients vary depending on the load, the velocity at which the gears are rotating and other factors, due to that, a conservative value such as 0.05 can be considered for this application.

-	Teeth 1		Teeth 2		Teeth 3		Teeth 4	
Location	Screw	Gear	Screw	Gear	Screw	Gear	Screw	Gear
0	0	0	209.88	181.66	76.59	73.65	135.92	152.46
0.9	0	0	233.16	215.77	77.46	75.55	40.26	67.75
1.8	0	0	382.66	202.4	75.51	73.00	0	0
2.7	0	0	609.94	161.36	73.47	72.49	0	0
3.6	0	0	122.66	108.03	70.56	71.08	0	0
4.5	0	0	83.85	74.27	68.90	70.73	0	0
5.4	0	0	77.44	72.71	68.16	71.83	0	0
6.3	0	0	73.38	68.46	88.61	107.13	0	0
7.2	0	0	74.72	70.27	131.39	146.69	0	0
8.1	0	0	75.98	71.33	148.65	169.98	0	0
9.0	195.25	178.51	76.28	73.25	136.51	158.33	0	0

Table 11: Maximum stress in MPa for frictional contact

If the data from Table 11 is compared with the frictionless data extracted from Table 10, it can be seen a general decrease in the maximum stress value in every position and for every tooth evaluated. On average, the reduction of the maximum stress is calculated a 5% for both the gear and the worm screw side. This is due to the effect of the friction, that changes the direction of the applied force due to the tangential component of the force

introduced in the system. As now the force needs to be divided into the pressure force perpendicular to the contact surface and the frictional force tangential to the surface, the "active" part of the force contributing to the stress generation and the deformation of the surface is smaller in comparison with the simulation shown before. This can be represented in the following image extracted from the following paper by Drechsel [Dre16].

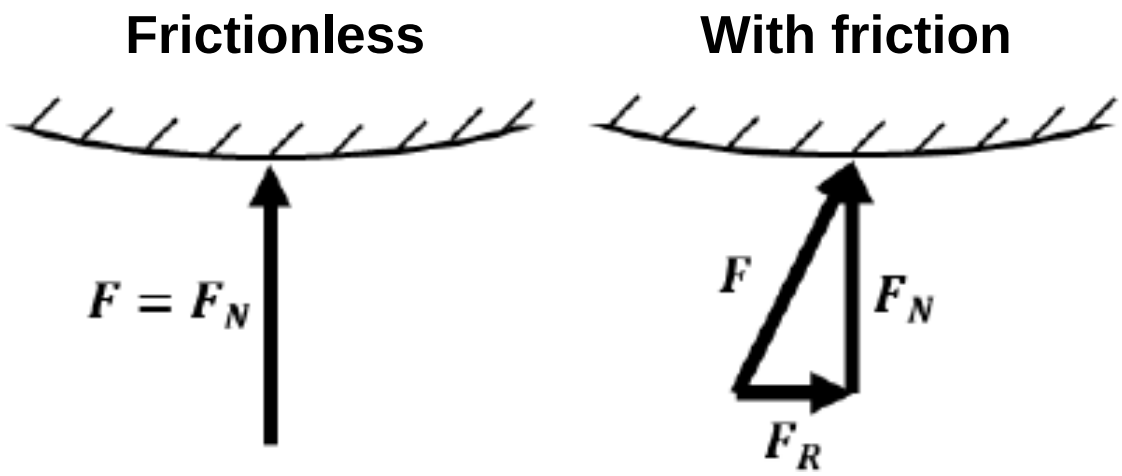


Figure 72: Schematic comparison of the contact force in a friction and frictionless simulation [Dre16].

Once this explanation has been clarified, in the following two figures, Figure 73 and Figure 74, the stress distribution of a complete frictional contact can be seen. As is exposed, the distribution of the stresses through the entire cycle shows a very similar behavior, as the one shown in the frictionless case. At the beginning and end of the contact, due to the reduced contact surface at the edge of the tooth, the stress increases slightly, while lowering and maintaining an approximate constant value during the rest of the contact cycle.

Interestingly, on the frictional simulation, the outliers are also present at the beginning of the contract cycle on the worm screw side, which should indicate that the results for those time steps should be taken with extreme caution and validated based on a real testing facility results before using them as design goals or conditions. On the second graph, where the outlier value was neglected, the frictionless simulation results are also plotted

with a dashed line to compare directly both results. As can be observed, the trend during the middle of the contact process is maintained, being the frictionless stress always a bit higher than the one with friction, but this difference increases considerably when observing the beginning and the end positions of the contract, meaning that the higher the stress value, the more difference there is between the frictionless and the frictional cases.

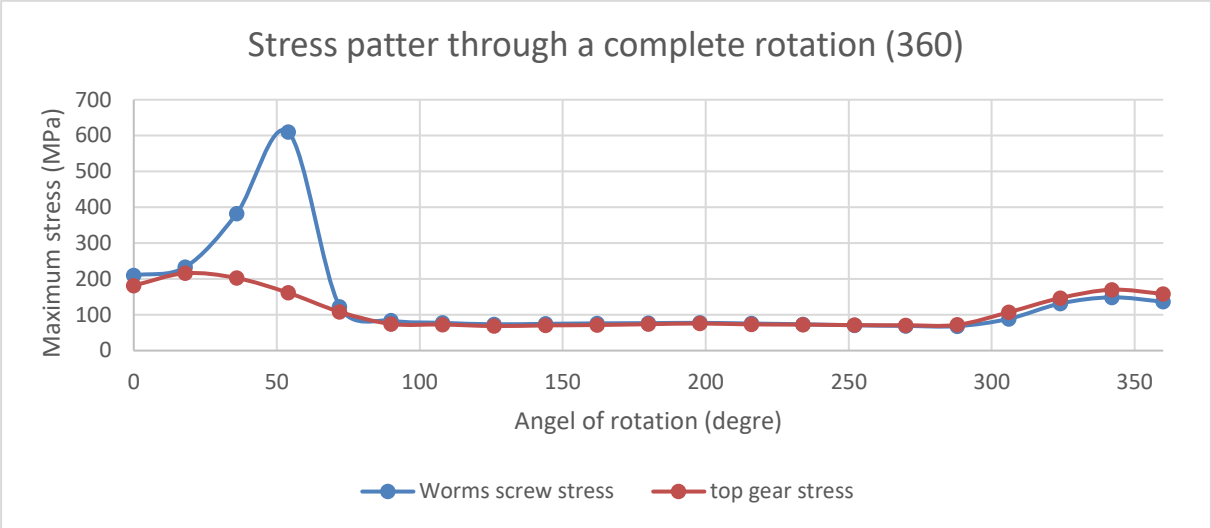


Figure 73: Stress pattern of a complete frictional rotation

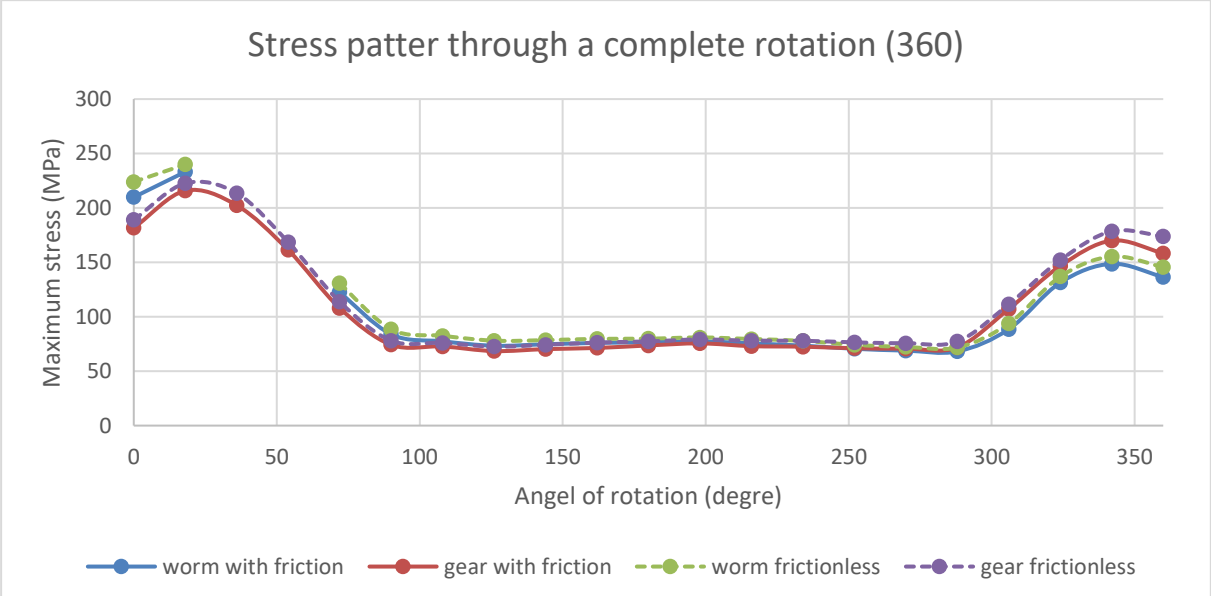


Figure 74: stress pattern neglecting outliers (frictional)

Another effect that can be detected in the frictional simulation is that the presence of a tangential force in the opposite direction of the movement generates a displacement of the stress distribution on the contact face. If both surfaces are examined as shown in Figure 75, on the frictionless distribution a more even and rounded shape can be seen, while on the frictional simulation, the regions of maximum stress are slightly displaced in the opposite direction of the movement due to this tangential force acting on the surface. As shown below, on a counterclockwise rotation, the maximum stress is displaced in the clockwise direction.

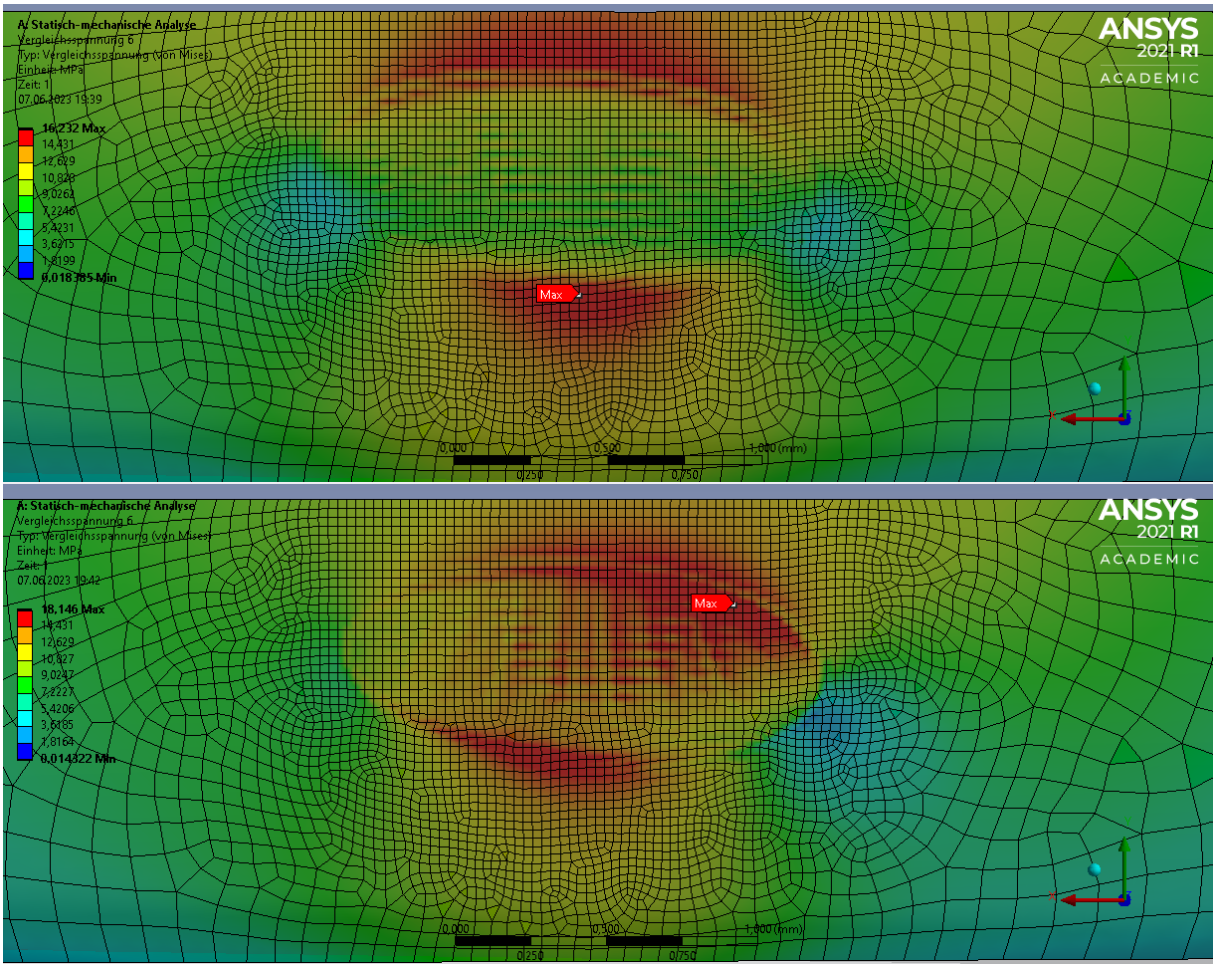


Figure 75: surface stress distribution for frictionless (top) and frictional simulation (bottom)

Lastly, in terms of displacement, the expected deformation of the contact surface should be lower than in the case of the frictionless distribution due to the less effective force pressing the contact surface caused by the frictional force. As it is displayed in Figure 76, the maximum is lower, as expected, also reducing the deformation ellipse dimensions. In this particular case, the maximum deformation has dropped from 15,766 µm to 14.297 µm, meaning a reduction of a 9.3%, doubling the percentual reduction of the maximum stresses. These values need to be also verified in the future due to the small order of magnitude of the displacements and deformations, making it possible that a numerical or mathematical modelling error leads to big deviations in comparison with the real model. Regarding the location of the maximum deformation point and the position of the ellipse axis, both stay fixed compared with the frictionless simulation, varying only the maximum deformation value.

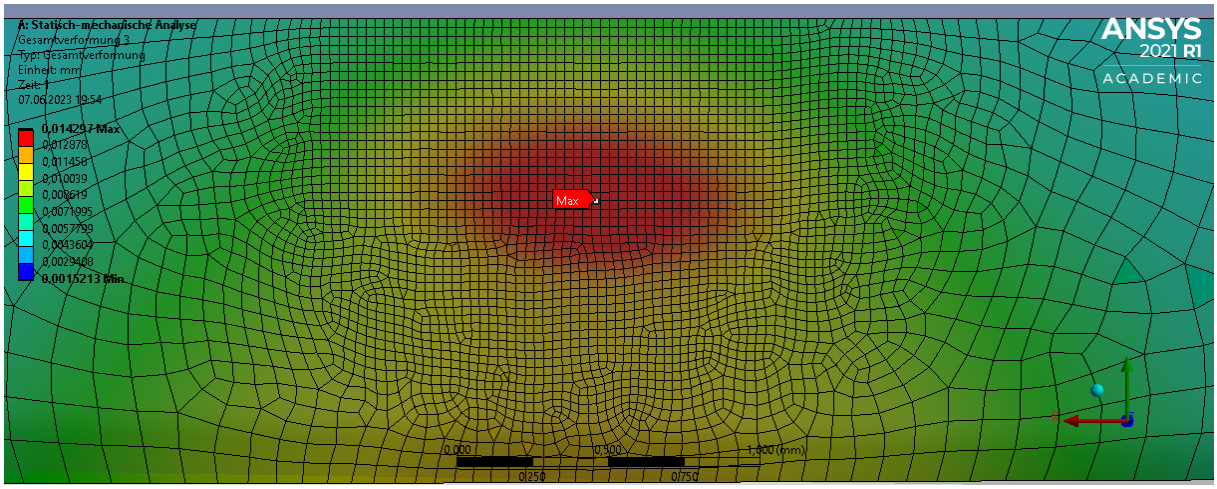


Figure 76: deformation of the contact surface in a frictional simulation

5 VALIDATION OF THE RESULTS

The last step is to consider the simulation setup as valid for its use in future experiments, a more in-depth validation of the results needs to be performed. At the moment of the study, a benchmark test of these gears is planned, but it has not been performed yet. This means that the final validation of the results will be needed to be performed as a future work following this study and these results cannot be considered valid until the bench-mark test has been performed.

Once this clarification is done, a "pre-validation" of the results can be performed. In order to do this validation, a qualitative study regarding the shape of the pressure ellipse has been studied.

To perform this validation, the first step is to calculate the shaft angle of the contact pair represented by the letter φ. Depending on that angle, the shape of the contact ellipse will vary as determined by the experiment performed and studied by Tamura et al. [Tam14] in their multiple articles such as "Contacting State on Imaginary Rack of Crossed Helical Gears" [Tam17] [NIM04].

As explained by Hofbauer in his paper [Hof18], to calculate the shaft angle, the following calculations must be performed. First of all, the shaft angle for both geometries of the gearbox needs to be calculated, and then the addition of those two values will be the total shaft angle.

$$\varphi_{1,2} = atan\left(tan(\beta_{1,2}) \cdot sin(\alpha_n)\right) \quad (13)$$

$\varphi_{1,2}$	º	Shaft angle of the contact lines	$\beta_{1,2}$	º	Helix angle on the pitch circle
α_n	º	Normal pressure angle			

$$\varphi = \varphi_1 + \varphi_2 \quad (14)$$

$\varphi_{1,2}$	º	Shaft angle of the contact lines	φ	º	Total shaft angle

For this particular case, the normal pressure angle is given in the geometry chapter, where in Table 9 the main geometric data of the assembly was gathered, being this 20º, and the same happens for the helix angle, which is in the case of the worm and the gear 82.5º and 7.5º respectively.

This data means that the total shaft angle for this application is approximately 71.5º. In the following picture extracted from [Tam17], the different geometric shapes for the contact ellipse are shown depending on the total shaft angle.

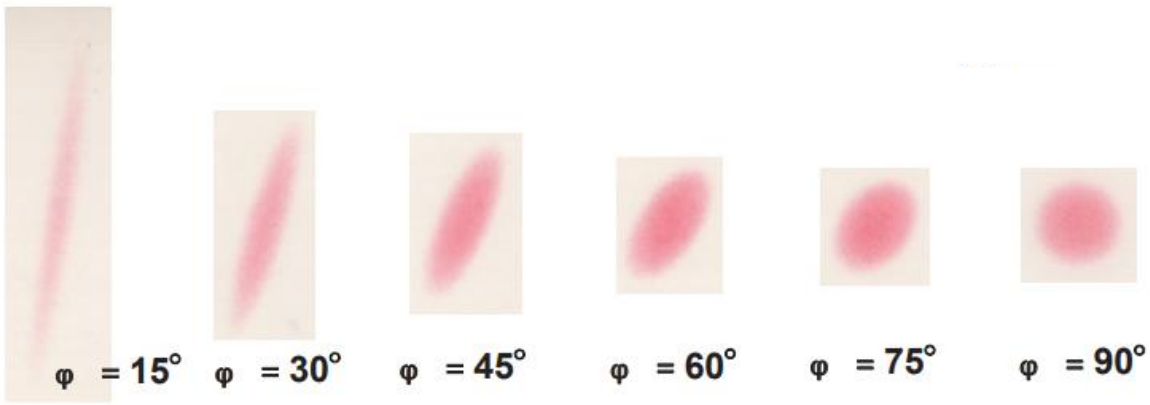


Figure 77: Geometric shape of contact ellipse depending on total shaft angle [Tam17].

In this case, the geometry that should be given by the ANSYS simulations should show a distribution between the one with 60º and the one with a 75º angle. As it is shown in Figure 78, these results match the expected experimental results extracted by Tamura.

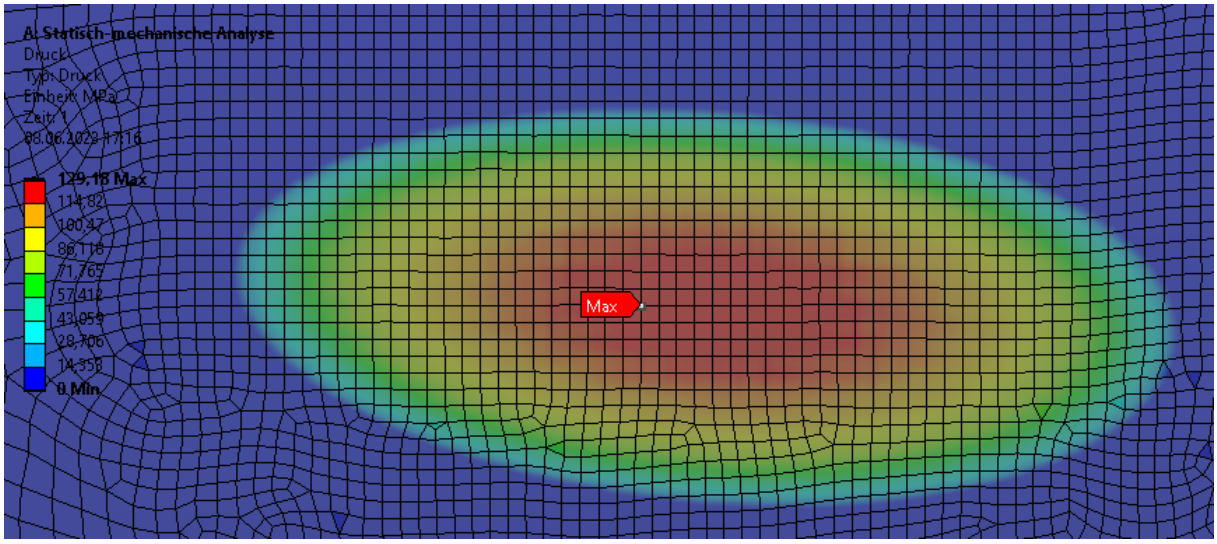


Figure 78: results of contact ellipse in frictional simulation

A second qualitative validation of the results can be performed, this time, observing the displacement of the contact ellipse during a full contact cycle. The data obtained from ANSYS can be compared with the simulated data extracted from SCHRAD2, a computational program of the Technical University of Munich created to perform these types of

simulations and used in previous studies carried out in multiple thesis performed by the university.

The main graphic that will be contrasted is the data related to the linear loads of the contact path. This is achieved by calculating the pressure during the complete contact cycle and plotting the overall maximum pressure that every point has registered during this cycle, then this pressure is multiplied by the path distance transforming it into a line load.

As ANSYS cannot plot that type of results, an approximation has been performed in order to show the contact path and the dimensions of the contact ellipse during the contact cycle. In order to perform this, a reorganization of the data with the help of MATLAB needs to be performed.

The first step is exporting the data from ANSYS, recording the coordinates of every point that constitutes the contact ellipse and saving the value of the pressure of that point. As the method used in the simulations is a quadratic method, the recorded points correspond to the nodes of the elements conforming the mesh and the middle point of its edges. Once this is achieved, it needs to be done for every tooth and every simulation step, this means that at the end there should be data from 40 contact ellipses, 4 teeth and 10 simulation steps.

Just after exporting the data, the first modification to do is a simplification and a selection of the useful contact points, this means that all of the coordinates that have a contact pressure of 0 MPa are erased to reduce the number of data and make the study of the data faster and easier.

The next step consists in translating all of the data into a one equivalent tooth. As the contact pattern evolves, the gears and its contact faces rotate and are displaced in the 3D space. As the representation aims to show the contact pattern of a tooth, every contact ellipse needs to be transformed and rotated to a reference tooth position grouping all the ellipses in a unique plane.

Once all the data is represented at the same tooth, a mathematical interpolation has been carried out, to increase the density of the evaluated points. This will allow creating a much clearer plot of the contact path, as it displays the data that is also not located exactly at the node of an element of the ANSYS mesh or at a middle point of an edge. For the density and the dimensions of the plot, the following parameters have been chosen:

	X axis	Y axis
Minimum value	-1.5 mm	-26.2 mm
Maximum value	1.5 mm	-24.2 mm
Distance between points	0.001 mm	0.001 mm

Table 12: mesh grid for interpolation of results

One last remark is that the mesh generated where the interpolation data will be plotted needs to be rectangular, and as the contact path is slightly inclined due to the movement in the 3D space of the contact point for every contact position, this creates the necessity of generating points where the interpolation will be evaluated that are considerably far from the location where the contact path is taking place, generating extremely low pressure values. Due to this, in the following graphics the scale has been set with the minimum pressure of 0 MPa (negative pressures does not make sense) and only the shapes and data of the contact path can be considered as valid, the display of the data points located far away from this path is maintained only for visual and reference purposes.

This validation of the contact path has been carried out with gears made of different materials as the one simulated previously. The first contact pair that was simulated is the Steel – PEEK pair, corresponding the first material to the worm and the second material to the gear itself, and the second material pair validated is PEEK – PEEK. Both of the simulations have been previously performed in SCHRAD2 in different thesis of the university. Regarding the boundary conditions, the input torque simulated for every case is 10 Nm at the gear side or 0.5 Nm on the worm side.

As it can be seen in Figure 79, the contact path of the Steel – PEEK pair is shown. In this case, the representation is taking place at the worm side and it was extracted form Sokolov's project [Sok22].

The figure shows a varying load, having its maximum near the outer edge of the worm. This shows the same behavior as the simulation presented in the previous chapter and it is due to the reduced contact area at that region. As the force that needs to be transmitted stays constant, but the contact area is reduced due to the location of the contact point at the edge of the tooth, this generates a peek in the pressure recorded in those points, but as it has been stated previously, the results shown in the figure correspond to line loads and not to pressure loads, so that information cannot be directly compared with the results extracted from ANSYS.

Another thing it can be observed is the movement of the contact ellipse along the plane perpendicular to the rotation axis of the worm. As the image displays, the contact ellipse moves from the outer region of the worm tooth to the inner region, but while moving at the same time to the left side. This is due to the displacement of the contact point not only across the height on the tooth, but also to the sides and causes an approximate 20° incline with respect to the vertical plane.

Regarding the width of the contact ellipse, a slight change can be observed. While at the bottom region, where the line loads are higher, the approximate width of the contact ellipse is 2.7 mm, at the opposite side of the contact, the width reduces to 2.3 mm due to the lower line loads present at that region. Finally, regarding the total height of the displacement, in the image can be measured a total ellipse displacement of 2.25 mm.

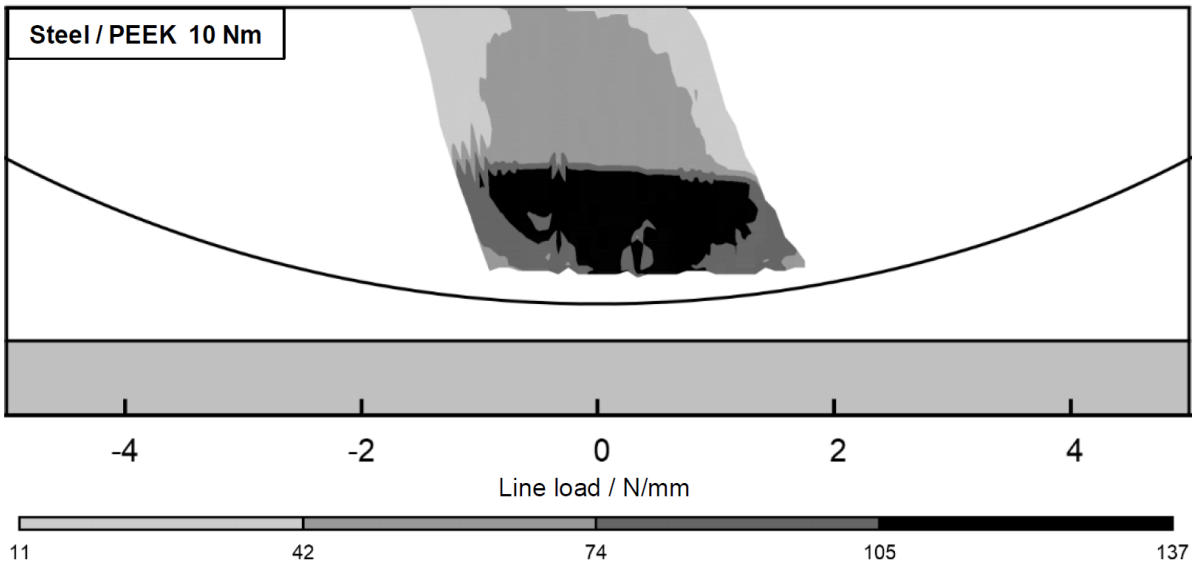


Figure 79: load contact pattern for the material combination Steel/PEEK (SCHRAD2) [Sok22].

Now, if the results from ANSYS are rearranged and plotted into a 2D space, the following image can be generated, as seen in Figure 80.

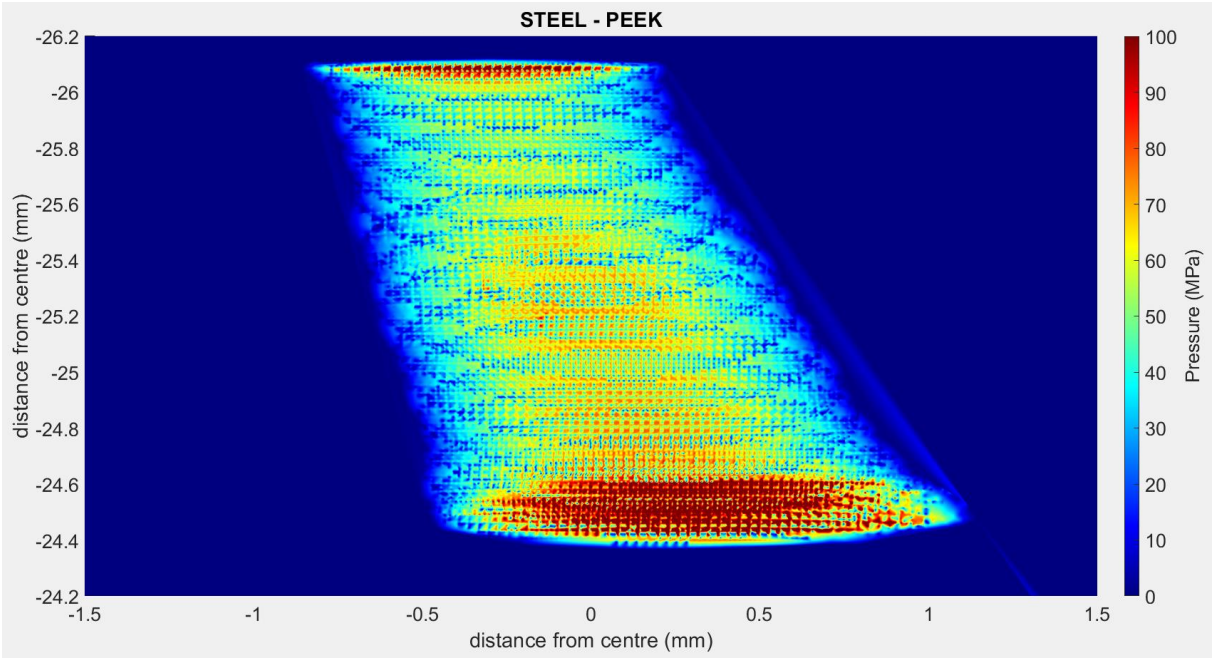


Figure 80: Steel – PEEK pressure during contact path

Here it can be seen, that as expected, the maximum pressure is located at the top and bottom of the contact path as explained earlier. The same behavior of the lateral movement of the contact ellipse is also present and maintains the 20º incline as seen previously, but in comparison with the previous data, this behavior is not symmetric, probably due to the friction considered in the simulation. On the SCHRAD2 results, the behavior is also not completely symmetric, but it is less accentuated than on the FEM results. In the case of the FEM results, a total maximum width of 1.7 mm is measured in the contact ellipse, while the minimum is only 1.1 mm. Not only the change in width is higher compared with the SCHRAD2 results, but also the ellipse width is approximately 1 mm narrower in the case of the FEM results. This must be checked once again when transforming the pressure data into linear forces to have a 1 to 1 comparison of both plots, as this trend continues also for the height of the contact path, reducing from the 2.25 mm showed by SCHRAD2 to the 1.5 mm showed in the FEM simulation.

If the second pair of materials is analyzed, in this case, the overall behavior stays the same, but with some small differences. As PEEK has a substantially lower young modulus in comparison with Steel, PEEK allows to have a largen deformation and thus reducing the stresses present in the contact path, this is observed in the Figure 81 and its values can be compared with the ones seen on Figure 79, showing in this last case a maximum line force of 109N/mm while on the Steel – PEEK pair, the maximum line load was 137 N/mm. In terms of inclination angle, the same behavior is observed, with an inclination of approximately 20º. Lastly, regarding the width of the ellipse, also the same pattern as before is observed, being the ellipse a bit wider in the bottom part of the graph with a total width of 2.8 mm and a minimum width at the top of 2.35 mm.

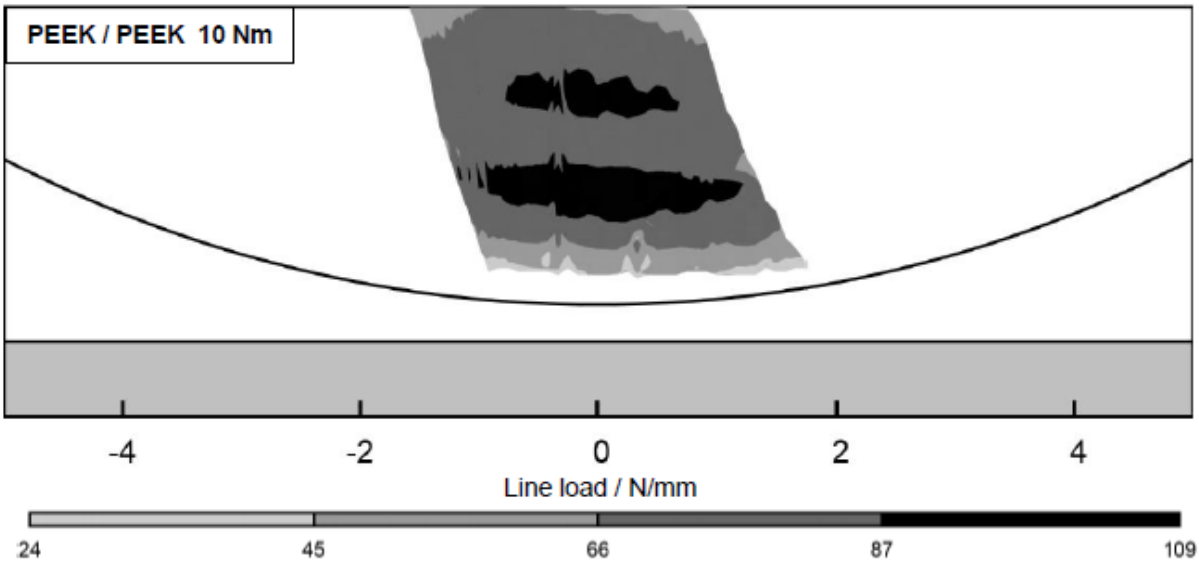


Figure 81: load contact pattern for the material combination PEEK/PEEK (SCHRAD2) [Sok22].

This same behavior is shown in the data extracted from the ANSYS simulations for this material pair. In this last case, the maximum pressure is also lower compared with the Steel – PEEK simulation and the contact path is bigger due to the higher deformations allowed by the low young modulus in both parts. The scale needed to be reduced, so that at the middle of the contact path, the increase in pressure could be appreciated. This is not as notable as in the SCHRAD 2 simulation, but it is also displayed in the FEM simulation.

Regarding ellipse dimensions, in this case, the maximum width is 2.4 mm, while the minimum width is set at 2 mm. The total height of the contact path is 1.85 mm. As it can be proved, the ellipse dimensions are higher, showing a bigger deformation and lower stresses in the contact path. Also, the differences between the FEM and the SCHRAD2 simulation are closer in this case.

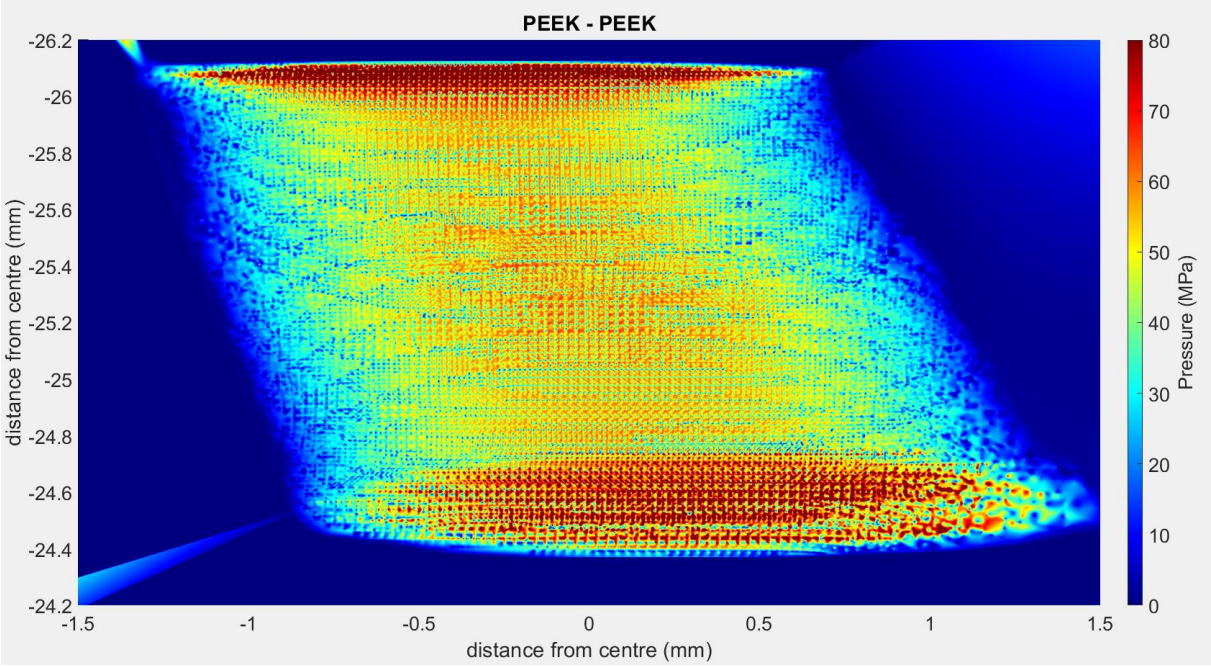


Figure 82: PEEK – PEEK pressure during contact path

To have also as a reference, in the Figure 83, the results for the reinforced PEEK material corresponding to the simulation done in Chapter 4.7 is showed, although for this material pair there is no other data available to compare the results.

As expected, as seen in the previous case, due to the higher young modulus, the contact ellipse is smaller than in the case of standard PEEK, and the stresses in the contact path are considerably higher.

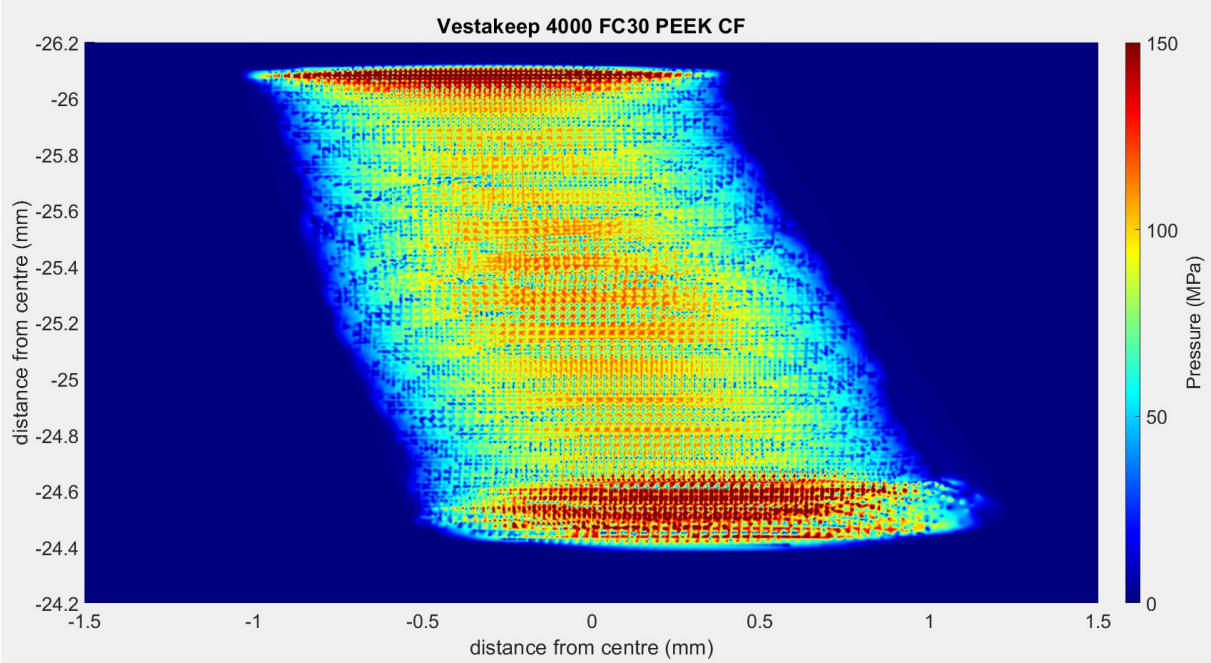


Figure 83: PEEK CF – PEEK CF pressure during contact path

6 SUSTAINABLE DEVELOPMENT GOALS

The last chapter of the thesis will be dedicated to the contribution of the thesis to the sustainable development goals. As it has been explained and developed during the thesis, the main goal is to implement the use of plastics into the fabrication and design of small gears. This will allow to make this systems cheaper due to the reduction in price of plastics in comparison with metal materials, the total weight of the system will also be reduced, minimizing the CO" emissions during the fabrication of the gears and the total life CO2 emissions during its whole life cycle and last but not least, due to the cheaper material, this systems will be more user friendly, because if a gear happens to break during operation, the substitution and replacement of it for a new one will be more affordable for the consumer.

With all of these benefits in mind, the following sustainable development goals have been chosen as goals in them this project will have an impact

6.1 *BUILD RESILIENT INFRASTRUCTURE, PROMOTE INCLUSIVE AND SUSTAINABLE INDUSTRIALIZATION AND FASTER INNOVATION [Uni23]*

Included inside this objective there are multiple goals regarding the reconstruction and development of new infrastructures and innovation for more equal development in all the countries making resources more accessible or using those resources more wisely. Here is where this project has the most impact, as the use of plastic gears, production emissions can be reduced considerably, and the secondary impact of reduced weight leads also to less fuel usage during the whole lifespan of the motor. This is enclosed in point 9.4 "By 2030, upgrade infrastructure and retrofit industries to make them sustainable, with increased resource-use efficiency and greater adoption of clean and environmentally sound technologies and industrial processes, with all countries taking action in accordance with their respective capabilities" [Uni23].

6.2 "ENSURE SUSTAINABLE CONSUMPTION AND PRODUCTION PATTERNS" [UNI23] AND NUMBER 13 "TAKE URGENT ACTION TO COMBAT CLIMATE CHANGE AND ITS IMPACTS" [UNI23].

These two objectives are more related to the reduction of emissions than to the reduction of materials or the correct usage of them, as this reduction in pollution aims to reduce climate change and preserve natural spaces. As explained in the introduction, this type of gearbox can have a huge variety of applications and could help to reduce emissions in different areas such as mobility, electric scooters and bikes, medical research with the use of these gears in motorized equipment and many more.

7 SUMMARY AND OUTLOOK

To conclude this thesis, in the following chapter a summary of the work done in this thesis with the explanations of the conclusions will be done. Additionally, a suggestion of what future works needed to be done to further develop the thesis will also be presented.

As was shown during the whole development of the thesis, a full simulation of a gearbox made of polymer material has been carried out with the intention to display the deformation and stresses suffered during its operation.

At first, the mesh sensitivity analysis was performed to determine the optimal meshing parameters that allow to achieve the maximum precision while making an optimal use of the computational resources available. This data was contrasted with the theoretical hertzian contacts results both in 2D and 3D simulations. The conclusion reached was that a minimum deviation of approximately 5% can be achieved and that the minimum refinement size that brings more precision to the results is around 0.02 mm. If a lower refinement was selected, the amount of time required to perform the simulation doesn't support the additional reduction of the error regarding the maximum pressure value.

Once these parameters have been determined, the mesh for the simulation of the gearbox of interest was created with the required refinement regions and sizes. To perform the simulation, it was divided into 10 steps, each one performing a 0.9º rotation to achieve a total 9º rotation equivalent to the displacement of 1 tooth to the next contact position.

The extracted results were mainly the pressure and the deformation of the contact faces of the respectively teeth in contact and two main simulation conditions were tested, the first one without friction and the second one with a low friction coefficient of 0.05 simulating the oiled contact.

When evaluating the results, the following conclusions were reached. The first conclusion was that at the top and bottom of the contact, this means when the contact point is located

at the top the worm teeth and at the bottom of the gear tooth, and the other way around, worm tooth's top and gear tooth's bottom, the pressures registered where considerably higher than the ones recorded during the rest of the contact due to the reduced contact area.

The next observation is that during almost all of the contact, only two teeth are in contact at the same time, causing that during the contact path, no peaks of pressure are registered and the changes in pressure follow a smooth curve.

The comparison between the frictionless and the simulation with friction showed that in the case of the simulation where the friction was taken into account, the pressure registered was lower than in the frictionless cases. This was considered to be occasioned by the tangential force responsible for the friction, reducing the perpendicular or effective force applied at the contact surface. This was the case during the whole contact path.

Regarding the validation of the results, as a real-life test of this material has not been performed yet, there is no real data available to validate the results and the only option is to compare it with other simulated data.

In this case, the first simulations were regarding the contact ellipse shape and orientation when the contact point was located exactly at the middle of the contact path, showing that the qualitative shape and deformation pattern goes in accordance with the data obtained by other studies of similar topics.

Another qualitative validation of the results was made, in this case, based on the simulations done by the machine elements department of the Technical University of Munich, but for different material pairs, like Steel – PEEK and PEEK – PEEK.

As was explained in the previous chapter, the simulation results must be validated with real benchmark testing through loading testing, and they must not be considered valid until this test is performed. Once this testing has been carried out, some other achievements need to be performed as future works for the project are the following.

- Validate results with benchmark testing.
- Perform transient simulation to simulate with enough precision a complete rotation cycle.
- Increase simulation span to fixing elements and testing casing assembly.
- Extrapolate setup adjustments to other gear types and geometries.
- Reduce the simulation step in case of static simulation to obtain more precise results with a smaller rotation interval between them.
- Transform pressure data into linear loads to make a quantitative validation with the simulated data obtained by the SCHRAD2 software.

8 BIBLIOGRAPHY

Journal articles, books, dissertations, student research projects

[Alt20] Altenbach, H.; Öchsner, A.: FEM. Castro; Altenbach. Encyclopedia of Continuum Mechanics, Berlin, Heidelberg (2020).

[Ans01] Ansi: Materials for plastic gears. American Gear Manufacturers Association, Alexandria, Va. (2001).

[Asc14] Aschendorf: FEM bei elektrischen Antrieben 1. Springer Fachmedien Wiesbaden, Wiesbaden (2014).

[Bar18] Barber, J. R.: Contact Mechanics. Springer, New York NY, 1. Auflage (2018).

[Bau22] Baumann, A.; Bertsche, B.: Coefficient of friction behavior of gear oils and significance for the meshing process of spur gears. Forschung im Ingenieurwesen 86. Heft: 4, S. 795–805 (2022).

[Car19] Carrozza, M. C.; Micera, S.; Pons, J. L.: Wearable Robotics: Challenges and Trends - Proceedings of the 4th International Symposium on Wearable Robotics, WeRob2018, October 16-20, 2018, Pisa, Italy, Cham (2019).

[Cas20] Castro; Altenbach: Encyclopedia of Continuum Mechanics, Berlin, Heidelberg (2020).

[Cri19] Crispel, S.; García, P. L.; Verstraten, T.; Convens, B.; Saerens, E.; Vanderborght, B.; Lefeber, D.: Introducing Compound Planetary Gears (C-PGTs): A Compact Way to Achieve High Gear Ratios for Wearable Robots. Carrozza, M. C.; Micera, S.; Pons, J. L. Wearable Robotics: Challenges and Trends. Proceedings of the 4th International Symposium on Wearable Robotics, WeRob2018, October 16-20, 2018, Pisa, Italy, Cham (2019).

[Dre16] Drechsel, A.: Analyse der Verformung des Zahnkontaktes von Schraubradgetrieben unter Verwendung der Finite Element Methode, Technical University of Munich, Garching, München (2016).

[Ehr11] Ehrenstein, G. W.: Polymer Werkstoffe - Struktur Eigenschaften Anwendung. Hanser Verlag, München, 3. Auflage (2011).

[Els12] Elsevier: International Journal of Solids and Structures (2012).

[Erh78] Erhard, G.; Strickle, E.: Maschinenelemente aus thermoplastischen Kunststoffen. VDI-Verlag, Düsseldorf (1978).

[Err13] Errichello, R.: Spur Gears. Wang, Q. J.; Chung, Y. Encyclopedia of Tribology, Boston, MA (2013).

[Fri93] Fritscher, T.: Fem-praxis mit ansys - Grundkurs. Friedrick Vieweg & Son, [Place of publication not identified] (1993).

[Frü12] Frühe, T.: Berechnung und Minimierung der Zahnfußspannung von Standard- und LowLoss-Verzahnungen, Technical University of Munich (2012).

[Für13] Fürstenberg, M. D.: Betriebsverhalten verlustoptimierter Kunststoffzahnräder, Disertation, Technical University of Munich (2013).

[God22a] Godec, D.; Gonzalez-Gutierrez, J.; Nordin, A.; Pei, E.; Ureña Alcázar, J.: GUIDE TO ADDITIVE MANUFACTURING, [S.l.] (2022).

[God22b] Godec, D.; Pilipović, A.; Breški, T.; Ureña, J.; Jordá, O.; Martínez, M.; Gonzalez-Gutierrez, J.; Schuschnigg, S.; Blasco, J. R.; Portolés, L.: Introduction to Additive Manufacturing. Godec, D., et al. GUIDE TO ADDITIVE MANUFACTURING, [S.l.] (2022).

[Gre21] Grellmann, W.; Seidler, S.: Polymer testing. Hanser Publications, Cincinnati, 3rd (2021).

[Has18] Hasl, C.: Zur Zahnfußtragfähigkeit von Kunststoffstirnrädern, Disertation, Technical University of Munich (2018).

[Her96] Hertz, H.: Miscellaneous Papers. MacMillan and Co., London, UK (1896).

[Het14] Hetnarski, R. B.: Finite Element Method. Hetnarski, R. B. Encyclopedia of thermal stresses, Dordrecht (2014).

[Hof18] Hofbauer, J.: Analyse der lokalen Lastverteilung von Schraubradverzahnungen, Technical University of Munich, München (2018).

[Kat22] Kathiresh, M.; Kanagachidambaresan, G. R.; Williamson, S. S.: E-Mobility: A New Era in Automotive Technology - A new era in automotive technology. Springer, Cham, Switzerland, 1. Auflage (2022).

[Kle00] Klein, B.: FEM - Grundlagen und Anwendungen der Finite-Elemente-Methode ; mit 12 Fallstudien und 16 Übungsaufgaben. Vieweg, Braunschweig, Wiesbaden, 4., verb. und erw. Aufl. (2000).

[Kli08] Klingelnberg; Brecher, C.; Hohn, B.; Klingelnberg, J.: Kegelräder. Springer Berlin Heidelberg (2008).

[Kur03] Kurokawa, M.; Uchiyama, Y.; Iwai, T.; Nagai, S.: Performance of Plastic Gear Made of Carbon Fiber Reinforced Polyamide. Wear (2003).

[Liu16] Liu, H.; Zhu, C.; Sun, Z.; Zhang, Y.; Song, C.: Coefficient of friction of a starved lubricated spur gear pair. Journal of Mechanical Science and Technology 30. Heft: 5, S. 2171–2177 (2016).

[Man22] Mandt, D.; Hessel, C.; Klopp, K.; Lange, S.: Kohlenstofffaserverstärkte Kunststoffzahnräder für den Einsatz in Leistungsgetrieben, Frankfurt am Main (2022).

[Moa13] Moaveni, S.: Finite Element Analysis Theory and Application with ANSYS, Internation. Pearson Education, Harlow, 4 ed. (2013).

[Nie11] Niemann, G.; Neumann, B.; Winter, H.: Maschinenelemente - Band 3: Schraubrad-, Kegelrad-, Schnecken-, Ketten-, Riemen-, Reibradgetriebe, Kupplungen, Bremsen, Freiläufe. Springer Berlin Heidelberg, Berlin, 2nd ed. (2011).

[Nie03] Niemann, G.; Winter, H.: Maschinenelemente - Band 2: Getriebe allgemein, Zahnradgetriebe -- Grundlagen, Stirnradgetriebe. Springer Berlin Heidelberg, Berlin, Heidelberg, Zweite, völlig neubearbeitete Auflage (2003).

[NIM04] NIMOTO, R.; TANAKA, E.; Takahasi, H.: Contact Stress State of Crossed Helical Gears. The proceedings of the JSME annual meeting 2004.4. Heft: 0, S. 271–272 (2004).

[Pec11] Pech, M. Dipl.-Ing.: Tragfähigkeit und Zahnverformung von Schraubradgetrieben der Werkstoffpaarung Stahl/Kunststoff, Ruhr-Universität Bochum, Bochum (2011).

[PID17] PIDAPARTI, R.: ENGINEERING FINITE ELEMENT ANALYSIS. SPRINGER INTERNATIONAL PU, [S.l.] (2017).

[Rad22] Radzevich: Recent Advances in Gearing - Scientific theory and applications. Springer International Publishing, [S.l.], 1st ed. (2022).

[Sok22] Sokolov, V.: Study on calculation approaches for the determination of the load carrying capacity of crossed helical gears made of polymers, Technical University of Munich, München (2022).

[Son21] Song, K.; Xiao, G.; Chen, S.; Li, S.: Analysis of thermal-mechanical causes of abrasive belt grinding for titanium alloy. The International Journal of Advanced Manufacturing Technology 113. Heft: 11-12, S. 3241–3260 (2021).

[Sto12] Stommel, M.; Stojek, M.; Korte, W.: FEM zur Berechnung von Kunststoff- und Elastomerbauteilen. Hanser, München (2012).

[Sug21] Sugunesh, A. P.; Mertens, A. J.: 2D FEA study of Hertzian contact stress between two cylindrical bodies. Materials Today: Proceedings 44, S. 4474–4478 (2021).

[Tam17] Tamura, E.; Nemoto, R.; Seyama, N.; Tanaka, E.: Contact Stress State of Crossed Helical Gears, Aachen, Germany (2017).

[Tam14] Tamuta, E.; Nemoto, R.; Tomita, E.; Takahashi, H.: Contacting State on Imaginary Rack of Crossed Helical Gears, Tokyo Metropolitan College Industry Technology, Pilsen, Czech Republic (2014).

[Tay16] Taylor, B.: Tutorial - Hertz Contact Stress (2016).

[Ver16]: Thermoplastic gear wheels Materials, material selection, production methods, production tolerances, form design (2016).

[VUL21] VULLO, V.: GEARS - Volume 2. SPRINGER NATURE, [S.l.] (2021).

[Wan13a] Wang, Q. J.; Chung, Y.: Encyclopedia of tribology - With 3650 figures and 493 tablets. SpringerReference, New York (2013).

[Wan13b] Wang, Q. J.; Zhu, D.: Hertz Theory: Contact of Spherical Surfaces. Wang, Q. J.; Chung, Y. Encyclopedia of Tribology, Boston, MA (2013).

[Wan12] Wang, Z.; Jin, X.; M. Keer, L.; Wang, Q.: Numerical methods for contact between two joined quarter spaces and a rigid sphere. Elsevier. International Journal of Solids and Structures (2012).

[Was05] Wassermann, J. Dipl.-Ing.: Einflussgrößen auf die Tragfähigkeit von Schraubradgetrieben der Werkstoffpaarung Stahl / Kunststoff, Ruhr-Universität Bochum, Bochum (2005).

[Whi17] Whiteley, J.: Finite Element Methods - A Practical Guide. Springer International Publishing; Imprint: Springer, Cham, 1st ed. 2017 (2017).

[Zhu12] Zhu, X.: Tutorial on Hertz Contact Stress (2012).

Internet pages

[Aut17] Auto Simple: Manual Transmission 101: How to Drive a Stick Shift. URL: https://www.autosimple.com/blog/how-to-drive-stick-shift/#:~:text=Manual%20cars%20have%20up%20to,R%E2%80%9D%20for%20%E2%80%9Creverse.%E2%80%9D. Abrufdatum 24.05.2023.

[Bos23] Bosch eBike Systems: Active line: the harmonious Bosch motor for electric bikes. URL: https://www.bosch-ebike.com/en/products/active-line.

[Col19] Collins, L.: The Evolution of Transmissions. URL: https://www.transmissionsolympia.com/the-evolution-of-transmissions/.

[DSM23] DSM: Delivering plastic gears optimized for e-bike drive units. URL: https://www.dsm.com/engineering-materials/en_US/insights/blog/delivering-plastic-gears-optimized-for-e-bike-drive-units.html.

[Hor20] Horizon Technology: Automotive powertrain design. URL: https://www.horizon-technology.biz/blog/automotive-powertrain-design-torque-considerations-trends.

[Kin20] Kinnaird, C.: How many electric motors are in your car? URL: https://e2e.ti.com/blogs_/b/behind_the_wheel/posts/how-many-electric-motors-are-in-your-car#:~:text=So%20how%20many%20electric%20motors,40%20electric%20motors%20or%20more. Abrufdatum 13.04.2023.

[Lay14] Layosa, C.: 5 Common Gear Types. URL: https://us.misumi-ec.com/blog/5-different-types-of-gears-their-applications/.

[Les23] Lesics: Understanding planetary engagement systems. URL: https://www.youtube.com/watch?v=ARd-Om2VyiE&ab_channel=Lesics.

[Nic22] Nice, K.; Hall-Geisler, K.: How Gears Work. URL: https://science.howstuffworks.com/transport/engines-equipment/gear.htm#pt2.

[Pul23] Pullen, K.: What Is A Planetary Gear? URL: https://www.rexnord.com/blog/articles/gear/what-is-a-planetary-

gear#:~:text=Planetary%20gear%20de-signs%20are%20used%20in%20a%20wide,uses%20planetary%20gear-ing%20to%20power%20the%20shifting%20mechanism.

[San23] Santram Engineers: Pros & Cons of Worm Gear and Bevel Gear. URL: https://www.santramengineers.com/pros-cons-of-worm-gear-and-bevel-gear/.

[tec18] tec-science: How does a gearbox (transmission) work? URL: https://www.tec-science.com/mechanical-power-transmission/basics/operating-principle/.

[Wik23] Wikipedia: Automatic Transmission. URL: https://en.wikipedia.org/wiki/Automatic_transmission.

Other

[ANS21] ANSYS Inc.: ANSYS Mechanical Users Guide (2021).

[Das15] Dassault Systems Solidworks Corp.: Introduction to Solidworks, Waltham, MA (2015).

[EEU] EEUU Parliament: legislative proposal for a revision of the CO2 emission performance standards.

[Gig20] Giglmaier, M. Dr.-Ing.: Applied CFD subject, Technical University of Munich (2020).

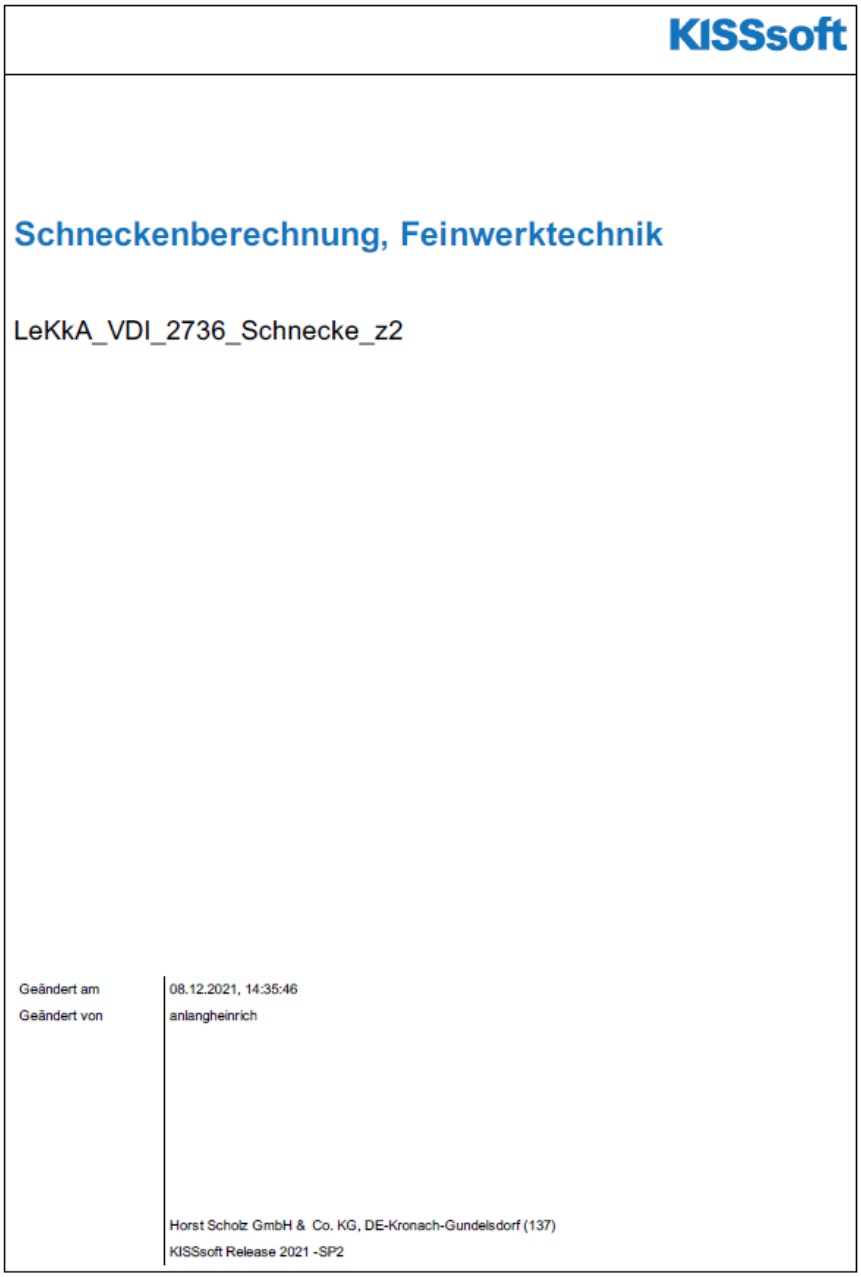
[KIS23] KISSsoft AG: KISSsoft users manual (2023).

[U.S11] U.S. Energy Information Administration: Annual Energy Outlook 2011 with projections to 2035, U.S. Energy Information Administration (2011).

[Wud21] Wudy, K. Prof. Dr.-Ing.: Additive Manufacturing with Plastics (TUM Lecture), Technical University of Munich (2021).

9 ANNEX

9.1 MATERIAL PROPERTIES AND GEOMETRIC DATA OF THE SIMULATED GEAR



KISSsoft

Schneckenberechnung, Feinwerktechnik

LeKkA_VDI_2736_Schnecke_z2

Geändert am	08.12.2021, 14:35:46
Geändert von	anlangheinrich

Horst Scholz GmbH & Co. KG, DE-Kronach-Gundelsdorf (137)
KISSsoft Release 2021 -SP2

KISSsoft

Inhalt

1	**Meldungen**	3
2	**Übersicht**	3
3	**Zahngeometrie und Werkstoff**	4
3.1	Werkstoff	4
3.2	Bezugsprofile	4
3.3	Schmierung	5
3.4	Zahngeometrie	5
4	**Allgemeine Einflussfaktoren**	6
5	**Entwurfsberechnung**	7
6	**Zahnflankentragfähigkeit**	7
7	**Zahnfuss-Tragfähigkeit**	7
8	**Prüfmasse für die Zahndicke**	8
9	**Verzahnungstoleranzen**	8
10	**Ergänzende Daten**	9
11	**Zahnformbestimmung**	9
11.1	Daten zur Zahnformberechnung	9
12	**Lebensdauer, Schädigung**	10
13	**Bemerkungen**	10

KISSsoft

1 Meldungen

Es sind während der Berechnung Meldungen aufgetreten:

Die eingegebenen Zahnraddaten erfüllen die Einschränkungen der Rechenmethode nicht!

Für die Anwendung der VDI 2736 gelten folgende Einschränkungen:
- Stahl/Kunststoff-Kombination
- Zähnezahl z1 < 6
- Normalmodul >= 0.30 mm
- Achswinkel = 90°

Rad 1:
Das Fusskreisabmass ist viel zu gross!

Rad 2:
Das Fusskreisabmass ist viel zu gross!

Rad 1:
Daten für die Bestimmung des Werkstoffkennwertes Zahnflanke [sigHlim]:
Keine Daten verfügbar bei Temperatur 70 °C
(oder Daten nicht vorhanden).

Rad 2:
Daten für die Bestimmung des Werkstoffkennwertes Zahnflanke [sigHlim]:
Keine Daten verfügbar bei Temperatur 70 °C
(oder Daten nicht vorhanden).

Rad 1:
Daten für die Bestimmung des Werkstoffkennwertes Zahnfuss [tauFadm]:
Keine Daten verfügbar bei Temperatur 70 °C
(oder Daten nicht vorhanden).

Werkstoff: Vestakeep 4000 FC30 PEEK CF
Daten für die Zahnfuss-Dauerfestigkeitsberechnung sind
für diesen Werkstoff nicht vorhanden (in Datei: Vestakeep_4000_Erlangen.DAT).

Hinweis:
Daten für eine statische Berechnung sind verfügbar.
Sie können damit die 'Statische Berechnung' durchführen.

Rad 2:
Daten für die Bestimmung des Werkstoffkennwertes Zahnfuss [tauFadm]:
Keine Daten verfügbar bei Temperatur 70 °C
(oder Daten nicht vorhanden).

2 Übersicht

Rechenmethode:		Kunststoff nach VDI 2736:2013 (YF Methode C)	
Zeichnungs- oder Artikelnummer:			
Rad 1:		0.000.0	
Rad 2:		0.000.0	
		------- Schnecke	---------- Schneckenrad ----
Leistung (W)	[P]	196.350	
Leistung (W)	[P]	277.578	196.350
Drehzahl (1/min)	[n]	3000.0	150.0
Drehmoment (Nmm)	[T]	883.558	12500.000
Anwendungsfaktor	[KA]	1.00	
Geforderte Lebensdauer	[H]	111.11	

3/10

KISSsoft

Rad treibend (+) / getrieben (-) + -

3 Zahngeometrie und Werkstoff

		------- Schnecke	---------- Schneckenrad ----
Achsabstand (mm)	[a]	34.784	
Achsabstandsabmass (mm)	[Aa.e/i]	0.020	-0.020
Achswinkel (°)	[Σ]	90.0000	
Normalmodul (mm)	[mn]	1.2500	
Normalmodul im Schraubkreis (mm)	[msn]	1.2500	
Schrägungswinkel am Teilkreis (°)	[β]	82.4930	7.5070
Schrägungsrichtung	[L/Rβ1]	rechts	
Schrägungsrichtung	[L/Rβ2]		rechts
Normaleingriffswinkel (°)	[αn]	20.0000	
Steigungswinkel am Teilkreis (°)	[γ]	7.5070	82.4930
Schrägungswinkel am Schraubkreis (°)	[βs]	82.4930	7.5070
Zähnezahl	[z]	2	40
Flankenform:		ZI	
Zahnbreite (mm)	[b]	75.00	10.00
Zahnbreite für Rechnung (mm)	[beH]	3.32	3.32
Verzahnungsqualität	[Q-DIN ISO 1328:2018]	A10	A10
Innendurchmesser (mm)	[di]	10.00	10.00
Innendurchmesser der Bandage (mm)	[dbi]	0.00	0.00

3.1 Werkstoff

Schnecke
Vestakeep 4000 FC30 PEEK CF, Thermoplast (POM, PPA, etc.), faserverstärkt
[S B Wd] PEEK, CF, PTFE, Graphite, by Evonik
Rad 2
Vestakeep 4000 FC30 PEEK CF, Thermoplast (POM, PPA, etc.), faserverstärkt
[S B Wd] PEEK, CF, PTFE, Graphite, by Evonik

		------- Schnecke	--------- Schneckenrad ----
Zahnfuss-Temperatur (°C)	[TR]	70.0	70.0
Flankentemperatur (°C)	[TF]	70.0	70.0
Bruchfestigkeit (N/mm²)	[σB]	120.15	120.15
Streckgrenze (N/mm²)	[σS]	76.83	76.83
Elastizitätsmodul (N/mm²)	[E]	10075	10075
Poissonzahl	[v]	0.440	0.440
Mittenrauhwert Ra, Flanke (µm)	[RAH]	0.00	0.00
Mittenrauhwert Ra, Fuss (µm)	[RAF]	0.00	0.00
Gemittelte Rauhtiefe Rz, Flanke (µm)	[RZH]	0.00	0.00
Gemittelte Rauhtiefe Rz, Fuss (µm)	[RZF]	0.00	0.00

3.2 Bezugsprofile

Bezugsprofil von Rad 1:
Bezugsprofil, Eigene Eingabe

Fusshöhenfaktor	[hfP*]	1.250	
Fussradiusfaktor	[ρfP*]	0.471	(ρfPmax*= 0.472)
Kopfhöhenfaktor	[haP*]	1.000	
Kopfradiusfaktor	[ρaP*]	0.000	
Protuberanzhöhenfaktor	[hprP*]	0.000	
Protuberanzwinkel	[αprP]	0.000	

4/10

KISSsoft

Kopfformhöhenfaktor	[hFaP*]	0.000		
Kantenbrechflankenwinkel	[cKP]	0.000		
	nicht überschneidend			
Bezugsprofil von Rad 2:				
Bezugsprofil, Eigene Eingabe				
Fusshöhenfaktor	[hfP*]	1.250		
Fussradiusfaktor	[ρfP*]	0.471	(ρfPmax*= 0.472)	
Kopfhöhenfaktor	[haP*]	1.000		
Kopfradiusfaktor	[ρaP*]	0.000		
Protuberanzhöhenfaktor	[hprP*]	0.000		
Protuberanzwinkel	[αprP]	0.000		
Kopfformhöhenfaktor	[hFaP*]	0.000		
Kantenbrechflankenwinkel	[cKP]	0.000		
	nicht überschneidend			

3.2.1 Angaben für die Fertigbearbeitung

Fusshöhe Bezugsprofil	[hfP*]	1.250	1.250
Fussradius Bezugsprofil	[ρfP*]	0.471	0.471
Kopfhöhe Bezugsprofil	[haP*]	1.000	1.000
Protuberanzhöhenfaktor	[hprP*]	0.000	0.000
Protuberanzwinkel (°)	[αprP]	0.000	0.000
Kopfformhöhenfaktor	[hFaP*]	0.000	0.000
Kantenbrechflankenwinkel (°)	[cKP]	0.000	0.000
Art der Profilkorrektur:	keine (nur Einlaufbetrag)		
Kopfrücknahme, durch Einlaufen (µm)	[Ca L/R]	20.4 /20.4	20.4 /20.4

3.3 Schmierung

Schmierungsart	Öl-Tauchschmierung	
Ölsorte	ISO-VG 46	
Schmierstoff-Basis	Mineralöl-Basis	
Kinematische Nennviskosität Öl bei 40°C (mm²/s)	[v40]	46.00
Kinematische Nennviskosität Öl bei 100°C (mm²/s)	[v100]	6.70
Spezifische Dichte bei 15°C (kg/dm³)	[ρ]	0.880
Öltemperatur (°C)	[TS]	70.000

3.4 Zahngeometrie

		------- Schnecke	---------- Schneckenrad ----
Gesamtübersetzung	[itot]	-20.000	
Zähnezahlverhältnis	[u]	20.000	
Stirnmodul (mm)	[mt]	9.5677	1.2608
Axialmodul (mm)	[mx]	1.2608	9.5677
Normaleingriffswinkel am Schraubkreis (°)	[αsn]	20.000	20.000
Stirneingriffswinkel am Schraubkreis (°)	[αst]	70.254	20.159
Axialeingriffswinkel am Schraubkreis (°)	[αsx]	20.159	70.255
Stirneingriffswinkel (°)	[αt]	70.254	20.159
Axialeingriffswinkel (°)	[αx]	20.159	70.254
Grundschrägungswinkel (°)	[βb]	68.692	7.052
Formzahl q	[q]	15.177	
Nullachsabstand (mm)	[ad]	34.784	
Profilverschiebungsfaktorsumme	[Σxi]	-0.0000	
Profilverschiebungsfaktor	[x]	-0.0000	-0.0000
Kopfhöhenänderung (mm)	[k*mn]	0.000	0.000
Teilkreisdurchmesser (mm)	[d]	19.135	50.432
Grundkreisdurchmesser (mm)	[db]	6.465	47.343
Kopfkreisdurchmesser (mm)	[da]	21.635	52.932

5/10

KISSsoft

(mm)	[da.e/i]	21.335 /21.195	52.632 /52.462
Kopfkreisabmasse (mm)	[Ada.e/i]	-0.300 /-0.440	-0.300 /-0.470
Kantenbruch 1 / Kopfrundung im Stirnschnitt: 2, im Axialschnitt: 3, Im Normalschnitt: 4			
		4	4
Kopfrundung (mm)	[rK]	0.200	0.200
Berechnung unter Berücksichtigung der exakten Zahnform:			
Kopfformkreisdurchmesser (mm)	[dFa]	21.340	52.669
(mm)	[dFa.e/i]	21.040 /20.900	52.363 /52.209
Kopfnutzkreisdurchmesser (mm)	[dNa]	21.340	52.669
Kopfnutzkreisdurchmesser (mm)	[dNa.e/i]	21.040 /20.900	52.363 /52.209
Schraubkreisdurchmesser (mm)	[ds]	19.135	50.432
Fusskreisdurchmesser (mm)	[df]	16.010	47.307
Erzeugungsprofilverschiebungsfaktor	[xE.e/i]	-0.1754/-0.2304	-0.1754/-0.2444
Fusskreisabmasse (mm)	[Adf.e/i]	-0.300 /-0.440	-0.300 /-0.470
Effektive Fusskreisdurchmesser (mm)	[df.e/i]	15.710 /15.570	47.007 /46.837
Kopfspiel theoretisch (mm)	[c]	0.313	0.313
Kopfspiel effektiv (mm)	[c.e/i]	0.788 /0.593	0.788 /0.593
Fussnutzkreisdurchmesser (mm)	[dNf]	17.186	48.610
(mm)	[dNf.e/i]	17.550 /17.426	48.951 /48.772
Berechnung unter Berücksichtigung der exakten Zahnform:			
Fussformkreisdurchmesser (mm)	[dFf]	16.800	48.502
(mm)	[dFf.e/i]	16.513 /16.376	48.324 /48.228
Evolventenlänge (mm)	[l_dFa-l_dFf]	6.695	2.226
Addendum, mn*(haP*+x+k) (mm)	[ha]	1.250	1.250
(mm)	[ha.e/i]	1.100 /1.030	1.100 /1.015
Dedendum (mm)	[hf=mn*(hfP*-x)]	1.563	1.563
(mm)	[hf.e/i]	1.713 /1.783	1.713 /1.798
Wälzwinkel zu dFa (°)	[xsi_dFa.e/i]	177.453 /176.149	27.077 /26.637
Wälzwinkel zu dNa (°)	[xsi_dNa.e/i]	177.453 /176.149	27.077 /26.637
Wälzwinkel zu dFf (°)	[xsi_dFf.e/i]	134.665 /133.347	11.727 /11.130
Zahnhöhe (mm)	[h]	2.813	2.813
Normalzahndicke am Kopfkreis (mm)	[san]	1.049	0.953
(mm)	[san.e/i]	1.051 /0.949	1.006 /0.862
ohne Berücksichtigung Kopfkantenbruch / Kopfrundung			
Normal-Lückenweite am Fusskreis (mm)	[efn]	0.837	0.000
(mm)	[efn.e/i]	0.891 /0.891	0.000 /0.000
Steigungshöhe (mm)	[pz]	7.922	1202.318
Axiale Teilung (mm)	[px]	3.961	30.058
Teilung Normalschnitt, Grundkreis (mm)	[pbn, pen]	3.690	
Teilung Normalschnitt, Teilkreis (mm)	[pn]	3.927	
Teilung Normalschnitt, Schraubkreis (mm)	[psn]	3.927	
Länge der Eingriffsstrecke (mm)	[gan]	6.072	
Länge A-S (mm)	[AS]	3.201	
Länge S-E (mm)	[SE]	2.871	
Profilüberdeckung	[εα]	0.217	1.621 *
Sprungüberdeckung	[εβ]	1.428	0.025 *
Gesamtüberdeckung	[εγ]	1.646 *	
Gesamtüberdeckung mit Abmassen	[εγ.e/i]	1.449 /1.308*	

*Berechnet mit den Formkreisen aus der Zahnform

4 Allgemeine Einflussfaktoren

		------- Schnecke	---------- Schneckenrad ----
Nennumfangskraft im Schraubkreis (N)	[Ft]	92.35	495.71
Axialkraft (N)	[Fa]	-495.71	-92.35
Radialkraft (N)	[Fr]	183.27	-183.27

6/10

KISSsoft

Normalkraft (N)	[Fnorm]	535.8	
(Berechnung mit Normalkraft mit Berücksichtigung der Reibung)			
Breite der Druck-Ellipse (mm)	[2*a]	3.107	
Höhe der Druck-Ellipse (mm)	[2*b]	1.309	
Fläche der Druck-Ellipse (mm²)	[π*a*b]	3.780	
Mittlere Zahnreibungszahl	[muzm]	0.050	
Zahnreibungswinkel (°)	[roz]	3.046	
Verzahnungswirkungsgrad (%)	[rz]	70.737	
Umfangsgeschwindigkeit Teilkreis (m/s)	[v]	3.01	0.40
Gleitgeschwindigkeit am Schraubkreis (m/s)	[vgs]	3.03	
Max. Gleitgeschwindigkeit am Kopf (m/s)	[vgg]	3.38	3.34
Mittlere Gleitgeschwindigkeit (m/s)	[vgm]	3.20	
Lagerverlustleistung (W)	[PVLP]	0.000	
Dichtungsverlustleistung (W)	[PVD]	0.000	
Leerlaufverlustleistung (W)	[PV0]	0.000	
Verzahnungsverlustleistung (W)	[PVZ]	81.222	
Gesamtverlustleistung (W)	[PV]	81.222	
Gesamtwirkungsgrad (%)	[rGes]	70.737	
Lastwechselzahl (in Mio.)	[NL]	20.000	1.000

5 Entwurfsberechnung

		------- Schnecke	---------- Schneckenrad ----
Zähnezahlbeiwert	[Kz]	1.15	
Tragende Zahnbreite Schnecke (mm)	[bm]	10.10	
Belastungskennwert (N/mm²)	[C]	10.826	
Zulässiger Belastungskennwert (N/mm²)	[Clim]	5.555	
Sicherheit für Belastungskennwert	[Sc]	0.513	

6 Zahnflankentragfähigkeit

Zwischenresultate nach VDI 2736:
ρn1 = 24.781 mm ρn2 = 8.756 mm ρn = 6.470 mm φ = 71.509 ° θ = 56.420 °
η = 0.696 ξ = 1.652

Normalkraft (N)	[Fn]	535.8	
Breite der Druck-Ellipse (mm)	[2*ah]	3.107	
Höhe der Druck-Ellipse (mm)	[2*bh]	1.309	
Überdeckungsfaktor	[ZεS]	0.780	
Elastizitätsfaktor (√N/mm²)	[ZE]	0.062	
Elastizitätsmodul Zahnflanke (N/mm²)	[E]	10075	10075
Nominelle Flankenpressung (N/mm²)	[σHm0]	196.11	
Flankenpressung (N/mm²)	[σHm]	196.11	

7 Zahnfuss-Tragfähigkeit

		------- Schnecke	---------- Schneckenrad ----
Scherung Zahnfuss			
Berechnungsformel:	τF = Ft2 * KA / AT * Yε		
Zwischenresultate nach VDI 2736:			
Minimaler Raddurchmesser am Schneckenkopfkreis (mm)	[dx0=2*a-da1]	48.23	

7/10

KISSsoft

Zahndicke in der Mitte des Rads (mm)	[sda1]	2.52	
Maximal nutzbare Radbreite (mm)	[bmax]	10.00	
Schubquerschnitt (mm²)	[Aτ]	22.30	
Überdeckungsfaktor	[Yε]	1.00	
Nennumfangskraft im Schraubkreis (N)	[Ft]	495.71	
Scherspannung (N/mm²)	[τF]	22.23	
Zulässige Schubspannung (N/mm²) (τFadm = 0.75 * σZSch)	[τFadm]	0.00	
Sicherheit Scherung	[SFτ]	0.00	>= 1.3

8 Prüfmasse für die Zahndicke

		------- Schnecke	---------- Schneckenrad ----
Zahndickentoleranz		Eigene Eingabe	Eigene Eingabe
Zahndickenabmass im Normalschnitt (mm)	[As.e/i]	-0.160 /-0.210	-0.160 /-0.222
Messzähnezahl	[k]	0.000	5.000
Zahnweite spielfrei (mm)	[Wk]	0.000	17.323
Zahnweite mit Abmass (mm)	[Wk.e/i]	0.000 / 0.000	17.173 / 17.114
(mm)	[ΔWk.e/i]	0.000 / 0.000	-0.150 / -0.209
Messkreisdurchmesser (mm)	[dMWk.m]	0.000	50.307
Theoretischer Messkörperdurchmesser (mm)	[DM]	2.275	2.120
Effektiver Messkörperdurchmesser (mm)	[DMeff]	2.500	2.500
Radiales Einkugelmass spielfrei (mm)	[MrK]	11.770	27.326
Radiales Einkugelmass (mm)	[MrK.e/i]	11.553 / 11.484	27.142 / 27.069
Messkreisdurchmesser (mm)	[dMMr.m]	0.000	50.764
Diametrales Zweikugelmass spielfrei (mm)	[MdK]	0.000	54.651
Diametrales Zweikugelmass (mm)	[MdK.e/i]	0.000 / 0.000	54.285 / 54.137
Diametrales Rollenmass spielfrei (mm)	[MdR]	23.539	54.651
Diametrales Rollenmass nach DIN 3960 (mm)	[MdR.e/i]	23.105 / 22.969	54.285 / 54.137
Mass über 3 Rollen, axial, nach AGMA 2002 (mm)	[dk3A.e/i]	23.105 / 22.969	54.285 / 54.137
Dreirollenmass spielfrei (mm)	[Md3R]	23.539	0.000
Dreirollenmass mit Abmass (mm)	[Md3R.e/i]	23.105 / 22.969	0.000 / 0.000
Dreidrahtmass: Für ZI-Schnecken			
Zahndickensehne spielfrei (mm)	[sc]	1.963	1.963
Zahndickensehne mit Abmass (mm)	[sc.e/i]	1.804 / 1.754	1.805 / 1.743
Höhe über der Sehne ab da.m (mm)	[ha]	1.066	1.076
Zahndicke, Bogen (mm)	[sn]	1.963	1.963
(mm)	[sn.e/i]	1.804 / 1.754	1.804 / 1.741
Spielfreier Achsabstand (mm)	[aControl.e/i]	34.342 / 34.185	
Spielfreier Achsabstand, Abmasse (mm)	[ja]	-0.442 / -0.599	
Kopfspiel (mm)	[c0.i(aControl)]	0.014	0.014
Achsabstandsabmass (mm)	[Aa.e/i]	0.020 / -0.020	
Radialspiel (mm)	[jrw.e/i]	0.619 / 0.422	
Verdrehflankenspiel (Stirnschnitt) (mm)	[jtw.e/i]	0.450 / 0.307	
Verdrehspielwinkel am Antrieb bei festgehaltenem Abtrieb:			
Gesamter Verdrehspielwinkel (°)	[j.tSys]	21.8072/14.8776	

9 Verzahnungstoleranzen

		------- Schnecke	---------- Schneckenrad ----
Nach DIN ISO 1328-1:2018, ISO 1328-2:1997			

KISSsoft

Hinweis: Die Toleranzen für Zahnräder mit Schrägungswinkel > 45° sind ausserhalb des Geltungsbereichs der Norm.
Ein oder mehrere Zahnraddaten (mn, b, z oder d) liegen ausserhalb der von der Norm vorgesehenen Grenzen.
Die Toleranzen werden gemäss den Formeln der Norm gerechnet.
Sie sind aber ausserhalb des offiziellen Gültigkeitsbereichs!

Verzahnungsqualität	[Q]	A10	A10
Teilungs-Einzelabweichung (µm)	[fptT]	31.00	31.00
Grundkreis-Teilungsabweichung (µm)	[fpbT]	10.47	29.10
Teilungsspannen-Abweichung über k/8 (µm)	[Fpk/8T]	0.00	63.00
Profil-Formabweichung (µm)	[ffαT]	32.00	32.00
Profil-Winkelabweichung (µm)	[fHαT]	26.00	26.00
Profil-Gesamtabweichung (µm)	[FcT]	41.00	41.00
Flankenlinien-Formabweichung (µm)	[ffβT]	46.00	33.00
Flankenlinien-Winkelabweichung (µm)	[fHβT]	41.00	31.00
Flankenlinien-Gesamtabweichung (µm)	[FβT]	62.00	46.00
Teilungs-Gesamtabweichung (µm)	[FpT]	87.00	95.00
Teilungssprung (µm)	[fuT]	44.00	44.00
Rundlaufabweichung (µm)	[FrT]	78.00	86.00
Einflanken-Wälzabweichung (µm)	[FisT]	118.00	126.00
Einflanken-Wälzsprung (µm)	[fisT]	31.00	31.00
Zweiflanken-Wälzabweichung (µm)	[FidT]	76.00	109.00
Zweiflanken-Wälzsprung (µm)	[fidT]	25.00	26.00

FidT (Fi"), fidT (fi") nach ISO 1328:1997 berechnet mit den geometrischen Mittelwerten für mn und d

Nach ISO 1328-2:2020

Verzahnungsqualität	[Q]	R45	R44
Zweiflanken-Wälzabweichung (µm)	[FidT]	78.00	68.00
Zweiflanken-Wälzsprung (µm)	[fidT]	72.00	29.00

10 Ergänzende Daten

Gewicht - berechnet mit da (kg)	[Mass]	0.021	0.027
Trägheitsmoment, System bezogen auf Rad 1:			
Räder einzeln, (da+df)/2...di (kg*m²)	[J]	1.131e-06	8.696e-06
System, (da+df)/2...di (kg*m²)	[J]	1.153e-06	

Angabe für die Herstellung durch Drahterodieren:

Abweichung von der theoretischen Flankenlinie (µm)	[WireErr]	8.6
Zulässige Abweichung (µm)	[Fb/2]	23.0

11 Zahnformbestimmung

11.1 Daten zur Zahnformberechnung

Berechnung von Rad 1
Zahnform, Rad 1, Schritt 1: Automatisch (Fertigbearbeitung)
haP*= 1.055, hfP*= 1.195, ρfP*= 0.471
Zahnform, Rad 1, Schritt 2: Automatisch (Kantenbruch/Rundung)
r= 0.200 mm, Im Normalschnitt
Zahnform, Rad 1, Schritt 3: Modifikation für Formenbau
rdadehn= 0.300, rdfdehn= 0.300, tdadehn= 0.000, tdfdehn= 0.000, dein= 0.000 mm
Zahnform, Rad 1, Schritt 4: Modifikation zum Erodieren
fs= 0.010 mm
v= 0.000 mm/min

Berechnung von Rad 2
Zahnform, Rad 2, Schritt 1: Automatisch (Fertigbearbeitung)
haP*= 1.055, hfP*= 1.195, ρfP*= 0.471

9/10

KISSsoft

Zahnform, Rad 2, Schritt 2: Automatisch (Kantenbruch/Rundung)
r= 0.200 mm, Im Normalschnitt
Zahnform, Rad 2, Schritt 3: Modifikation für Formenbau
rdadehn= 0.300, rdfdehn= 0.300, tdadehn= 0.300, tdfdehn= 0.300, dein= 0.000 mm
Zahnform, Rad 2, Schritt 4: Modifikation zum Erodieren
fs= -0.100 mm
v= 0.000 mm/min

12 Lebensdauer, Schädigung

Konnte nicht berechnet werden.

13 Bemerkungen

- Angaben mit [.e/i] bedeuten: Maximal- [e] und Minimalwert [i] bei Berücksichtigung aller Toleranzen
Die Angabe des Verdrehflankenspiels, sowie des spielfreien Achsabstands für die Kontrolle der Zahndicke, ist nicht exakt, sie dient nur als Hinweis.
- Die Berechnung des Zahnformfaktors YF erfolgt nach ISO 6336:1996 mit Methode C, Kraftangriff am Kopf
- Die Berechnung des Fussnutzkreisdurchmessers erfolgt nach Pech.

Ende Protokoll Zeilen: 392

10/10

9.2 *MATLAB SOURCE CODE FOR PLOTTING CONTACT PATH DATA*

```
clear all
% Specify the input Excel file names as a cell array
inputFileNames  =  {'00_2.xlsx',  '00_3.xlsx',  '00_4.xlsx',  '09_2.xlsx',
'09_3.xlsx',    '09_4.xlsx',    '18_2.xlsx',    '18_3.xlsx',    '18_4.xlsx',
'27_2.xlsx',    '27_3.xlsx',    '36_1.xlsx',    '36_2.xlsx',    '36_3.xlsx',
'45_1.xlsx',    '45_2.xlsx',    '45_3.xlsx',    '54_1.xlsx',    '54_2.xlsx',
'54_3.xlsx',    '63_1.xlsx',    '63_2.xlsx',    '63_3.xlsx',    '72_1.xlsx',
'72_2.xlsx', '72_3.xlsx', '81_1.xlsx', '81_2.xlsx', '81_3.xlsx'};
%inputFileNames = {'00_3.xlsx'};


% Specify the output Excel file name
outputFileName = 'rotated_points.xlsx';

% Specify the rotation angles for each input Excel file
rotationAngles = [-9, 0, 9, -8.1, 0.9, 9.9, -7.2, 1.8, 10.8, -6.3, 2.7, -
14.4, -5.4, 3.6, -13.5, -4.5, 4.5, -12.6, -3.6, 5.4, -11.7, -2.7, 6.3, -10.8,
-1.8, 7.2, -9.9, -0.9, 8.1];
%rotationAngles = [0];


% Specify the coordinates of two points that define the rotation axis
point1 = [0, 0.031446, 0.056525];  % [x1, y1, z1]
point2 = [-0.002514, 0.031446, 0.056525];  % [x2, y2, z2]

% Initialize an empty table to store the rotated points
rotatedPointsData = [];

% Process each input Excel file
for i = 1:numel(inputFileNames)
    % Read points from the current input Excel file
    pointsData = readtable(inputFileNames{i});

    % Filter out points with pressure value of 0
    pointsData = pointsData(pointsData.Pressure ~= 0, :);

    % Extract X, Y, Z, and pressure values from the table
    x = pointsData.X;
    y = pointsData.Y;
    z = pointsData.Z;
    pressure = pointsData.Pressure;

    % Combine the coordinates into a single matrix
    points_origin = [x, y, z];

    %Translate points to new origin
    points = points_origin - point2;

    % Sort points based on pressure in descending order
```

```
    [~, sortIdx] = sort(pointsData.Pressure, 'descend');
    pointsData = pointsData(sortIdx, :);

    % Check for points with the same coordinates and keep the one with higher
pressure
    [~, uniqueIdx] = unique(pointsData(:, {'X', 'Y', 'Z'}), 'rows', 'last');
    pointsData = pointsData(uniqueIdx, :);

    % Get the rotation angle for the current input Excel file
    rotationAngle = rotationAngles(i);

    % Compute the rotation axis from the given points
    rotationAxis = point1 - point2;
    rotationAxis = rotationAxis / norm(rotationAxis);  % Normalize the vector

    % Convert the rotation angle to radians
    rotationAngleRad = deg2rad(rotationAngle);

    % Compute the rotation matrix
    rotationMatrix = axang2rotm([rotationAxis, rotationAngleRad]);

    % Rotate the points
    rotatedPoints = points * rotationMatrix;

    % Create a new table for the rotated points
    rotatedPointsDataCurrent = array2table(rotatedPoints, 'VariableNames',
{'X', 'Y', 'Z'});

    % Add the pressure values to the rotated points table
    rotatedPointsDataCurrent.Pressure = pressure;

    % Append the rotated points to the overall rotated points table
    rotatedPointsData = [rotatedPointsData; rotatedPointsDataCurrent];
end

rotatedPointsData.X = rotatedPointsData.X * 1000;
rotatedPointsData.Y = rotatedPointsData.Y * 1000;
rotatedPointsData.Z = rotatedPointsData.Z * 1000;
rotatedPointsData.Pressure = rotatedPointsData.Pressure / 1000000;

% Write the rotated points to the output Excel file
writetable(rotatedPointsData, outputFileName);

% Extract the X, Y, Z, and pressure values from the rotated points table
x = rotatedPointsData.X;
y = rotatedPointsData.Y;
z = rotatedPointsData.Z;
pressure = rotatedPointsData.Pressure;

% Define the color map based on pressure values
cmap = jet(numel(pressure));

% Create a new figure for the 3D plot
```

```
figure;

% Plot the points in 3D with color based on pressure
%scatter3(x, y, z, 30, pressure, 'filled');
F = scatteredInterpolant (x, y, pressure , 'natural');
[gx, gy] = meshgrid(-1.5:0.001:1.5, -26.2:0.001:-24.2);
vp = F(gx,gy);
s = surf (gx, gy, vp);
s.EdgeColor = 'none';
colormap(cmap);
colorbar;
caxis([0 150]);
% Set the axis labels
xlabel('X');
ylabel('Y');
zlabel('Z');

% Set the title
title('Vestakeep 4000 FC30 PEEK CF');

% Adjust the view angle
view(0,-90);

hold on;

cbar = colorbar;
ylabel(cbar, 'Pressure (MPa)');
xlabel('distance from centre (mm)');
ylabel('distance from centre (mm)');
set (cbar, 'Fontsize', 20);
set (gca, 'Fontsize', 20);

hold off;
```